



UIT

THE ARCTIC
UNIVERSITY
OF NORWAY

Faculty of Science and Technology
Department of Geosciences

Late Weichselian and Holocene glacier dynamics and sedimentary processes in and north of the Wijdefjorden-Austfjorden fjord system, north Spitsbergen

—
Carmen Braun

GEO-3900 Master's Thesis in Geology

May 2019



Abstract

Multi-proxy analyses (lithostratigraphy, physical properties, XRF core scanning, and grain size analysis) of five sediment cores and high resolution seismic (chirp) data were integrated to reconstruct the Late Weichselian and Holocene sedimentary environments and glacial history in and on the shelf north of Wijdefjorden. Three acoustic units (U1-U3) correlating with three lithostratigraphic units (L1-L3) are defined. A glacial till (U1/L1) covers most of the area, though it is sometimes lost over bedrock highs and is not visible beneath thicker sediment sequences. The overlying sediments are divided into two units representing glacier-proximal (U2/L2) and -distal (U3/L3) glaciomarine depositional settings. Both tend to drape the underlying till. Suspension settling from meltwater plumes and rivers is the primary source of such sediments. The origin of the suspended sediments fluctuates in the glacier-proximal sediments; laminations of sediments with different colours, densities, and element ratios reflect sources in either the southwest and Woodfjorden, or in the northwest and east of Wijdefjorden. The glacier-distal sediments are massive, indicating a greater distance from fluctuating sources and more stable conditions. Sediments from the southwest have a greater influence in the inner fjord, while and sediments from the east are more important in the outer fjord. In the central fjord sediments derived from both sides are important. Beyond the mouth of the fjord, sediments from Woodfjorden are present. The glaciomarine sediments also have IRD-rich (ice rafted debris) intervals in the cores, which generally correlate with internal reflections in the chirp profile and reflect periods of enhanced sea ice rafting.

The deglaciation of the shelf likely occurred before ~16 cal. ka BP, and the presence of IRD on the shelf after ~14.8 cal. ka BP likely indicates the beginning of the retreat of ice into the fjords. The transition from glacier-proximal to -distal sedimentation on the shelf, signalling a weakening glacial influence beyond the fjord, occurred around 12.2 cal. ka BP despite the Younger Dryas cooling. At ~11.5 cal. ka BP, glacier-distal sediments were deposited in the central fjord, indicating that glaciers had receded into the inner fjord. There is little IRD in the cores from ~9.3 cal. ka BP to ~3.5 cal. ka BP, signalling a period with reduced glacial activity. In the inner fjord, a transition from glacier-proximal to glacier-distal sediments occurred around 7.2 cal. ka BP, later by ~4 cal. ka than other Svalbard fjords and at a time of generally cooler conditions. This is perhaps due to locally more active glaciers or rivers near the core site prior to that time. Around ~3.5 cal. ka BP, there is increasing IRD in the cores, with a maximum from ~1.5-1.0 cal. ka BP. This is likely due to the generally cool conditions that have encouraged glacial advance since ~4 cal. ka BP.

Acknowledgments

There are so many people who have helped me get to where I am. I want to thank my supervisor, Matthias Forwick, for all his guidance and support over the last year. I am grateful for your confidence in me. Thank you for all the knowledge and experience you have shared with me, and all the discussions we have had. I also greatly appreciate all your feedback and suggestions throughout this process.

Thank you to Gesine Mollenhauer and all the other people involved with the Alfred Wegener Institute radiocarbon lab who performed the AMS radiocarbon analyses presented in this thesis. Thanks also to Seung-Il Nam, who shared additional radiocarbon dates with me. It was a pleasure to meet you both, and this thesis has benefited from the conversations we had.

To Karina Monsen, Trine Dahl, and Ingvild Hald, I appreciate all the time and effort you have spent with me in the lab and the container. You had answers, or helped me find answers, to so many questions, big or small. The many discussions I had with each of you, as well as your kind guidance and advice have all helped me immensely. Thank you also for making the lab such a lovely place to be; I enjoyed my lab time so much more because of you and your efforts.

A big thanks to my friends and fellow students. Thank you for welcoming me from the beginning and helping me get the swing of how things work here in Norway. I have had so much fun with you all, be it in class, on field trips, in the lab, or in the kantina. To Lis and Sofia, thank you for all the discussions we have had, and all the advice you have given me. Lotte, it is a shame you were only here for the first year, but thank you so much for your continued friendship, discussion, advice, and support. I would be remiss to not also thank my Canadian friends, especially Bailey, Kate, Krista, and Vanessa: because of you I feel the love from coast to coast! Thanks to Gillian too, for always being there for my phrasing questions!

To the people of Hagerups: where would I be without you! Living with you has been so lovely, hilarious, and dramatic (in the best way) and just so wonderful. I cannot imagine a better home with better people. Thank you for your friendship and support, it means a lot to me!

Thank you also to my family, thank you for your love and support no matter where in the world I am. You helped nurture my enthusiasm and curiosity and have helped me so much. Jocelyn, you are the best sister a person could ask for. Thank you for being there for me, I am so glad I can count on you, and for all the puppy photos (Dad, you too!), which never fail to put a smile on my face. Thanks for listening to my rants and confused rambling, and all the boring stuff, too.

Camille, my love, thank you. Thank you for sharing in this process, and everything else, with me. Thank you for bringing light to each day and making these amazing two years just that much better. Thank you for everything you do, and for always cutting the onions. There are no words to express how much you and your help and support mean to me; I appreciate it all, and you, so much.

Thank you all so very much,

Carmen Braun

Table of Contents

Abstract.....	iii
Acknowledgments.....	v
1 Introduction.....	1
1.1 Objectives	1
1.2 Background.....	1
1.2.1 Svalbard Late Weichselian and Holocene Glacial History	1
1.2.2 Previous investigations in the Study Area and Northern Spitsbergen.....	6
2 Study Area	9
2.1 Bedrock geology.....	10
2.2 Geochemistry.....	12
2.3 Glaciology	13
2.4 Bathymetry	16
2.5 Oceanography and Hydrography.....	17
2.5.1 Currents	17
2.5.2 Fjord dynamics	18
2.6 Sea Ice.....	20
2.7 Climate.....	20
3 Materials and methods	23
3.1 Acoustic Data – Chirp sonar.....	23
3.2 Sediment cores.....	23
3.3 Laboratory work	24
3.3.1 Physical properties.....	24
3.3.2 Opening cores	25
3.3.3 X-ray photography.....	26
3.3.4 Sedimentological descriptions.....	26
3.3.5 Element geochemistry	26

	Line scan imaging.....	28
	3.3.6 Grain-size analysis.....	28
	3.3.7 Radiocarbon dating.....	29
4	Results.....	33
4.1	Acoustic data	33
4.1.1	Overview	33
4.1.2	Distribution.....	36
4.2	Lithostratigraphic results	39
4.2.1	Continental shelf: core HH17-1085-GC-MF.....	43
4.2.2	Fjord mouth: core HH17-1091-GC-MF	48
4.2.3	Outer Fjord: core HH17-1095-GC-MF	51
4.2.4	Middle Fjord: core HH17-1100-GC-MF.....	54
4.2.5	Inner Fjord: core HH17-1103-GC-MF.....	57
4.2.6	Chronology	60
4.2.7	Sedimentation rates.....	61
5	Discussion.....	63
5.1	Acoustic data	63
5.1.1	Units.....	63
5.1.2	Distribution.....	64
5.2	Correlation of acoustic data and sediment cores	66
5.2.1	Core 1085	67
5.2.2	Core 1091	68
5.2.3	Core 1095	69
5.2.4	Core 1100	69
5.2.5	Core 1103	70
5.3	Sedimentary processes and provenance	72
5.3.1	Suspension settling	72

5.3.2	Ice rafting.....	74
5.3.3	Sediment provenance.....	75
5.4	Sedimentation rates.....	84
5.4.1	Core 1085	84
5.4.2	Core 1091	86
5.4.3	Core 1095	86
5.4.4	Core 1100	87
5.4.5	Core 1103	87
5.4.6	Correlations between Wijdefjorden cores	88
5.5	Paleoclimate and environment of Wijdefjorden since the Late Weichselian	89
5.5.1	Late Weichselian (>11.65 cal. ka BP)	90
5.5.2	Early Holocene (11.65-7.0 cal. ka BP).....	93
5.5.3	Mid to late Holocene (7.0 cal. ka BP - present)	96
6	Summary and Conclusions	99
7	References.....	101

1 Introduction

1.1 Objectives

The main objective of this master thesis is to reconstruct the Late Weichselian deglaciation dynamics and the Holocene paleoenvironment development in and on the shelf north of the Wijdefjorden fjord system. This will help improve current understanding of the glacial dynamics and post-glacial environment in northern Spitsbergen. The reconstruction is based primarily on lithological data from five sediment cores, as well as high-resolution seismic data.

1.2 Background

Fjords, deep, high-latitude estuaries carved by glaciers (Syvitski et al., 1987), are ideal locations for paleoenvironmental studies as they host unique depositional environments that transition from a terrestrially dominated inner fjord to the marine dominated outer fjord. Their temporal resolution is often higher than many other marine archives due to the proximity of sediment sources and the associated higher sedimentation rates (Howe et al., 2010b; Syvitski et al., 1987). As such, they contain valuable records of climatic and environmental changes since the last deglaciation. Additionally, the fjords of Svalbard are subpolar (Domack and McClemen, 1996; Howe et al., 2010b) and are often free of sea ice during the summer, which increases accessibility.

1.2.1 Svalbard Late Weichselian and Holocene Glacial History

Svalbard has experienced several major glacial advances, the most recent being in the Late Weichselian. Ice sheet growth and decay are closely linked to Atlantic Water (AW) and Polar Water and changes in their relative strengths (e.g. Bauch et al., 2001; Knies et al., 1999; Nielsen and Rasmussen, 2018; Vorren and Plassen, 2002). In the Late Weichselian, AW was still advected to the Nordic seas and ensured seasonally open water, which provided the moisture required for ice sheet growth at the high latitudes (Andersen et al., 1996; Jessen et al., 2010).

A general understanding of the timing and dynamics of this glaciation and the subsequent deglaciation have been developed for the greater Svalbard area. However, variability between different regions (e.g., western and northern Spitsbergen, and the many islands of the archipelago) exists, and it is generally poorly constrained (Batchelor et al., 2011; Dowdeswell et al., 2010; Forman and Ingólfsson, 2000; Fransner et al., 2017; Gjermundsen et al., 2013; Landvik et al., 2003, 1998; Lloyd et al., 1996).

1.2.1.1 Ice sheet growth and dynamics

The Svalbard Barents Sea Ice Sheet (SBIS) began to grow ~32 cal. ka BP (thousand calibrated radiocarbon years before present: 1950 AD) (Andersen et al., 1996; Jessen et al., 2010; Landvik et al., 1998) and reached its maximum extent on the western Spitsbergen shelf ~23.8 cal. ka BP (Jessen et al., 2010). Others suggest the western maximum occurred later, for example around 19 cal. ka BP (Andersen et al., 1996; Elverhøi et al., 1995) or between 20-15 ka BP (thousand calendar years before present) (Svendsen et al., 2004). Comparatively, in the north, the ice sheet reached its maximum earlier, around ~25 cal. ka BP (Kleiber et al., 2000) or around 23-22 ka (Chauhan et al., 2016b). Regardless of the timing, there is now consensus that the SBIS extended all the way to the shelf edge in both the west and north of Svalbard at its maximum (Andersen et al., 1996; Dowdeswell and Elverhøi, 2002; Hormes et al., 2013; Jessen et al., 2010; Kleiber et al., 2000; Landvik et al., 1998; Mangerud et al., 1998; Svendsen et al., 2004).

At the glacial maximum, the SBIS was initially thought to include two styles of glaciation: a large, marine based ice sheet, and local ice domes on land, with some fjords being free of glaciers (Forman et al., 1987; Mangerud et al., 1987). Some areas of north-western Spitsbergen were, while others continue to be, interpreted as being ice free as well (Hormes et al., 2013; Landvik et al., 2003; Salvigsen, 1979), though they may have instead been covered in non-erosive, cold-based ice (Gjermundsen et al., 2015, 2013; Hormes et al., 2013). The SBIS is now generally accepted to have had a major ice dome, with some smaller, local domes (Dowdeswell et al., 2010; Gjermundsen et al., 2013; Hogan et al., 2010; Hormes et al., 2013; Landvik et al., 1998; Ottesen et al., 2005), however the interpreted location of the major ice dome varies. Reconstructions of the ice dome locations (Figure 1-1) are now largely based on the location of ice streams, areas of fast-flowing ice that would have rapidly drained large volumes of ice from the SBIS (Dowdeswell et al., 2010; Hogan et al., 2010), though earlier models primarily used isostatic models and emergence rates from paleo-shorelines (Lambeck, 1995; Landvik et al., 1998). The largest ice streams flowed west from the Barents Sea through Storfjordrenna and Bjørnøyrenna, and north through the Kvitøya and Franz Victoria troughs to the east of Svalbard. On Svalbard, ice streams flowed through many of the western and northern fjords, including Wijdefjorden (for a more detailed discussion of ice streams in Wijdefjorden, see section 1.2.2), and through the Hinlopen Strait as well (e.g., Alexanderson et al., 2011; Dowdeswell et al., 2010; Flink and Noormets, 2018; Gjermundsen et al., 2015; Kleiber et al., 2000; Landvik et al., 2005; Ottesen et al., 2007, 2005; Ottesen and Dowdeswell,

2009; Streuff et al., 2017). Between the fast-flowing ice streams, or in the inter-ice stream areas, slower flowing and sometimes cold-based ice was present (Batchelor et al., 2011; Gjermundsen et al., 2013; Henriksen et al., 2014; Landvik et al., 2014; Ottesen and Dowdeswell, 2009).

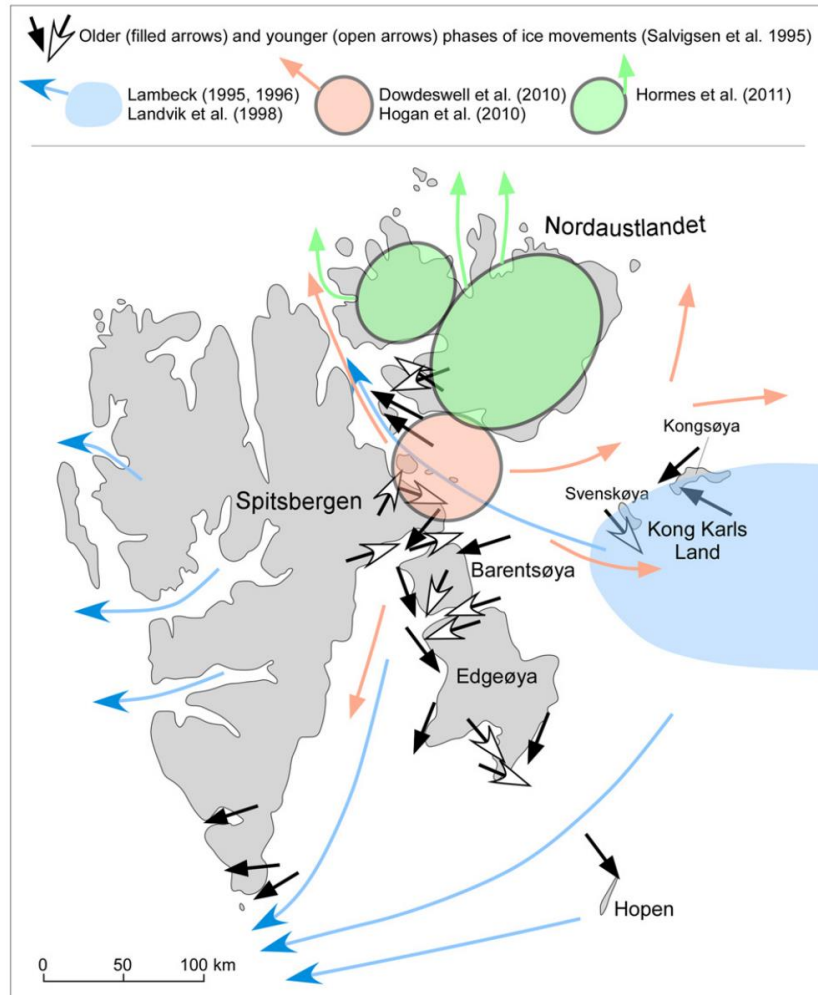


Figure 1-1. Different locations of proposed ice domes. Figure from Ingólfsson and Landvik (2013).

1.2.1.2 Late Weichselian and early deglaciation

The deglaciation of the SBIS on Svalbard likely began with a retreat from the outer shelf around 20-21 cal. ka BP (Gjermundsen et al., 2013). This initial retreat was slow, with a possible standstill or readvance around 16 cal. ka BP, followed by more rapid retreat between 15.7 and 11.7 cal. ka BP (Jessen et al., 2010, and references therein). Mangerud et al. (1992) found that the earliest deglaciation on the west coast occurred by ~12.5 ka and that in the north, this occurred slightly later: the earliest deglaciation there occurred by ~10.8 ka. The same study established that both the west and north, as well as the east, had deglaciated by around 10 ka.

Other studies show that deglaciation began around 14.5 ka on the western shelf (Andersen et al., 1996) and that it was deglaciated by 11.7 ka, with the deglaciation of the fjords occurring around 10.1 cal. ka BP (Andersen et al., 1996; Elverhøi et al., 1995; Jessen et al., 2010; Mangerud et al., 1998). The timing of deglaciation is relatively well constrained on the western Spitsbergen margin compared to the northern margin.

In the northwest of Spitsbergen and to the east of Wijdefjorden, there is evidence that the thinning of the ice dome commenced between 25-20 ka (Gjermundsen et al., 2013; Hormes et al., 2013) and that, on the northern margin, partial breakup of the SBIS began offshore around 20 ¹⁴C (radiocarbon) ka BP (~21.5 cal. ka BP) with several subsequent readvances and collapses until around 16.2 ¹⁴C ka BP (~17 cal. ka BP) (Knies et al., 2000). Partial breakup occurred during Heinrich stadial 1 (18-15 cal. ka BP) on the shelf north of Woodfjorden (Bartels et al., 2017), and at a similar time (18.5 cal. ka BP) north of Nordaustlandet (Chauhan et al., 2016b). Rapid disintegration of the ice sheet on the northern continental margin may have begun around 15.4 ¹⁴C ka BP (~16.1 cal. ka BP) (Knies et al., 2000). Similarly, Hormes et al. (2013) found that the retreat of grounded ice on the shelf in this area began after 15.9 ka, with inner shelf areas deglaciating between 15 and 14 ka. They also found that the outer and central parts of Wijdefjorden were deglaciated around ~14.6 to 13.8 ± 1 ka, and that Reinsdyrflya was deglaciated slightly prior to this. The deglaciation of the Hinlopen Strait seems to have occurred slightly earlier, with fully glaciomarine conditions established by around 16.9-16.5 cal. ka BP (Ślubowska et al., 2005); this deglaciation was likely rapid based on the absence of grounding zone wedges (Batchelor et al., 2011). The Kvitøya Trough was likely fully deglaciated by 14.2 cal. ka BP (Rasmussen et al., 2007). Gjermundsen et al. (2013) found later deglaciation ages (~13.4 ka) for outer Woodfjorden, but Bartels et al. (2017) found that AW advection was already helping destabilise the local glaciers in Woodfjorden during the Bølling-Allerød (~14.6-12.9 ka), suggesting an earlier deglaciation of the outer fjord. Based on shoreline studies of Andrée Land, which separates Woodfjorden from Wijdefjorden, Brückner and Schellmann (2003) suggest the area was also seasonally free of sea ice during the Bølling and Allerød interstadials.

The impact of the Younger Dryas cooling is still poorly defined, with little evidence of a widespread glacial readvance or standstill on land (Mangerud and Landvik, 2007; Svendsen and Mangerud, 1992, 1997). There are indications of potential growth for some glaciers, while other glaciers appear to have remained stable, or even to have continued their retreat during

this period (Bartels et al., 2017; Butschek et al., 2018; Forwick and Vorren, 2009, 2011; Nielsen and Rasmussen, 2018). In northeast Svalbard, one glacier is thought to have re-advanced between ~11.9 and 10.6 cal. ka BP (Farnsworth et al., 2018). There is also evidence suggesting there was increased sea ice cover during the Younger Dryas period, which could have suppressed glacier calving (Bartels et al., 2017; Butschek et al., 2018; Forwick and Vorren, 2009; Kristensen et al., 2013) and beach ridge formation (Brückner and Schellmann, 2003). Enhanced meltwater production at that time isolated the warm AW from the air, causing the sea surface temperature (SST) to fall, and therefore enabling the sea ice expansion (Bartels et al., 2017; Butschek et al., 2018; Chauhan et al., 2016a).

1.2.1.3 Holocene

At the Younger Dryas/Holocene boundary, there is evidence of an influx of AW to northern Svalbard and the temperature was warmer (Bartels et al., 2017; Butschek et al., 2018; Chauhan et al., 2016b; Salvigsen and Österholm, 1982). The final deglaciation of most fjords occurred around in the early Holocene (e.g., Svendsen et al., 1996); for example, Van Mijenfjord, Billefjorden and Isfjorden, and Van Keulenfjord in western Spitsbergen deglaciated around 11.2 cal. ka BP (Baeten et al., 2010; Forwick and Vorren, 2009; Hald et al., 2004) or 10.7 cal. ka BP (Kempf et al., 2013). In northern Spitsbergen, this likely occurred slightly later. Bartels et al. (2017) suggest the glaciers of Woodfjorden reached their innermost positions around 10.1 cal. ka BP, supporting Salvigsen and Høgvard's date for the deglaciation of Bockfjorden, a branch of Woodfjorden (2005); additionally, the evidence from Hansen (2014) suggests a similar timing. To the east on Nordaustlandet, two fjords were deglaciated before ~10.6 cal. ka BP (Fransner et al., 2017). In general, this final deglaciation likely occurred stepwise (Baeten et al., 2010; Bjarnadóttir et al., 2013; Butschek et al., 2018; Forwick et al., 2011; Hogan et al., 2010; Kempf et al., 2013; Kleiber et al., 2000; Ottesen et al., 2007) and led to reduced glacier cover during the early and mid-Holocene (e.g., Dowdeswell and Elverhøi, 2002; Salvigsen and Høgvard, 2005; Ślubowska et al., 2005; Svendsen et al., 1996).

The influence of AW was greater between 9.0 and 6.0 ka (Rasmussen et al., 2014), with intermittent cooling at around 8.8 and 8 cal. ka BP (Bauch et al., 2001; Forwick and Vorren, 2009; Hald et al., 2004). Some glaciers in western Spitsbergen appear to have begun to grow around 9 ka, after which glaciers grew asynchronously (Baeten et al., 2010; Forwick et al., 2010; Forwick and Vorren, 2009). In other western Spitsbergen fjords, this occurred later,

around 7.5-7.0 ka (Forwick and Vorren, 2007; Hald et al., 2004), or in the late Holocene (Svendsen and Mangerud, 1997).

In the late Holocene, cooling of the waters recommenced as the influence of AW declined around 6 ka (Hansen, 2014; Kristensen et al., 2013; Mangerud and Svendsen, 2018; Rasmussen et al., 2014; Telesiński et al., 2018). The last 4 ka have been relatively cool and stable (Bauch et al., 2001; Butschek et al., 2018; Forwick and Vorren, 2009; Hald et al., 2004; Rasmussen et al., 2013; Svendsen and Mangerud, 1997) and from 3.7 ka, sea ice cover was extensive and potentially near perennial (Chauhan et al., 2016b; Forwick et al., 2010). Additionally, some western Spitsbergen glaciers formed around 4 ka (Svendsen and Mangerud, 1997).

For the last two thousand years, there has been a general trend of weakening glacial influence in the waters surrounding Svalbard (Jernas et al., 2013; Telesiński et al., 2018). Starting at that time, AW flow was strong and there was little IRD deposition. Later, AW inflow was reduced for a period between ~1650 and 1250 BP, allowing for sea ice to develop and increased ice-rafting. Following this, it again gained strength, leading to reduced sea ice cover (Chauhan et al., 2016b). It weakened again from 450 to 50 BP, a period with extensive sea ice cover and increased IRD, interpreted to correspond with the Little Ice Age. Since 1950 (0 BP), there has been, for example, less sea ice cover of the Hinlopen Strait and stronger advection of AW in western Spitsbergen (Jernas et al., 2013).

1.2.2 Previous investigations in the Study Area and Northern Spitsbergen

Studies in the north of Spitsbergen are few, especially compared to the more easily accessible western Spitsbergen. Hence, information characterising the deglaciation of the SBIS is sparse, and we have only an incomplete picture. As mentioned in sections 1.2.1.2 and 1.2.1.3, partial breakup of the SBIS on the northern shelf of Spitsbergen occurred around 18-15 cal. ka BP (Bartels et al., 2017). Using cosmogenic nuclide ages, Hormes et al. (2013) determined that the inner part of Wijdefjorden at ~140 m a.s.l (above sea level) became ice-free between 14.6 and 13.8 ± 1.0 ka. This fits with data from beach ridges studied on the headland west of Wijdefjorden, where Brückner and Schellmann (2003) showed that the glaciers must have retreated past the Vogtvatnet area before, and that there was limited sea ice, around 12 ka, allowing the oldest ridges to form. They identified a gap in beach ridge formation between 11.1 and 10.6 ka, likely due to sea ice blocking the fjords during the Younger Dryas. Neighbouring Woodfjorden has been more intensively studied than Wijdefjorden. Studies there have found that the outer part of Woodfjorden deglaciated around 13.4 (Gjermundsen et

al., 2013) and the glaciers in Woodfjorden reached their innermost positions around 10.1 cal. ka BP (Bartels et al., 2017; Hansen, 2014; Salvigsen and Høgvard, 2005).

Studies focusing on the marine geology of the Wijdefjorden region are especially rare. Kowalewski et al. (1990) acquired a longitudinal profile of the fjord using continuous seismic profiling (CSP) (Figure 1-2). They defined four seismo-acoustic units: bedrock, till or compacted glaciomarine deposits, glaciomarine ice-front deposits, and glaciomarine mud. They showed that the glaciomarine muds drape the fjord floor along the entire profile. The authors interpreted the locations of several local still-stands, with the northernmost being beyond the mouth of the fjord near Moffen. They also identified one near the fjord mouth across from Bangenhuk, and two within the fjord: one across from Sturfjellet and one poorly defined further inland.

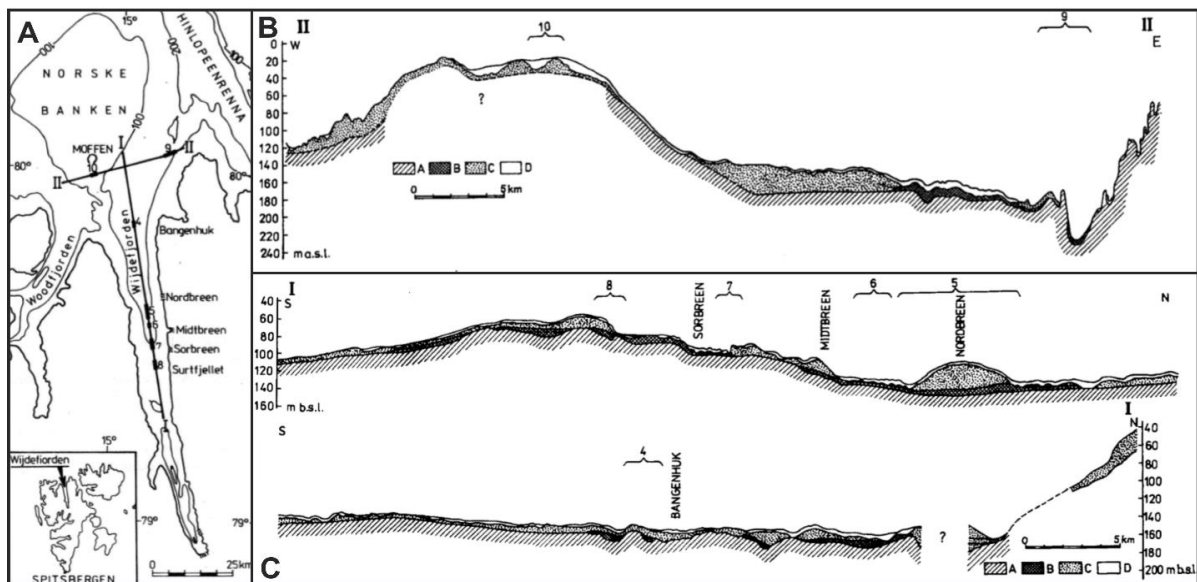


Figure 1-2. Figures from Kowalewski et al. (1990), showing A) Wijdefjorden, with place names indicated, and the locations of the two profiles: II, trending E-W (B), and I, trending N-S (C). In the profiles, A = bedrock, B = till or compacted glaciomarine deposits, C = glaciomarine ice-front deposits, and D = glaciomarine mud.

Multibeam bathymetry from the outer fjord and fjord-mouth shows megascale glacial lineations (MSGL) up to 5 km long (Figure 1-3) (Ottesen et al., 2005). They are up to 10 m high max (average 2-4 m), with an average width of 260 m and an average distance of 480 m between ridge crests. They are oriented parallel to the fjord and meet with MSGL from the Hinlopen trough, showing that ice flowing from Wijdefjorden was confluent with the ice stream in the Hinlopen trough. They end at the shelf break 70 km to the north. The MSGL

from Woodfjorden split around Moffen island and the Norwegian bank, and meet with those from Wijdefjorden (Figure 1-3) (Ottesen et al., 2007, 2005). They are typical of fast ice flow through paleo-ice streams (Flink and Noormets, 2018; Ingólfsson and Landvik, 2013; Landvik et al., 2005; Ottesen et al., 2005). Recessional moraines or grounding-zone wedges are absent in this area, which indicates rapid thinning and retreat of the ice sheet from outer Wijdefjorden (Ottesen et al., 2007).

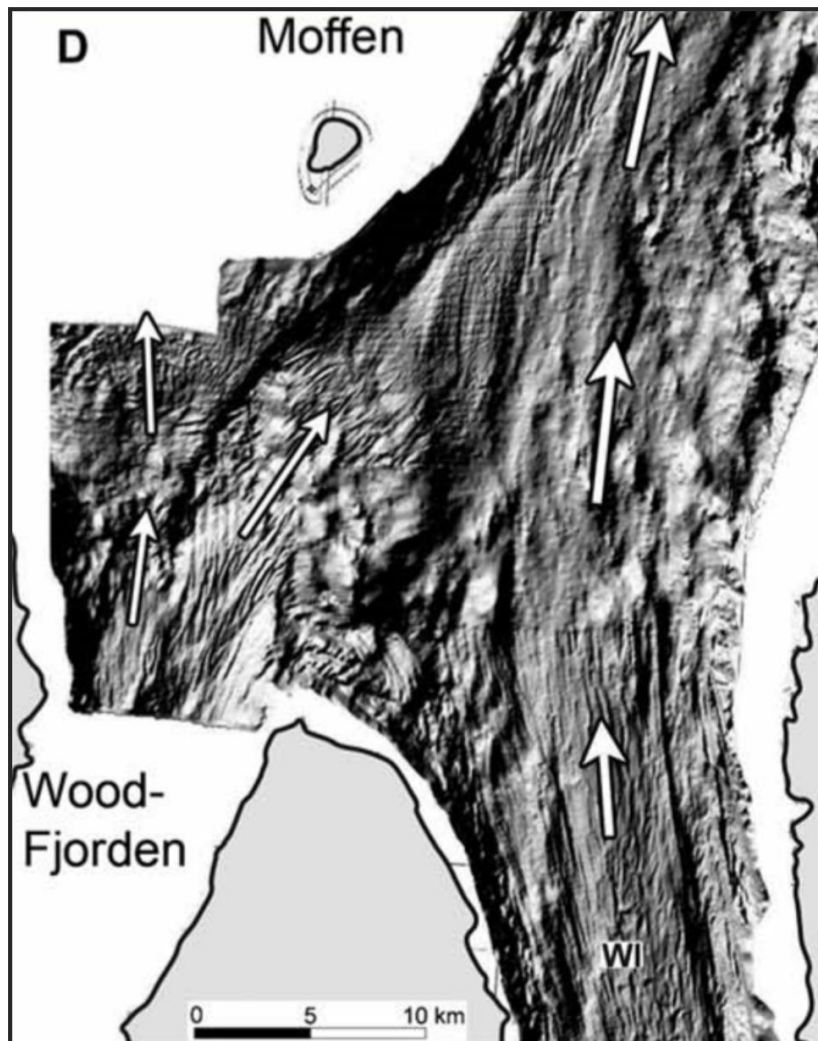


Figure 1-3. Shaded-relief image of the seafloor showing megascale glacial lineations (MSGSL) in outer Wood-fjorden and Wijdefjorden (WI), with their orientation highlighted by arrows. Figure from Ottesen et al., 2005.

2 Study Area

Svalbard is an archipelago that includes all land masses between 74° and 81°N, and 10° and 35°E (Figure 2-1). The study area, the Wijdefjorden-Austfjorden fjord system, is a fjord system in the north of Spitsbergen, the largest of the Svalbard islands (Figure 2-2). It is the longest of the Svalbard fjords at 108 km (Statistisk Sentralbyrå, 2005). Running N-S, the fjord system separates Andrée Land in the west from Ny-Friesland and Margaretas Land in the east. Wijdefjorden is renamed Austfjorden south of where Vestfjorden branches off to the west (Figure 2-2). At the head of Austfjorden, it is ~5 km wide and it widens to ~20 km at the mouth of Wijdefjorden. From there, it continues as a NE-SW cross-shelf trough that eventually meets the Hinlopen trough as a hanging fjord (Ottesen et al., 2007). The maximum water depth is 230 m in the inner fjord (Figure 2-6). For simplicity, I will refer to the Wijdefjorden-Austfjorden system as Wijdefjorden in this thesis.



Figure 2-1. Overview map of Svalbard with an inset panarctic map (bottom right) and box indicating the extent of Figure 2-2. On the inset map, the box indicates the extent of the Svalbard overview map. Created with Plot-Svalbard (Vihtakari, 2019).

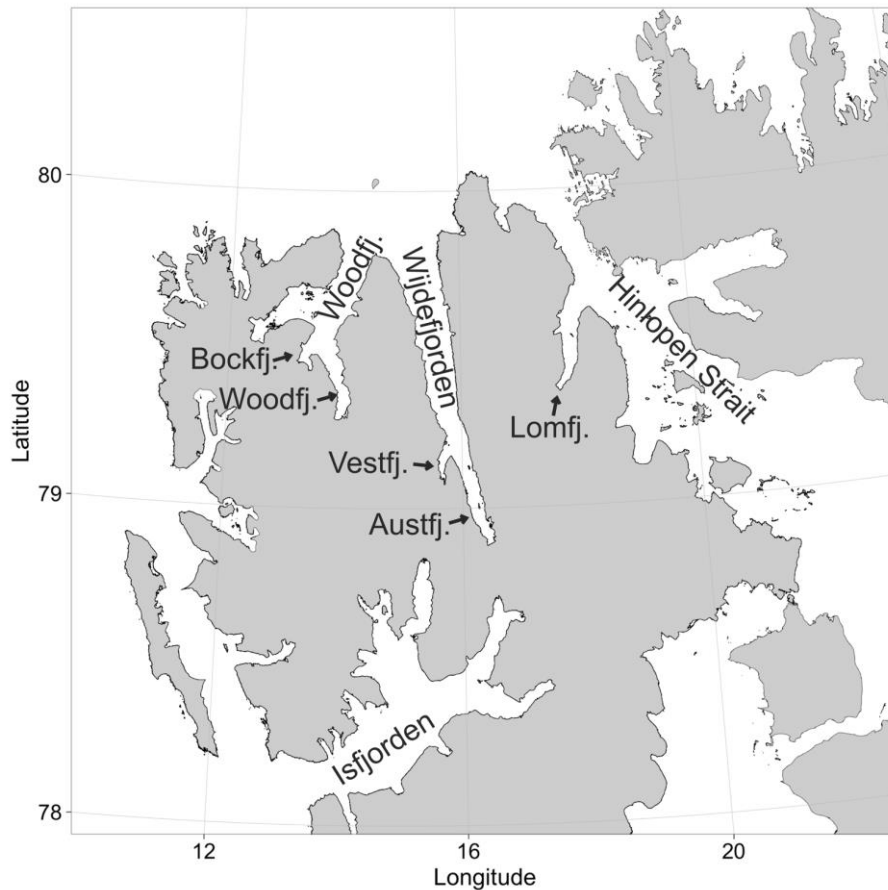


Figure 2-2. Overview map of the study area (Wijdefjorden) with other major fjords and the Hinlopen Strait indicated. Note: fj. = fjorden. Created with PlotSvalbard (Vihtakari, 2019).

2.1 Bedrock geology

Svalbard has many major fault systems, including the N-S trending Billefjorden Fault Zone that traverses the entire length of Wijdefjorden (Figure 2-3, Figure 2-4). This results in distinct bedrock geology on either side of the fjord. Andrée Land, to the west of Wijdefjorden, is dominated by the Wijde Bay, Grey Hoek, and Wood Bay formations from the Andrée Land Group (Dallmann, 2015; Ramberg et al., 2013). The Wijde Bay Formation outcrops nearer the mouth of the fjord and consists of Mid-Devonian sandstones. The slightly older sandstones and shales of the Grey Hoek Formation outcrop at the mouth and middle. Wood Bay Formation forms the base of the group and is from the Early Devonian; it is composed of red sandstones ranging in grain size from siltstones to conglomerates, with subordinate limestone (Dallmann, 2015; Hjelle, 1993; Norwegian Polar Institute, 2016; Pernègre and Blicek, 2016).

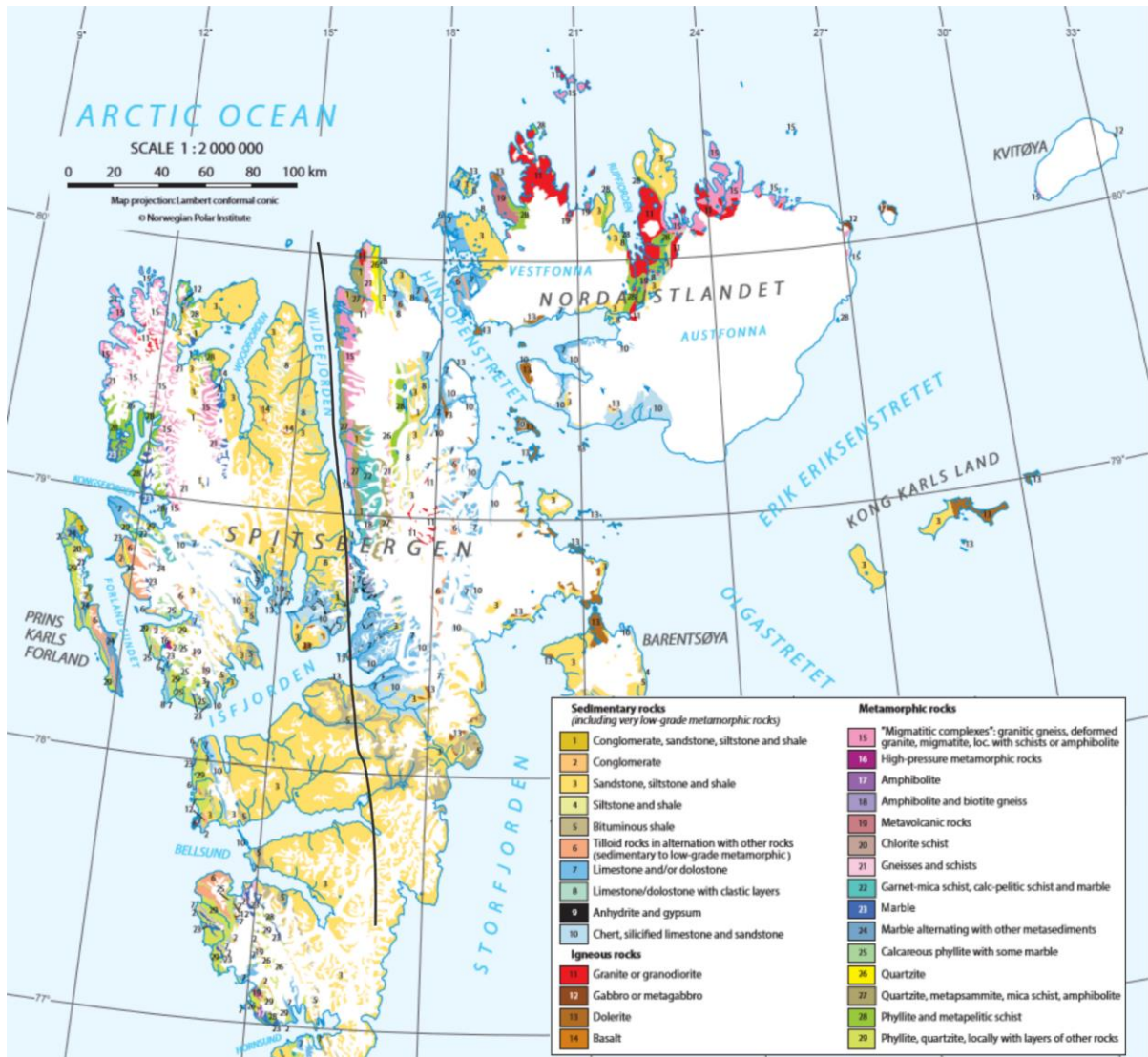


Figure 2-3. Bedrock geology map of Svalbard, with the Billefjorden fault zone indicated through Wijdefjorden and continuing to the south (black line). Modified from Dallmann (2015).

To the east of Wijdefjorden lie mostly paleoproterozoic rocks from the Atomfjella antiform complex, which includes the Vassfaret unit (micaschist, metapsammite, amphibolite), the Banguhuk unit (granitic gneiss, migmatite, amphibolite), the Polhem and Rittervatnet units (quartzite, micaschist, amphibolite, marble), the Smutsbreen unit (garnet-micaschist, calc-peliticschist, amphibolite, marble), and the Eskolabreen unit (biotite gneiss, amphibolite) (Corfu et al., 2014; Dallmann, 2015; Hjelle, 1993; Norwegian Polar Institute, 2016). The area with exposed Atomfjella complex bedrock also represents an area with a high magnetic anomaly (Dallmann, 2015). The bedrock at and south of the fjord-head consists primarily of members of the Carboniferous Campbellryggen subgroup, and includes carbonates, evaporites,

and clastic sedimentary rocks (Dallmann, 2015; Hjelle, 1993; Norwegian Polar Institute, 2016).

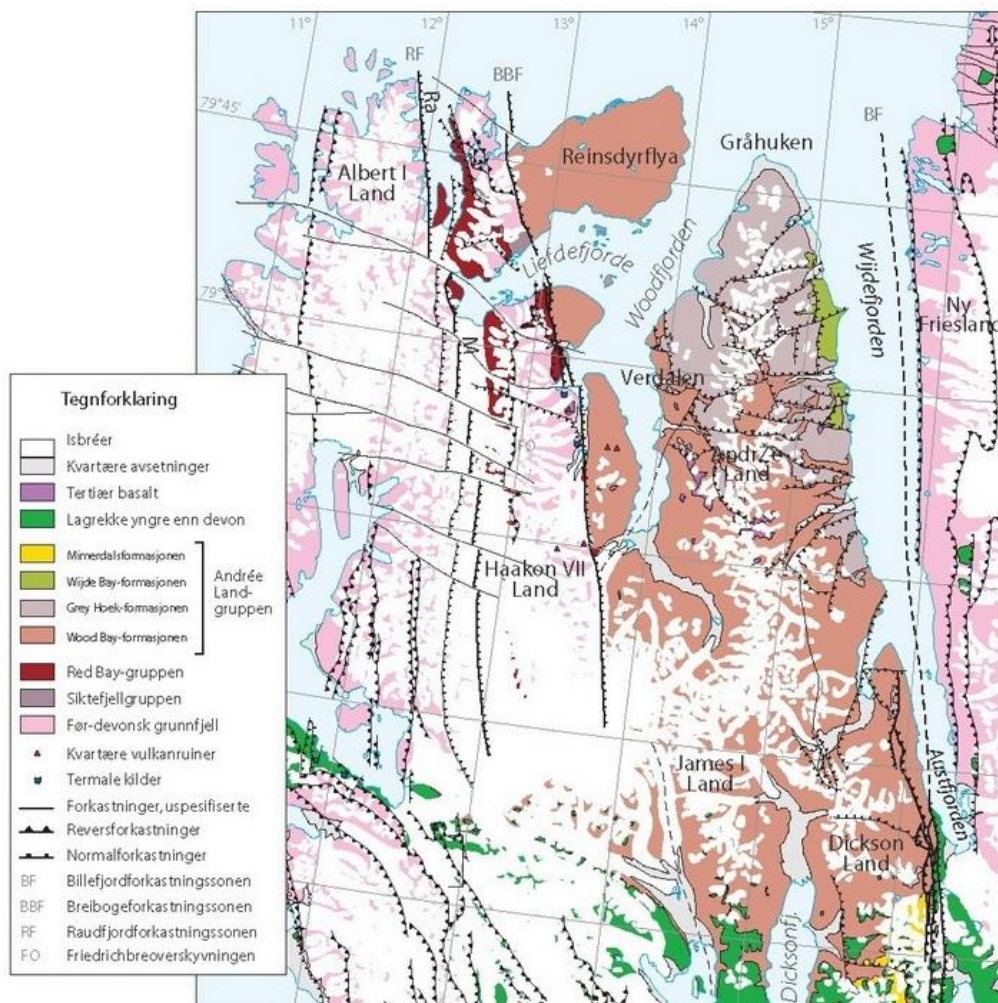


Figure 2-4. A more detailed geologic map of the Devonian succession to the west of Wijdefjorden. Modified from Ramberg et al. (2013).

2.2 Geochemistry

The geochemistry of the area, based on the results of overbank sediment sampling, shows that certain elements are more common in some areas than others (Ottesen et al., 2010). Aluminium (Al) is present in higher concentrations (up to ~4.5%) on both sides of Wijdefjorden than in the area just south of the fjord. Inversely, calcium (Ca) is present in very high concentrations south of Wijdefjorden (up to ~21%) and in the southwest of the fjord (~2-8%), while accounting for only ~1-3% in the northwest and east of the fjord. Iron (Fe) is present along much of the east and the northwest of the fjord in concentrations up to ~6%, and between ~1 to 3% in the south and southwest. The concentration of potassium (K) is higher (~0.3-0.9%) in the east and southwest of the fjord, as well as at the very tip of the western headland, than in

the south and northwest of the fjord (~0.08-0.3%). Titanium (Ti) is present in relatively high concentrations to the east of Wijdefjorden (up to 0.3%), whereas in the west it accounts for only up to ~0.02 %. Zirconium (Zr) does the opposite, with higher concentrations (~4.5-14.5 ppm) to the west, and particularly the northwest, of Wijdefjorden, and lower (<~0.4 ppm) concentrations to the south and east of the fjord. Rubidium (Rb) is relatively equally concentrated on both sides of the fjord (~10-330 ppm), though it is present only in very low concentrations south of Wijdefjorden (<70 ppm). Strontium (Sr) has a distribution similar to Ca, with concentrations up to ~600 ppm south of the fjord and only ~7-80 ppm on each side of the fjord, with the slightly higher values more common in the west. Please note that all values given are only rough estimates based on the figures presented in the Geochemical Atlas of Spitsbergen (Ottesen et al., 2010).

2.3 Glaciology

Recent data, largely from 2007-2008, show glaciers cover 57% of the Svalbard archipelago (Nuth et al., 2013). Svalbard is divided into several catchment areas; the Wood-/Wijdefjorden catchment (Figure 2-5) system covers 7349 km² (Nuth et al., 2013) and is further subdivided into secondary drainage basins (SDB). There are four SDBs in the Wijdefjorden catchment area: Andrée Land NE, Andrée Land SE, Austfjorden, and Ny Friesland W (Figure 2-5). Glacier cover varies between the different SDBs and is lower in the west and higher in the south and east of the fjord (see Table 2-1).

In the Wijdefjorden catchment system, data from 1960-1980 shows that 41.85% of its 4375 km² area (1831 km²) was glaciated (Hagen et al., 1993). More recent data is unavailable for just this system. However, when considering the greater Wood-/Wijdefjorden catchment area, the glaciated area has decreased from 42.8% in the 1960-1980s (Hagen et al., 1993) to 40% in the late 2000s (Nuth et al., 2013) (see Table 2-1). The named glaciers with an area larger than 1 km² in the Wijdefjorden SDBs have decreased between 1.6 and 16.7% between 1960-1980 and 2007-2008 (Table 2-2) (calculated from data in Hagen et al., 1993, and GLIMS and NSIDC, 2005).

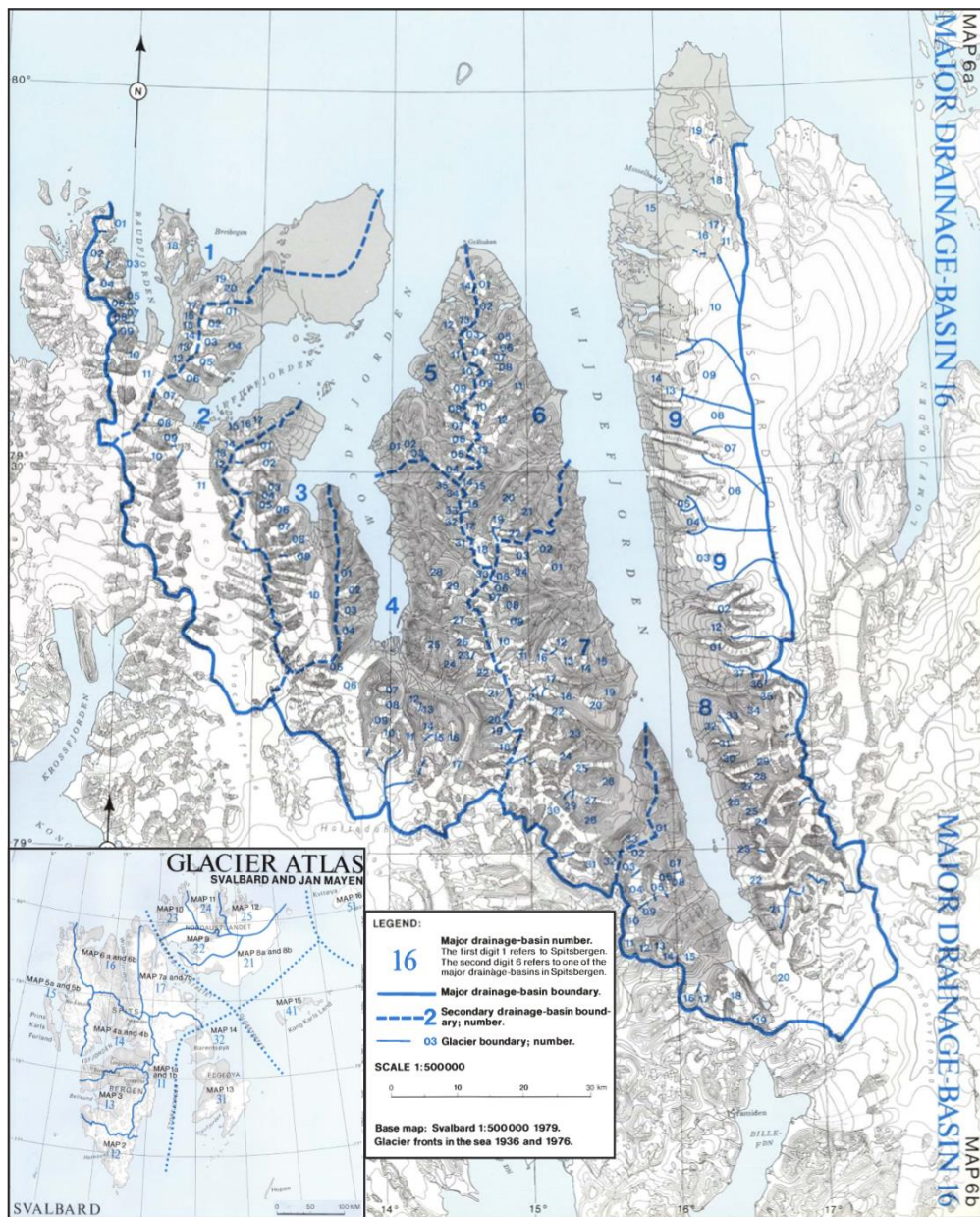


Figure 2-5. Map of the catchment area with secondary drainage basins numbered: 6 = Andrée Land NE, 7 = Andrée Land SE, 8 = Austfjorden, and 9 = Ny Friesland W. Inset map shows overview of other catchment areas. Modified from Hagen et al. (1993).

Table 2-1. Glacier information for Wood-/Wijdefjorden Catchment Area and Wijdefjorden Secondary Drainage Basins

Drainage basin no.	Basin name	Basin Area (km ²)	Number of Glaciers	Total Glaciated Area (km ²)	% Glacier Cover
166	Andrée Land NE	492	54	116	23.5
167	Andrée Land SE	925	61	291	31.5
168	Austfjorden	1360	56	728	53.5
169	Ny Friesland W	1598	31	696	43.5
Total		4375	202	1831	41.85
Wood-/Wijdefjorden		7597	381	3250	42.8
2013 Wood-/Wijdefjorden		7349	338	2959	40.0

Note: All data from Hagen et al. (1993) except 2013 Wood-/Wijdefjorden total, from Nuth et al. (2013). Italics indicate calculated value.

Table 2-2. Area of named glaciers with an area greater than 1 km²

	Glacier Area (km ²)			
	<u>GAS</u>	<u>GLIMS</u>	<u>Change</u>	<u>% Change</u>
Andrée Land NE	46.65	38.84	7.81	16.7
Andrée Land SE	217.70	181.70	36.00	16.5
Austfjorden	685.50	604.51	80.99	11.8
Ny Friesland W	638.40	628.34	10.06	1.6

Note: GAS is the Glacier Atlas of Svalbard, with data collected primarily in 1960/1961, with few data from 1969 and the 1980s (Hagen et al., 1993), while GLIMS (Global Land Ice Measurements from Space) uses data from 2007 and 2008 (GLIMS and NSIDC, 2005).

Of the total glaciated area in Svalbard, 68% drains through tidewater glaciers (Nuth et al., 2013). However, only four glaciers (34.3% of glaciated area) in the Wijdefjorden catchment area are currently tidewater glaciers: Nordbreen and Midtbreen (Ny Friesland W), and Stubendorffbreen and Mittag-Lefflerbreen (Austfjorden) (for locations see Figure 2-6). The remainder, and all the glaciers in the Andrée Land SDBs, terminate on land. About nine of the Wijdefjorden glaciers, including Mittag-Lefflerbreen, have been documented to exhibit surge behaviour; however, it is possible that approximately 25 more, including the other 3 tidewater glaciers, could have surged in the past (Farnsworth et al., 2016).

2.4 Bathymetry

The sub-bottom profile from Kowalewski et al. (1990) (Figure 1-2) also provides some bathymetric data, though it does not extend all the way to the head of the fjord, stopping just north of Vestfjorden. There, the profile shows a shallow basin, separated from the rest of the fjord across from Surtfjellet by both a rise in the bedrock and a mound of what they have interpreted as glaciomarine ice-front deposits. Beyond that, they characterise the fjord floor as hummocky, interpreted as being the result of additional ice-front deposits. The northernmost and largest of the hummocks is directly across from Nordbreen. In this section, the fjord also deepens to ~140-150 m b.s.l. (below sea level); thereafter, the depth remains relatively consistent.

From recent bathymetric data (Figure 2-6), Forwick et al. (2011) identified glacial lineations and iceberg plough marks in the outer fjord, a series of grounding zone wedges on the plateau, or northern sill (55 m b.s.l., M. Forwick pers. comm.) across from Surtfjellet, moraines just to the south of this, and lineations and drumlins near Vestfjorden in inner Wijdefjorden. The water depth over the inner, narrow sill is as little as 18 m. Immediately to the south, the water is up to 183 m deep, and to the north, the water depth reaches its deepest point (230 m). In the outer fjord, north of Nordbreen, the water depth over the highs is around 110 m, and over the lows, it is up to 182 m (M. Forwick pers. comm.). However, detailed bathymetric data from Wijdefjorden as well as subsequent landform interpretations have yet to be published.

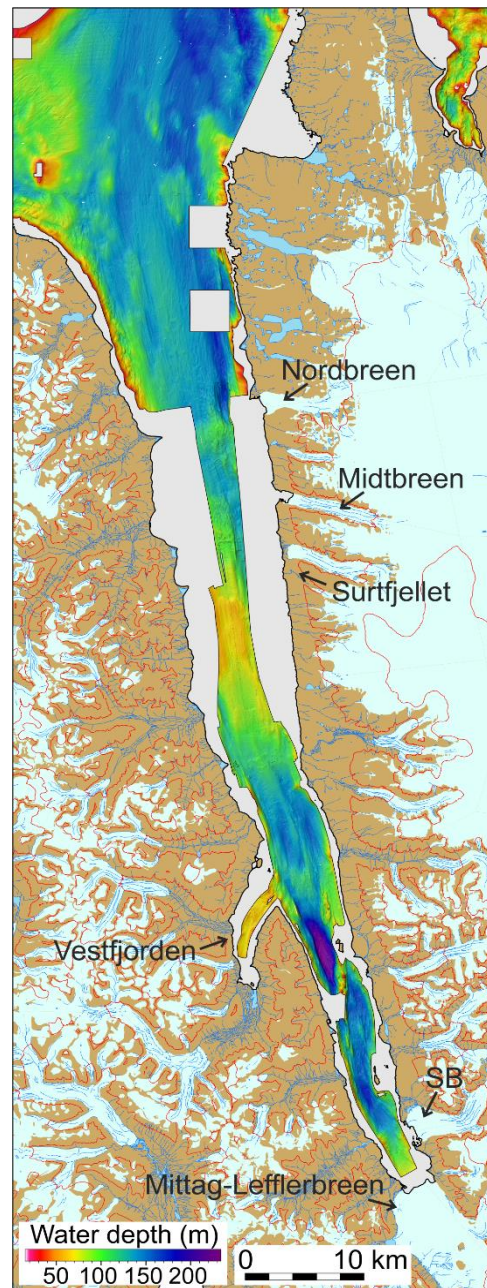


Figure 2-6. Bathymetry of Wijdefjorden. Data from Norwegian Hydrographic Service and M. Forwick (unpublished); figure modified from M. Forwick.

2.5 Oceanography and Hydrography

2.5.1 Currents

Warm Atlantic Water (AW) enters the Arctic Ocean via the West Spitsbergen Current (WSC), a continuation of the Norwegian Atlantic Current (Figure 2-7). The WSC transports AW, Atlantic Intermediate Water, and Norwegian Deep Water (Beszczynska-Möller et al., 2011). Atlantic Water is warmer and saltier than Arctic Water, and is defined as being ≥ 2 °C and ≥ 34.88 psu (Aagaarda et al., 1987; Cokelet et al., 2008). The WSC travels along the shelf break on the west coast of Spitsbergen before splitting into several branches; the Svalbard Branch starts at the northwestern shelf break of Spitsbergen and then follows the northern Spitsbergen slope eastward (e.g., Aagaarda et al., 1987) along the 400-500 m isobath (Cokelet et al., 2008; Koenig et al., 2017).

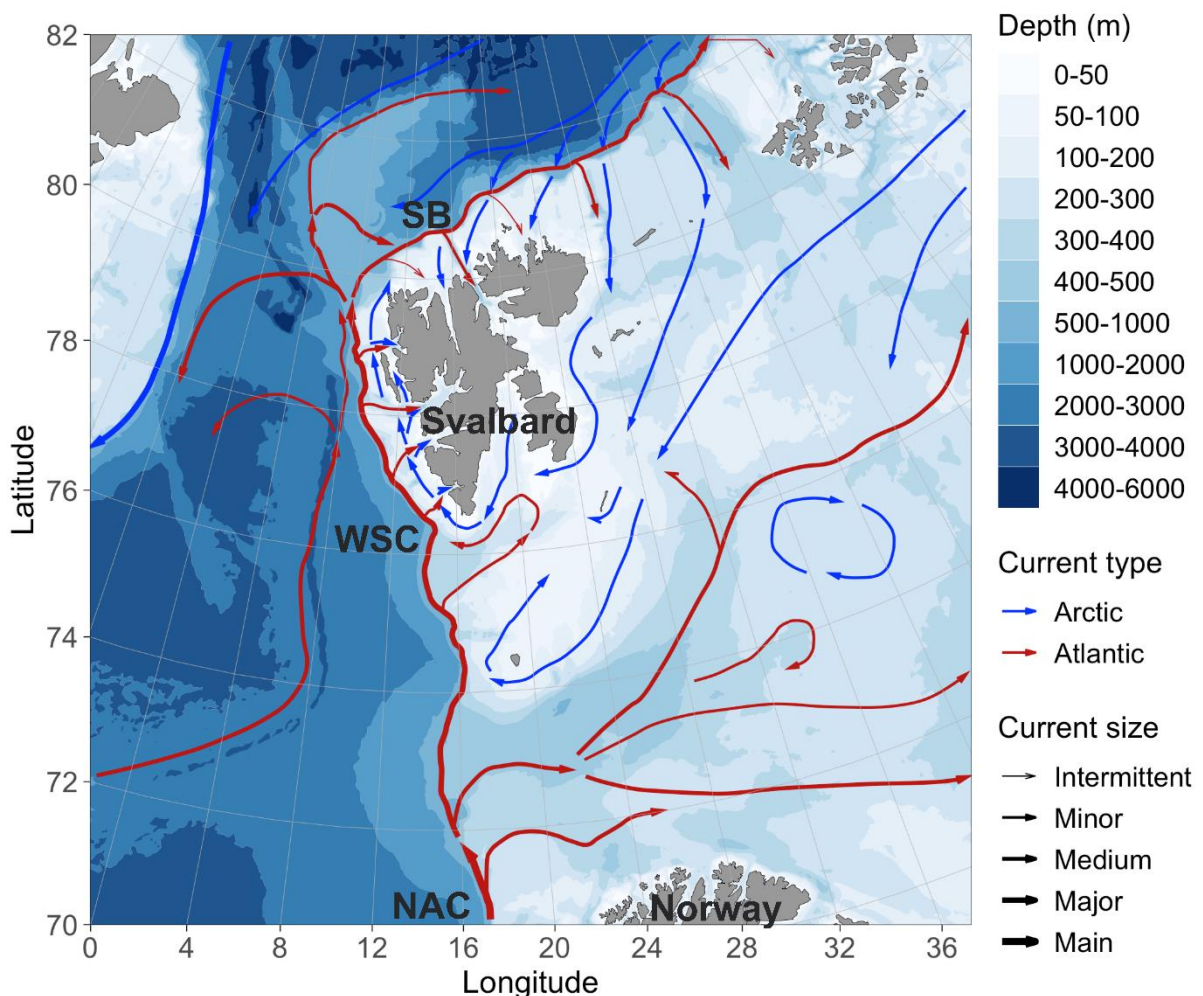


Figure 2-7. Overview map of currents around Svalbard. Created with PlotSvalbard (Vihtakari, 2019). NAC = Norwegian Atlantic Current, WSC = West Spitsbergen Current, SB = Svalbard Branch.

Due to the difference in density between the Svalbard Branch and the Arctic waters of the shelf and fjords, transport mechanisms such as eddies and upwelling are required for the Svalbard Branch waters to reach the shelf and fjords (Cottier et al., 2010, 2005). Eddies form when there is instability at the front between two water masses and can occur with or without a density gradient (Crews et al., 2017). Crews et al. (2017) tracked eddies, which transported AW away from the Svalbard Branch of the WSC, north of Svalbard at 150 m water depth. Their results show that most eddies travel basin-ward and not landward. Upwelling is, therefore, more likely to be a more effective transport mechanism of AW from the Svalbard Branch to the shelf. Little upwelling can occur in periods with heavy ice. However, when ice conditions are low and, therefore, favourable for air-sea interaction, the area north of Svalbard is ideally situated. Here, the prevailing north-easterly winds result in northward Ekman transport of the surface waters and upwelling of the Atlantic Water below (Cottier et al., 2010; Falk-Petersen et al., 2014).

The extent of the Svalbard Branch above the shelf break and into Wijdefjorden has not been well documented, however Crews et al. (2017) show that AW is present at 150 m b.s.l. along the shelf north of Spitsbergen, with an arm extending into the Hinlopen trough and branching west into the Wijdefjorden cross-shelf trough. Since Bartels et al. (2017) identified AW at the mouth of Woodfjorden between ~55-135 m further west, potentially representing an extension of this arm undetected at 150 m b.s.l, AW could be present in Wijdefjorden as well.

2.5.2 Fjord dynamics

Wijdefjorden has not yet been the subject of detailed hydrographic or oceanographic studies and, as such, there is little information available. Fjord hydrography is complex. Fjords with a sill typically have a three-layer arrangement of water masses in the summer, with fresh and warm meltwater at the surface, mid-temperature and -salinity advected water in the middle, and older, salty, winter cooled water that can become deoxygenated at the bottom (Figure 2-8). In the winter, cooling of the surface waters leads to mixing of the water column as they sink (Cottier et al., 2010). The height of the sill has a large influence on the degree of stratification in the fjords, leading to differences in oxygenation and general hydrography (Syvitski et al., 1987). Cottier et al. (2005) and Nilsen et al. (2008) found that this arrangement was also present in two Svalbard fjords (Kongsfjorden and Isfjorden) with no sill. The cross-section through Wijdefjorden from Kowalewski et al. (1990) and the multibeam bathymetry of the fjord mouth from Ottesen et al. (2005) show that there is no fjord-mouth sill; however, there are two sills further in the fjord, one in the inner and one in the mid-fjord, visible in Figure 2-6. Since there

have been no studies on the water masses present in Wijdefjorden specifically, nor how they might change seasonally, how the bathymetry of Wijdefjorden affects the water masses is unknown.

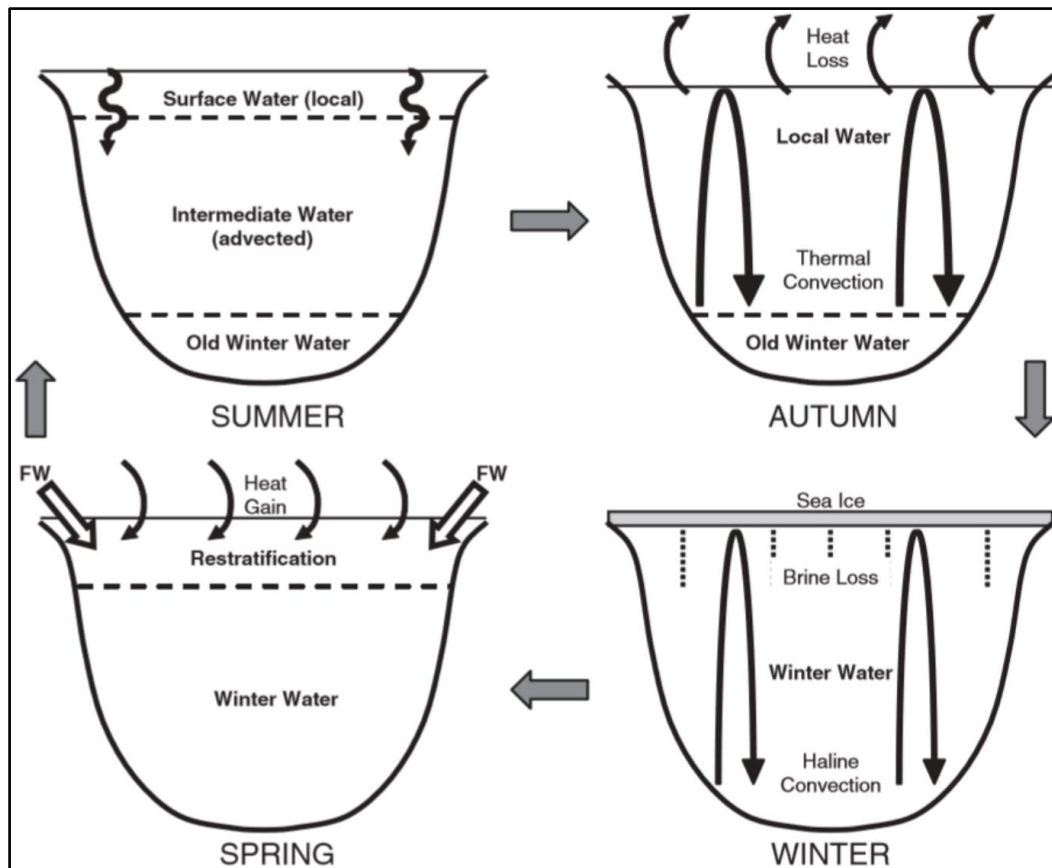


Figure 2-8. Schematic representation of the seasonal water stratification and mixing in shallow (<300 m), arctic fjords (from Cottier et al., 2010).

Circulation of water within a fjord is dependent on several factors including the Coriolis effect. Earth's rotation can lead to a rotational effect as water layers are deflected, to the right in the northern hemisphere. A broad, stratified fjord will experience this as inflowing and outflowing waters will tend to hug their respective right-hand shores (Cottier et al., 2010). This effect is dependent on the Rossby radius, which is defined as the ratio of the speed of an internal wave to the Coriolis parameter.

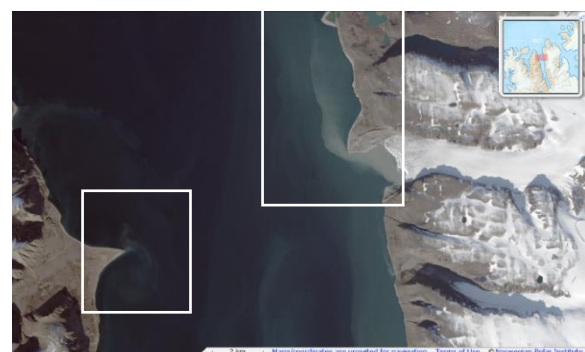


Figure 2-9. Satellite imagery from TopoSvalbard (Norwegian Polar Institute, 2018) showing sediment-laden waters deflected to the right (white boxes) on both west and east coasts of Wijdefjorden. The tidewater glacier on the east coast is Nordbreen.

Internal waves occur only when there is stratification, and the rotational effects will only occur in areas wider than the Rossby radius (Cottier et al., 2010). The Rossby radius for Wijdefjorden cannot be calculated without more information on the water masses, but Wijdefjorden is wide, and as the radius decreases with increasing latitude (Cottier et al., 2005), it likely experiences rotational effects (Figure 2-9).

2.6 Sea Ice

Sea ice around Svalbard begins to form in October or November and recedes around May or June. The sea ice maximum occurs in March and typically extends south of Svalbard (Dallmann, 2015). In addition to the seasonal ice fluctuations, the sea ice extent can vary widely year-to-year (Cottier et al., 2007; Dallmann, 2015) or on multi-year cycles (Walczowski, 2010). The extent of the sea ice is related to many variables, including the temperature of AW, the strength and direction of the wind, and the local bathymetry (Cottier et al., 2007; Dallmann, 2015; Walczowski, 2010). Land fast sea ice in fjords is often present in the winter, however in wider, less sheltered fjords, the land-fast sea ice often breaks off. The outer fjords (e.g., Figure 2-10) are less likely to develop land fast ice (Dallmann, 2015). In late winter, the sea ice from the ocean and the sea ice from the fjords often connect, though this happens less frequently now as the climate warms and AW advection increases (Gjelten et al., 2016).

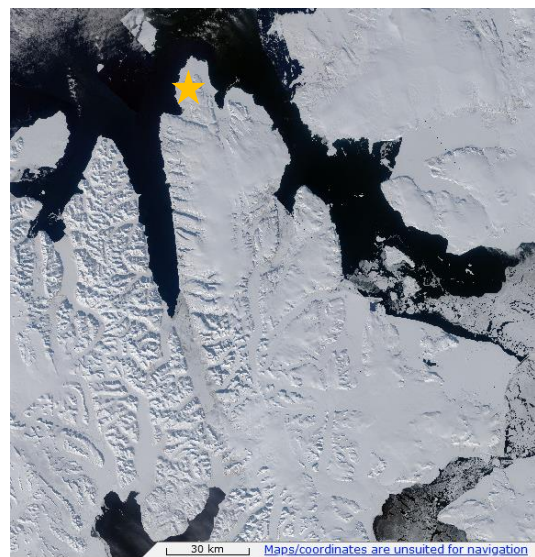


Figure 2-10. Satellite imagery (winter) from TopoSvalbard (Norwegian Polar Institute, 2018) of Wijdefjorden showing the extent of sea ice in the fjord. Yellow star indicates location of Verlegenuken.

2.7 Climate

Svalbard's location means it is influenced by the warm water from the Atlantic (Figure 2-7), and that it is therefore relatively warm considering its latitude. However, sea ice can act as an isolator between the relatively warm water and the land; when present, it leads to Svalbard having a cold and dry continental climate (e.g., Sund, 2008). Compounding this effect, sea ice has a high albedo and reflects much of the incoming solar radiation, leading to less heat storage. In times with little sea-ice, Svalbard has a relatively warm and humid maritime climate

(Førland et al., 2009; Gjelten et al., 2016). The variability of the sea ice cover results in larger changes from one year to another than for other regions at similar latitudes (Førland et al., 2009). The region receives little precipitation, as cold air masses carry little water. There is a precipitation gradient across Spitsbergen, as precipitation decreases from the southwest to the northeast (Førland et al., 2009). The southwest Spitsbergen receives up to ~1200 mm/yr of precipitation, while areas in the northeast generally receive less than 600 mm/yr. Wijdefjorden generally receives less than 400 mm/yr, with less than 200 mm/yr, the lowest values for Spitsbergen, in the centre of the fjord (Hagen et al., 1993) (note: these values are largely based on indirect measurements and are almost 30 years old, thus give only a general idea).

Meteorological stations are sparsely distributed in Svalbard; the majority are on the west coast and along the western fjords of Spitsbergen. Svalbard airport has a long temperature record, beginning in 1898, which shows warming in the area, with an average increase of 0.3°C per decade from 1898 to 2015 (from ca. -7 to ca. -2.5°C). The rate of warming is also increasing; in the last 37 years of the timespan, warming was occurring at a rate of 1.3°C per decade and 2.3°C per decade in the winter (Gjelten et al., 2016). These rates of warming are higher than those of Hanssen-Bauer, who found rates of 0.3°C per decade and 1.0°C per decade, respectively (2002), indicating an increasing rate of warming in the most recent years. This warming is driven largely by the decline in sea ice, higher sea surface temperatures (sst), and general background warming. Warm air masses from the north and east, likely driven by heat exchange from areas of open water in the Barents Sea and the Nansen Basin, also contribute (Isaksen et al., 2016). Projections by Førland et al. (2011) indicate a further 10°C warming by the end of the century, as well as an increase in precipitation. These correspond well to some of the models in Hanssen-Bauer et al. (2019). Current average temperatures at Svalbard airport are about -3°C and the annual precipitation is 190 mm (Elvebakk et al., 2018; Førland et al., 2009; Hanssen-Bauer, 2002). In Wijdefjorden, the average temperature from 1971-2000 was around -16°C to 18°C in the winter, and in the summer it was around -1°C to 1°C (Hanssen-Bauer et al., 2019).

Since 1997, there has been a weather station at Verlegenuken (at the head of Ny-Friesland, Figure 2-10), making it the nearest station to Wijdefjorden. The average temperature in 2018 was about -3°C (yr.no). Region specific climate data are lacking, as there are no meteorological stations in Wijdefjorden. However, in association with the formation of the Inner Wijdefjorden National Park in 2005, biological surveys in the area provide some information. Elvebakk et

al. (2018) determined that, based on the flora in the area, the temperatures are probably similar in range to those at the Svalbard airport, though there is considerably less precipitation. This aridity is likely due to the length and relative narrowness of Wijdefjorden, which can act as a wind tunnel, desiccating the air and soils. Additionally, since the region is surrounded by high mountains, there are rain shadow effects limiting precipitation rates, though these have not been measured (Elvebakk et al., 2018). Rachlewicz (2009), in an investigation into the causes of floods in the drainage areas between Wijdefjorden and Billefjorden, observed very little precipitation and low rainfall intensity (<2 mm/hr) near the head of Wijdefjorden. The area has relatively deep alkaline soils up to 300 m a.s.l. that form only due to long-lasting droughts, supporting those observations (Elvebakk et al., 2018). While Inner Wijdefjorden is unique for these areas of high-arctic steppe, the tributary valleys have less dry conditions and are more normal for Spitsbergen.

3 Materials and methods

This thesis is based on the integration of acoustic (chirp) data and multi-proxy analyses of five sediment cores, the details of which are described here.

3.1 Acoustic Data – Chirp sonar

Sub-bottom profiling is possible with acoustic systems like the chirp, which can produce high-resolution sediment profiles that are free of artefacts in real time (Schock et al., 1989). The chirp sonar systems use a swept-frequency pulse generated by a computer. This pulse is amplitude- and phase-compensated, to limit effects on the vertical resolution and improve the signal to noise ratio (Quinn et al., 1998; Schock et al., 1989). It has a vertical resolution of ~0.125 m and a horizontal resolution of 1 to 2 m (Quinn et al., 1998). The instrument used in this study is the EdgeTech 3300-HM hull-mounted sub-bottom profiler ("Chirp"). The pulse frequency sweep was 2-10 kHz over 20 ms, with a shot rate of 1 Hz. The ship was traveling at a speed of ~4.5-5 knots (Forwick et al., 2017). The line along which chirp data was acquired is indicated in Figure 3-1.

3.2 Sediment cores

This study is based on data from five sediment cores, collected with a gravity corer on the 29th and 30th of July 2017, from the R/V Helmer Hanssen (Figure 3-1). Table 3-1 lists the coring locations, the water depth at each location, and the length of each core recovered. The cores measure 10 cm in inner diameter and were split into approximately meter-long sections on board the ship. All cores were stored in a refrigerated unit (4° C) when not in use. Once in Tromsø, and before they were opened and split into the working and archive halves, all cores were analysed using the multi-sensor core logger and x-radiographs were acquired. After they were split, other analyses and measurements were performed. All methods are described in the following sections.

Table 3-1. Core locations, water depths, and recovery lengths

Station name	Location	Longitude (N)	Latitude (E)	Water depth (m)	Length (cm)
HH17- 1085 -GC-MF	Cont. shelf	80°16.465'	016°12.648'	322	462
HH17- 1091 -GC-MF	Wijdefjorden	79°51.934'	015°22.743'	164	88
HH17- 1095 -GC-MF	Wijdefjorden	79°36.284'	015°28.350'	116	240
HH17- 1100 -GC-MF	Wijdefjorden	79°18.265'	015°46.755'	112	377
HH17- 1103 -GC-MF	Wijdefjorden	79°09.827'	015°57.703'	143	215

Note: The bolded number in the station name is how I will subsequently refer to the cores.

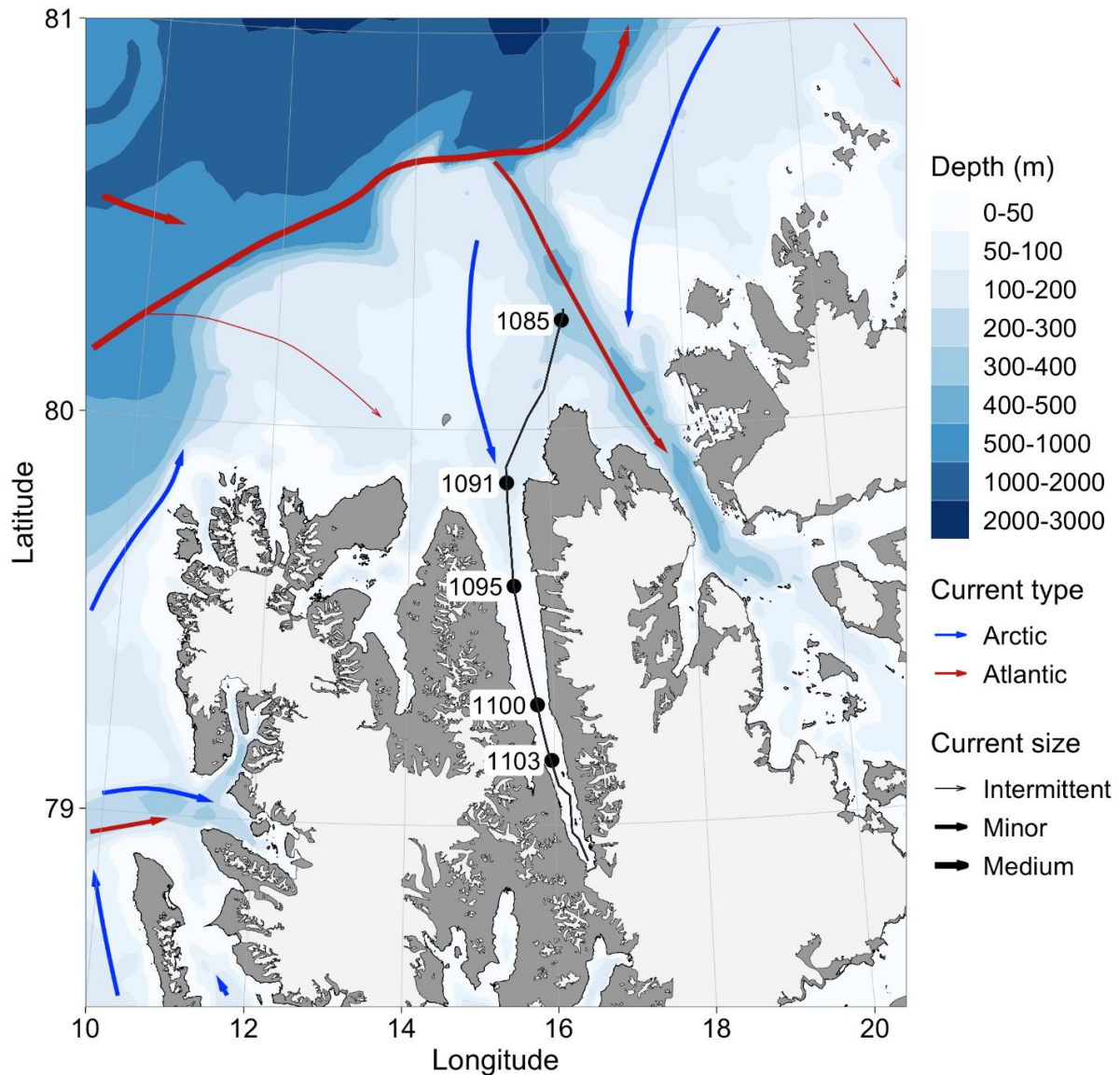


Figure 3-1. Map of Wijdefjorden showing the location of the cores and the chirp line (black).

3.3 Laboratory work

The laboratory work was carried out at the UiT Department of Geosciences laboratory in August and September 2017, and from July 2018 to February 2019, unless otherwise specified.

3.3.1 Physical properties

Each core was logged using a GEOTEK Multi Sensor Core Logger (MSCL) to determine the physical properties of the cores prior to splitting in August 2017 by visiting students Camille Brice and Katharina Lehner. The measured properties include wet bulk density, P-wave velocity and amplitude, magnetic susceptibility, as well as temperature and core diameter. The temperature and core diameter are essential for the calibration of the other physical properties. As the temperature is important, all cores were stored in the lab for at least 24 hours prior to

logging to allow for the temperature to equilibrate. The MSCL operates and takes measurements as each core segment is moved past the sensors by the core pusher in increments of 1 cm, with measurements taken for 10 seconds at each step.

3.3.1.1 Wet bulk (gamma) density

A cesium-137 source emits gamma rays in a narrow beam; as the beam passes through the core, attenuation occurs through scattering of the gamma photons in the beam by electrons in the core. A detector on the other side of the core records the number of photons that have not been scattered; the unscattered electrons will have the same energy as the source, while scattered electrons will not. By measuring the unscattered photons, the density of the core can be measured as the degree of attenuation is proportional to the number of electrons the beam must pass through (Geotek, 2000).

3.3.1.2 P-wave velocity

The MSCL is equipped with an ultrasonic P-wave system, in which a P-wave transducer is located on each side of the core. One transducer acts as the transmitter and sends a short P-wave pulse through the core to the other, the receiver. The travel time of the pulse is recorded, and with the width of the core, which is measured by a displacement transducer to each P-wave transducers, the velocity can be calculated (Geotek, 2000). P-wave velocity varies in sediments; it changes with the porosity, bulk density, and the degree of consolidation of the sediments (Blum, 1997). The P-waves will not travel through air or gas; if, in the path of the P-wave, there are pockets between the sediments and the core liner due to poor coupling, no signal will be received (Geotek, 2000).

3.3.1.3 Magnetic Susceptibility

A loop sensor (Barington MS2C) is mounted on the MSCL. It produces an alternating magnetic field, and any material with magnetic susceptibility will change the oscillator frequency. As the core passes through the sensor, these changes are recorded and transformed into magnetic susceptibility values (Geotek, 2000).

3.3.2 Opening cores

The cores were cut in half lengthwise, using a core-liner saw and an osmotic knife. One half of each core was designated as the archive half, covered with plastic wrap, put in a plastic sleeve, and moved to a refrigerated (4°C) storage area. The other halves, the work halves, were

similarly packaged between analyses and stored in a cold room whenever possible.

3.3.3 X-ray photography

In August and September 2017, Camille Brice and Katharina Lehner took x-radiographs of the split cores. Denser materials absorb more x-rays, while less dense material allows more to pass through. These density contrasts are reflected in the images produced by the machine, and can be caused by sedimentary structures, objects such as clasts and shells, or burrows. Identifying clasts not visible on the surface of the split core is helpful in qualifying the amount of clasts in a core, while shells visible in the x-rays can be more easily found and collected for radiocarbon dating (see section 3.3.7), and burrows are indicative of bioturbation. This information is included in the lithological logs (section 4.2). X-ray images were taken every 20 mm for all cores using the Geotek MSCL-XCT x-ray imaging machine. It uses a source voltage of 120 kV and 225 μ A current. The resulting images were processed using MSCL software. In the processed images, denser material appears darker than lighter material.

3.3.4 Sedimentological descriptions

The surfaces of the cores were systematically described in terms of approximative grain size and sedimentary structures, as well as colour, which was determined using the Munsell Soil Colour Charts. Additionally, any traces of bioturbation and clasts or fossils visible at the surface were noted. These descriptions form the basis for the lithological logs (section 4.2).

3.3.5 Element geochemistry

The opened cores were scanned with the Avaatech XRF core scanner. This scanner uses x-ray fluorescence to determine the qualitative geochemical composition of the cores. The core scanner consists in part of a cathode and a rhodium anode in a vacuum chamber (Avaatech, 2016). When an electric current is passed through the cathode, it heats up and emits electrons toward the anode. This current, as well as the voltage between the cathode and anode, can be changed to modify the number and acceleration of the electrons emitted respectively; higher energies are required to measure the heavier elements (Forwick, 2013). When the electrons collide with the anode, x-rays are emitted. These x-rays are directed to the sediment surface through the helium chamber in the landing unit (Figure 3-2) and interact with the electrons of the atoms of different elements within the sediments. The radiation excites the electrons, which are then ejected from the atoms' inner orbitals, creating a gap in the orbital of each atom. Electrons from outer orbitals move to fill that gap, thereby releasing energy (secondary radiation) in the form of a photon, or fluorescence (Brouwer, 2010; Richter et al., 2006). The

fluorescence travels through the helium chamber to the detector and is what the detector reads. Helium is used in the chamber as it creates less friction with the secondary radiation than air, allowing for better detection, especially of the lighter elements (Avaatech, 2016). Since the energy signature and wavelength of the fluorescence depends on the difference in energy between the two orbitals the electron moved between, the energy of the fluorescence can be used to identify the element from which it came. The amplitude of the resultant energy peaks are proportional to the concentration of each of the elements (Richter et al., 2006). However, limitations of this method mean all results are qualitative.

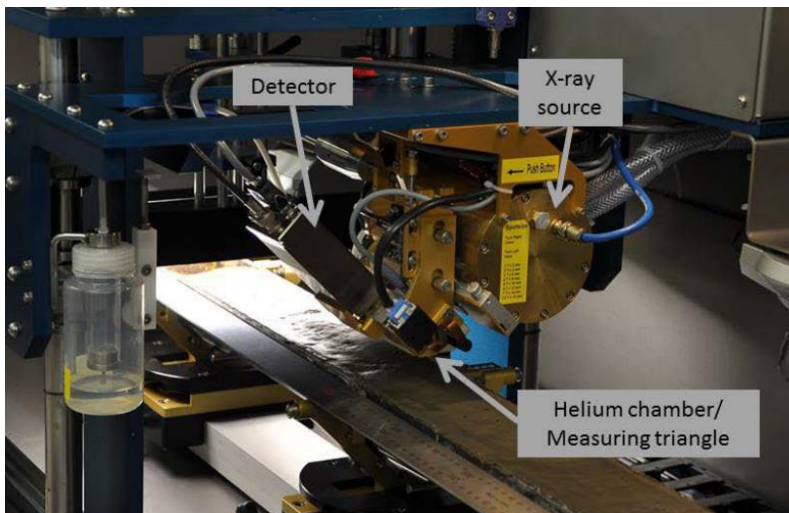


Figure 3-2. Photo of the Avaatech core scanner setup, showing the x-ray source and detector, as well as the landing unit with the helium chamber and the measuring triangle. Modified from Forwick (2013).

The Avaatech core scanner can provide data on the relative changes in element concentrations throughout a core. Herein lies the advantage and disadvantage of core scanning. This method allows for quick and non-destructive analysis of a split core, while other XRF methods require homogenous and dry samples—impossible conditions to meet using an opened core (Richter et al., 2006). However, the heterogeneity of the surface and moisture content of the cores leads to air and water pockets, lowering the number of detected counts (Richter et al., 2006; Tjallingii et al., 2007). These matrix effects are impossible to negate given the characteristics of a sediment core. However, to minimise it, the core surface is carefully flattened and smoothed prior to scanning. A 4 μm -thick foil (Ultralene film) is placed on the sediments to help avoid contamination of the landing unit during the analyses (Brouwer, 2010; Richter et al., 2006).

The analysis of each core segment was conducted in two runs after the cores had time to come to room temperature to avoid condensation accumulating on the film, which can, as described above, lower the number of detected counts. The first run is at a lower energy (10 kV and 1000 μA , with no filter) to capture the lighter elements (Magnesium to Cobalt), and the second

is at a higher energy (30 kV and 2000 μ A, with a Pd-thick filter) for the heavier elements (Nickel to Molybdenum). Both runs had a 10 second measurement time, 10 mm steps between measurements, and the measured area was 10 mm down-core by 12 mm cross-core.

The results for a given element are considered reliable if the counts for that element are above 10000 for the 10 kV run and above 3000 for the 30 kV run. All XRF data are presented as element ratios, either between two elements or of one element over the sum of all other reliable elements. This reduces the matrix effects of surface roughness and water content (Tjallingii et al., 2007), as well as other changes in the cores, such as sediment compaction, that can affect the counts for all elements. Using element ratios can be additionally useful as they can be used to identify changes in the proportion of sediments derived from different sources, using different ratios depending on the geochemistry of the potential sources (Richter et al., 2006).

Line scan imaging

The Avaatech core scanner can also produce high quality line-scan colour images of cores. The camera has three sensors with 4096 pixels each, and each pixel is calibrated on a white ceramic tile before the set of cores are imaged. It produces visual colour images as well as colour data in RGB colour space for each 0.07 mm down-core; only the colour images are used here. Since the cores require similar preparation (they must be smooth and flat) for both the imaging and the XRF scanning, but the removal of the foil used in the XRF scanning can leave marks on the surface, this step was performed just before the XRF scanning to obtain the best photos.

3.3.6 Grain-size analysis

A total of 291 grain size samples from the cores were analysed using the Beckman Coulter LS 13 320 laser particle size analyser. Samples weighing approximately 4 g were taken from a centimetre-wide interval above every fifth centimetre, as well as from the upper- and lowermost centimetre of each core (i.e., from 0-1, 4-5, 9-10, 14-15 cm etc...). These depths correspond to where researchers from the Korea Polar Research Institute (KOPRI) took samples for their research. They did not sample core 1095, but the same pattern was followed. From core 1085, they took additional samples from the following intervals: 401-402, 412-413, 417-418, 422-423, 423-424, and 447-448 cm; these extra intervals were also sampled for grain size analysis.

Each sample was covered with dilute (20%) HCl and left to soak, in order to remove any carbonate material. After 24 hours, the samples were rinsed; to do so, distilled water was added

to each sample, after which they were centrifuged to separate the solids from the liquids. The liquid was then decanted away, after which each sample was flushed with distilled water twice more. To rid the samples of organic matter, the samples were then covered with H₂O₂. The reaction between the H₂O₂ and the organic matter requires heat, so the samples were put in a warm water bath at 85°C for two hours so the reaction could occur. At the end of the two hours, the same rinsing procedure was followed. The remaining sediments were then transferred to a dryer. Once dry, ~0.2 g of each sample was measured out and mixed with 20 ml of distilled water on a shaking table for at least one day to break up any clumps of sediments. Immediately prior to measuring, a drop of Calgon (sodium polyphosphate) was added to the sample, which was then placed in an ultrasonic bath, to break up any clay aggregates that may have formed. The sample was then poured through a 2 mm sieve to ensure no particles too large were introduced into the machine. The Beckman Coulter LS 13 320 laser particle size analyser can analyse particles from 0.04 to 2000 microns. Particles exceeding 2000 microns are included in the lithological logs (section 4.2) as clasts.

The results from the instrument were analysed with GRADISTAT v 8.0, a program that helps with the statistical analysis of results from laser granulometers (Blott, 2010). The Gradistat program defines particles as clay (< 2 µm), silt (2 - 63 µm), or sand (63 µm – 2 mm).

3.3.7 Radiocarbon dating

Macrofossil samples observed at the surface of the split cores, as well as those identified through the x-ray images of the cores, were collected from the sediments (Table 3-2). They were subsequently cleaned over a sieve prior to identification. Three shells were selected for radiocarbon dating based on their quality and condition, as well as their location in the core and proximity to transitional zones or changes in the sediments. Additionally, three areas at transitional zones in the cores with no discernible macrofossils were selected for microfossil (foraminifera) sampling. These sediments were taken from a 1 cm slice of the core, and then sieved. The 100 and 63 µm fractions were kept, dried, and then analysed under a microscope. Of the three sediment samples, only two contained enough datable material. One sample contained almost exclusively *Nonionellina labradorica*, while the other contained a number of species, the two most abundant of which were *Nonionellina labradorica* and *Cibicides lobatulus*. These two were each separated from the rest of the sample and were analysed separately (Table 3-2).

Table 3-2. Radiocarbon sample information and type of analysis

Lab reference	Core	Depth (cm)	Species	Analysis type
AWI 2738.1.1	1095	82-83	<i>Nonionellina labradorica</i>	Gas
AWI 2738.2.1	1095	82-83	<i>Cibicides lobatulus</i>	Gas
AWI 2739.1.1	1103	208-209	<i>Nonionellina labradorica</i>	Graphite
AWI 2740.1.1	1085	221.5	<i>Yoldiella lenticula</i>	Graphite
AWI 2741.1.1	1100	154.5	<i>Macoma calcarea</i>	Graphite
AWI 2742.1.1	1085	326	Unknown	Graphite
N/A	1100	337-338	N/A	N/A

3.3.7.1 Basic principles

Carbon has three naturally occurring isotopes (^{12}C , ^{13}C , and ^{14}C). The most common is ^{12}C , which makes up 98.9% of all carbon (Meija et al., 2016); the remainder is largely ^{13}C (1.1%), with ^{14}C accounting for only ~1 ppm (Bowman, 1990; Meija et al., 2016). Two of the isotopes (^{12}C and ^{13}C) are stable, while ^{14}C is unstable (radioactive). The half-life of ^{14}C is 5730 (Bowman, 1990) and radiocarbon dating can be used to date sample material that is between ~300 and 50 000 years old (Kreienziek, 2018). This radioactive isotope is continuously replenished as it is formed in the upper atmosphere when neutrons, produced by cosmic rays, collide with nitrogen atoms. The production, and therefore the global amount, of ^{14}C varies as solar activity and the strength of Earth's magnetic field, for example, are not constant (Beck et al., 2001; Stuiver and Braziunas, 1989). Once produced, ^{14}C can combine with oxygen to form CO_2 , and then circulate through the carbon cycle. This includes mixing in the atmosphere, dissolution in the ocean and other water bodies, and uptake to plants through photosynthesis and to animals through the food chain and respiration. This continuous carbon exchange replenishes the ^{14}C as it decays in living organisms but continues only while the organism is alive. When an organism dies, it stops incorporating any new carbon and is no longer in equilibrium with the atmosphere. At this point, its radiocarbon clock starts as the $^{14}\text{C}/^{12}\text{C}$ ratio begins to change due to the decaying ^{14}C . By measuring the ratio of $^{14}\text{C}/^{12}\text{C}$ remaining in a sample, one can determine the amount of time that has passed since it stopped incorporating new ^{14}C .

3.3.7.2 Accelerator mass spectrometry (AMS)

The samples were sent to the radiocarbon laboratory at the Alfred Wegener Institute in Bremerhaven, Germany. The lab uses a Mini-Carbon-Dating-System (MICADAS) from Ionplus AG (Gentz et al., 2018). All AMS techniques require the carbon to first be ionized;

here, either a graphite target ($>200 \mu\text{g C}$) or CO_2 gas sample ($20\text{-}100 \mu\text{g C}$) is hit with a cesium beam (Synal et al., 2007). The beams of negative carbon ions are then sent through the low-energy mass spectrometer for mass analysis. The next step is acceleration; the MICADAS uses a small vacuum insulated high voltage platform to accelerate the ions through a high electric field gradient instead of a conventional acceleration tube, which greatly reduces its size (Synal et al., 2007). There is also a gas-filled stripper tube where helium gas interacts with the ion beam, stripping electrons from the atoms and changing their charge from -1 to $+1$ (Kreienziek, 2018; Wiedenbeck, 2015). After this, the beam current of the stable isotopes is measured as it passes through a high-energy mass spectrometer. Lastly, the ions are deflected using electrostatic deflection prior to reaching the detector; more heavily charged ions are deflected more than weakly charged ions. The stable isotopes are detected with Faraday cups and only the unstable ^{14}C ions reach the final gas ionization detection chamber (Synal et al., 2007; Wiedenbeck, 2015).

3.3.7.3 Calibration

The radiocarbon dating results must be calibrated as the concentration of ^{14}C has not been constant through time and ^{14}C years are not directly equal to calendar years (Stuiver and Braziunas, 1989; Stuiver and Suess, 1966). To do this, a record of atmospheric ^{14}C concentration has been compiled using various other ways to date samples, including dendrochronology and Uranium-Thorium dating of stalagmites and corals (Beck et al., 2001; Reimer et al., 2013; Stuiver et al., 1998). Comparing the ^{14}C dates to the dates obtained by the alternative methods provides the basis for the calibration curves (Reimer et al., 2013). Once calibrated, radiocarbon dates, are presented as calibrated years before present (cal. yr BP), where present refers to the year 1950.

The dating of marine samples presents additional challenges, because atmospheric and marine ^{14}C concentrations differ (Mangerud, 1972; Reimer and Reimer, 2016). At the sea surface, gas exchange occurs between the atmosphere and the ocean and the concentrations of the different carbon isotopes are in equilibrium. However, once a water parcel is no longer in contact with the air, the ^{14}C cannot be replenished and its radiocarbon clock starts. Organisms incorporate this old carbon into their shells, resulting in an apparent age older than their true age (Bowman, 1990; Mangerud et al., 2006). The longer the water has been out of contact with the surface, the older it will appear—this is the marine reservoir effect (Mangerud, 1972). The marine reservoir effect changes in space and time, as some areas and periods have more active

ventilation of the surface waters. The strength of the overturning circulation and deep water formation has an impact on this as well (Austin et al., 2011; Bondevik et al., 2006a). For example, it increased shortly after the beginning of the Younger Dryas, before decreasing back to the modern value of ~400 by the end of the Younger Dryas both near Scotland and Norway, though the magnitude of the changes and the timing differs between the locations (Austin et al., 2011; Bondevik et al., 2006a).

To calibrate the radiocarbon ages presented here, CALIB 7.1 (Stuiver et al., 2019) was used. This program uses the marine13 curve for marine samples, rather than adding a marine correction and then using the terrestrial curve, as marine calibration curves have fewer wiggles than the terrestrial counterparts since ^{14}C concentration changes are attenuated in the ocean (Reimer and Reimer, 2016). The curve for the surface oceans between 0-10.5 cal. ka BP was created using the marine atmosphere ocean box model along with the terrestrial IntCal13 curve. From 10.5-13.9 cal. ka BP, it uses several marine ^{14}C data sets including the varved marine sediments from Cariaco Basin and coral data sets. Beyond that, all available data were used, including terrestrial and speleothem data, along with a standard offset of 405 ^{14}C years, representing the global ocean reservoir age, from the IntCal13 curve (Reimer et al., 2013).

In addition to the marine reservoir effect, local differences from the global ocean value (ΔR) cause further discrepancies. The ΔR value varies in space and time (Bondevik et al., 2006b; Mangerud et al., 2006). Calculations of ΔR include measuring the carbon dates of molluscs and whales and comparing those to known years of death (Mangerud et al., 2006), or dating paired terrestrial and marine material from the same depths (Bondevik et al., 2006b). In this study, a Svalbard-specific ΔR of 105 ± 24 is applied after Mangerud et al. (2006) to all samples, as time-varying ΔR has not yet been determined for the region.

4 Results

This chapter contains two main sections: the acoustic data are described first, followed by a description of the data collected from the five sediment cores. The locations of each are shown in Figure 3-1.

4.1 Acoustic data

The chirp sonar data extends from approximately 400 m north of the outermost core (1085) to the head of the fjord approximately 30 km past the innermost core (1103) in ten sections (Figure 3-1). A composite line covering that distance was created (Figure 4-1). The vertical axis shows the two-way time (TWT), or the time it took for the source signal to travel down and back up to the receiver from a given interface.

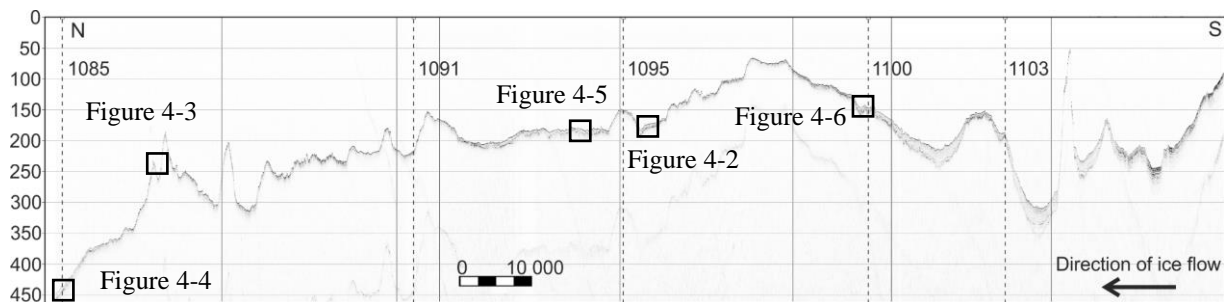


Figure 4-1. Composite section of chirp lines (solid lines indicate chirp line boundary) running SSW from near core 1085 to inner Wijdefjorden, with the approximate locations of the cores indicated by the dashed lines, and the locations of other figures indicated.

4.1.1 Overview

There are two regional reflectors extending throughout most of the 155 km of the composite section. Both become weaker or disappear in some areas but are consistent enough to be described in this subsection. Additionally, there are three distinguishable units that occur in part or all of this section.

4.1.1.1 Reflector R1 and Unit 1

The R1 reflector is the lowermost reflector present in enough of the composite section to be considered regional. It is irregular and varies between being rugged and smooth; in some places there are large (~5-10 ms TWT high, ~50-175 m wide) spikes or mounds (Figure 4-2). It can be diffuse and, therefore, hard to follow in some sections. The R1 reflector defines the top of Unit 1 or Unit 2, except in areas with exposed bedrock (Figure 4-3). Unit 1 (Figure 4-2) is the acoustic basement, so its base is not identifiable. The unit is almost transparent to semi-

transparent, with decreasing transparency higher in the unit. It is generally around 5 ms TWT thick.

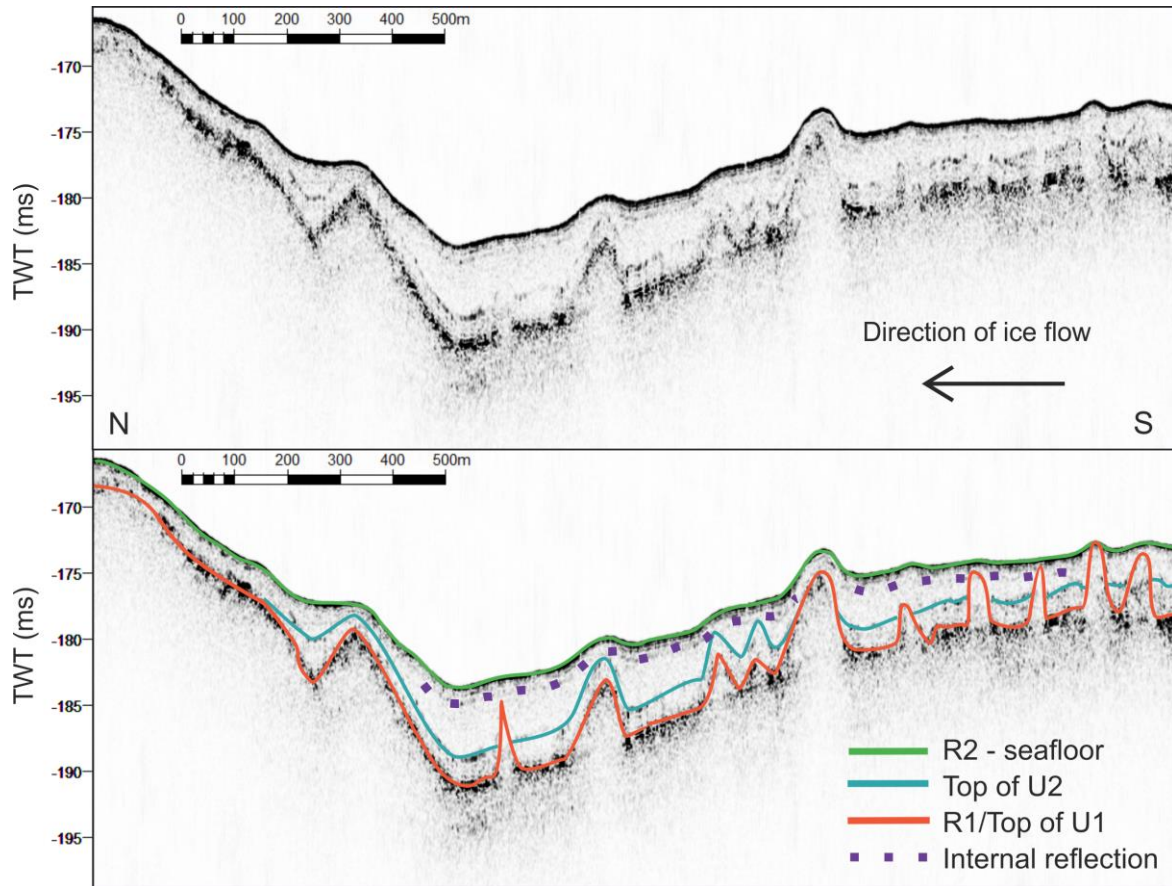


Figure 4-2. Chirp profile with interpretation (lower panel) showing all reflectors and units, with the spikes interpreted as moraines.

4.1.1.2 Unit 2

In some parts of the composite section, an acoustically stratified sequence overlies R1 and Unit 1 (Figure 4-4). This sequence, Unit 2, is typically 2-4 ms TWT thick. It is not continuous, nor is it continuously stratified: in some places, it appears as a chaotic layer (Figure 4-5). It occurs often in conjunction with areas where Unit 1 is irregular as infill between areas of positive relief (Figure 4-2) and occasionally drapes the irregularities (Figure 4-5).

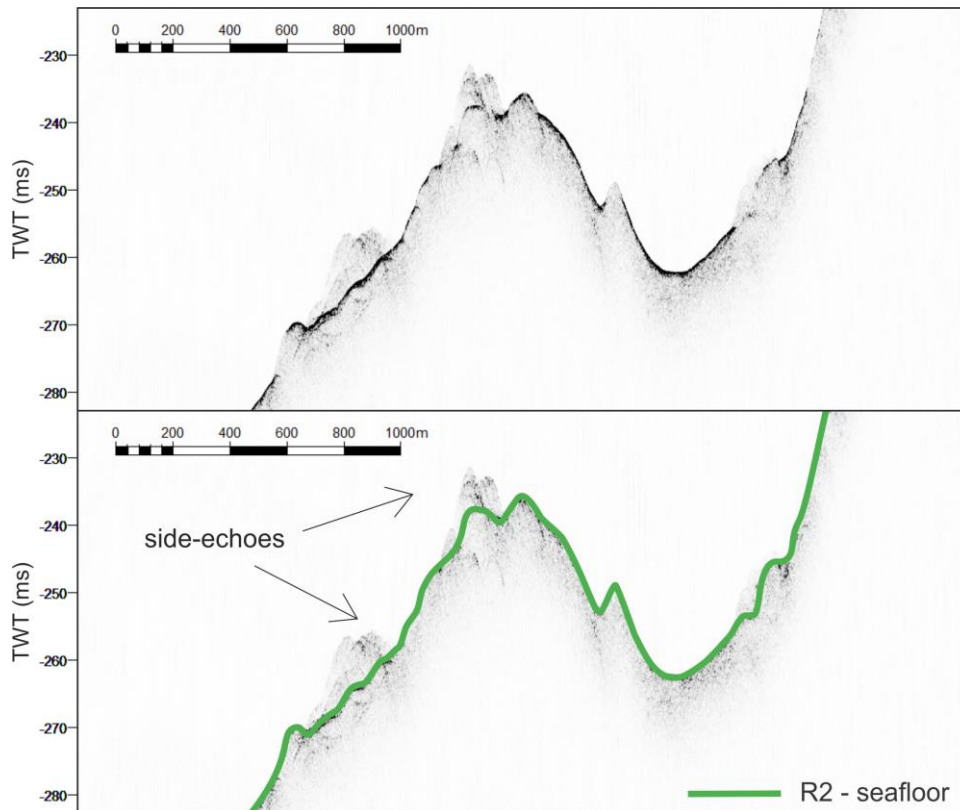


Figure 4-3. Chirp profile with interpretation (below) showing the seafloor reflector where it is immediately above the acoustic basement, and where topographic highs lead to artefacts (side-echoes) (for location of the section see Figure 4-1).

4.1.1.3 Unit 3

Unit 3 is the most abundant unit and is found throughout most of the composite section. It is semi-transparent to transparent. Internal reflectors are common (Figure 4-4) and drape the underlying units, following and often smoothing out the underlying features. Near some obstacles, this unit thins and sometimes pinches out (Figure 4-2). It is typically around 3-6 ms TWT thick, but can be thicker (Figure 4-5), reaching a maximum of ~36 ms TWT thick in the inner fjord.

4.1.1.4 Seafloor reflector R2

The topmost reflector is strong and continuous throughout the section, except for several small areas where it is very weak (Figure 4-3). In these areas, the reflector overlies the acoustic basement. In the north of the section, there are a few occasions where the R2 reflector is overlain by small, acoustically semi-transparent peaks. Since these peaks occur near and mimic topographic highs, they are interpreted as side-echoes (Figure 4-3).

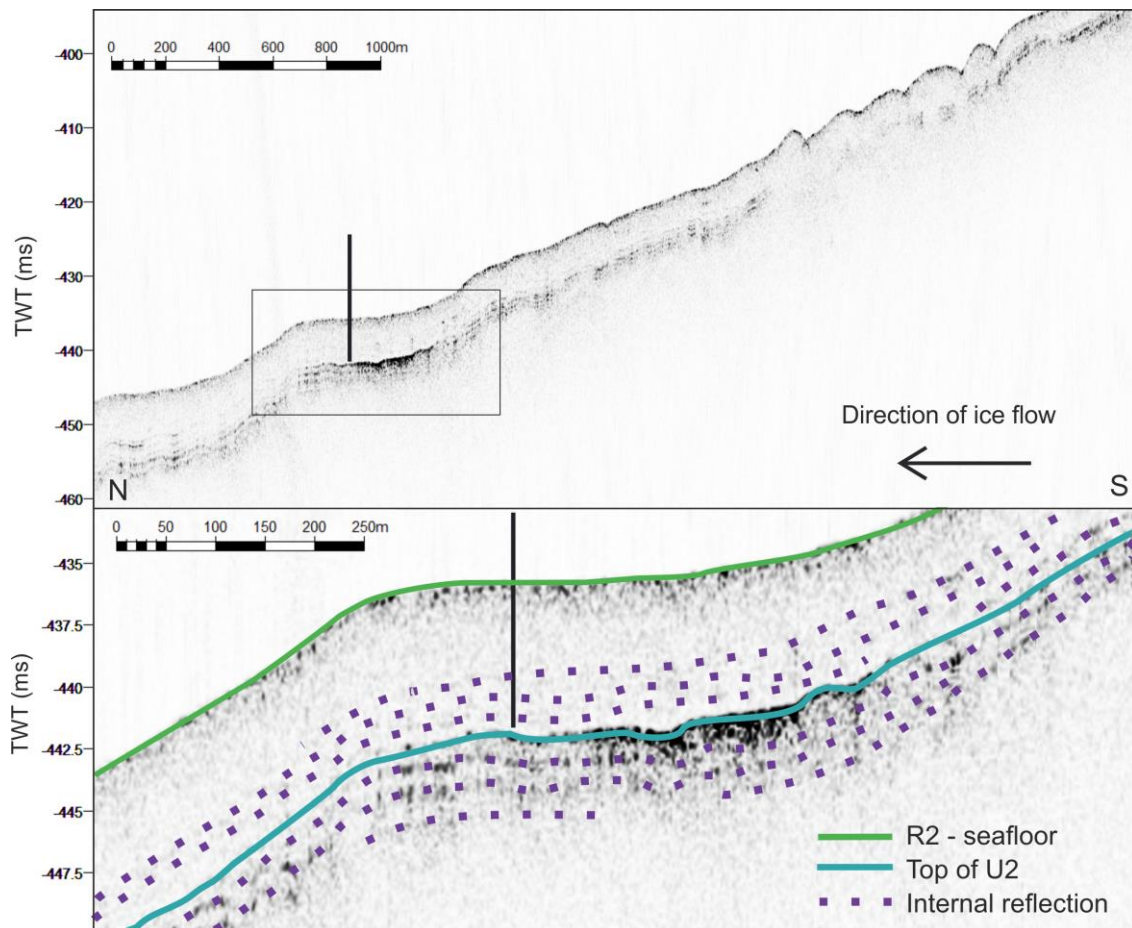


Figure 4-4. Chirp profile with interpretation near the location of core 1085, where Unit 2 rests directly above the acoustic basement (for location of the section see Figure 4-1).

4.1.2 Distribution

Unit 1 is absent in the very north of the profile, however where the bathymetry shallows, U1 appears very chaotic and near to the surface (Figure 4-1, see also Figure 5-1). Subsequently, U1 is lost over the bedrock highs, before reappearing with a similar appearance to the south. Beginning around 5 km north of core 1091, U2 and possibly U3 are present. However, they are often thin and hard to discern. In areas where there are depressions in U1, U2 is thicker, filling them in, allowing for a relatively flat seafloor. This continues until approximately 10 km south of core 1091.

U1 becomes more well-defined south of core 1091 and U2 is present, though it thins and thickens, for about 20 km, until approximately 5 km north of core 1095. When U2 is thinner, U3 is thicker, and has stronger internal reflections. Over the bathymetric high where core 1095 was taken, the sub-bottom profile looks as it does near core 1091. Just to the south of the high, the profile appears as it does to the north. However, it quickly reverts to a thin and chaotic

sequence that continues over the bedrock high until about 3 km north of core 1100. The chaotic U3 sequence becomes thicker in some areas above this high.

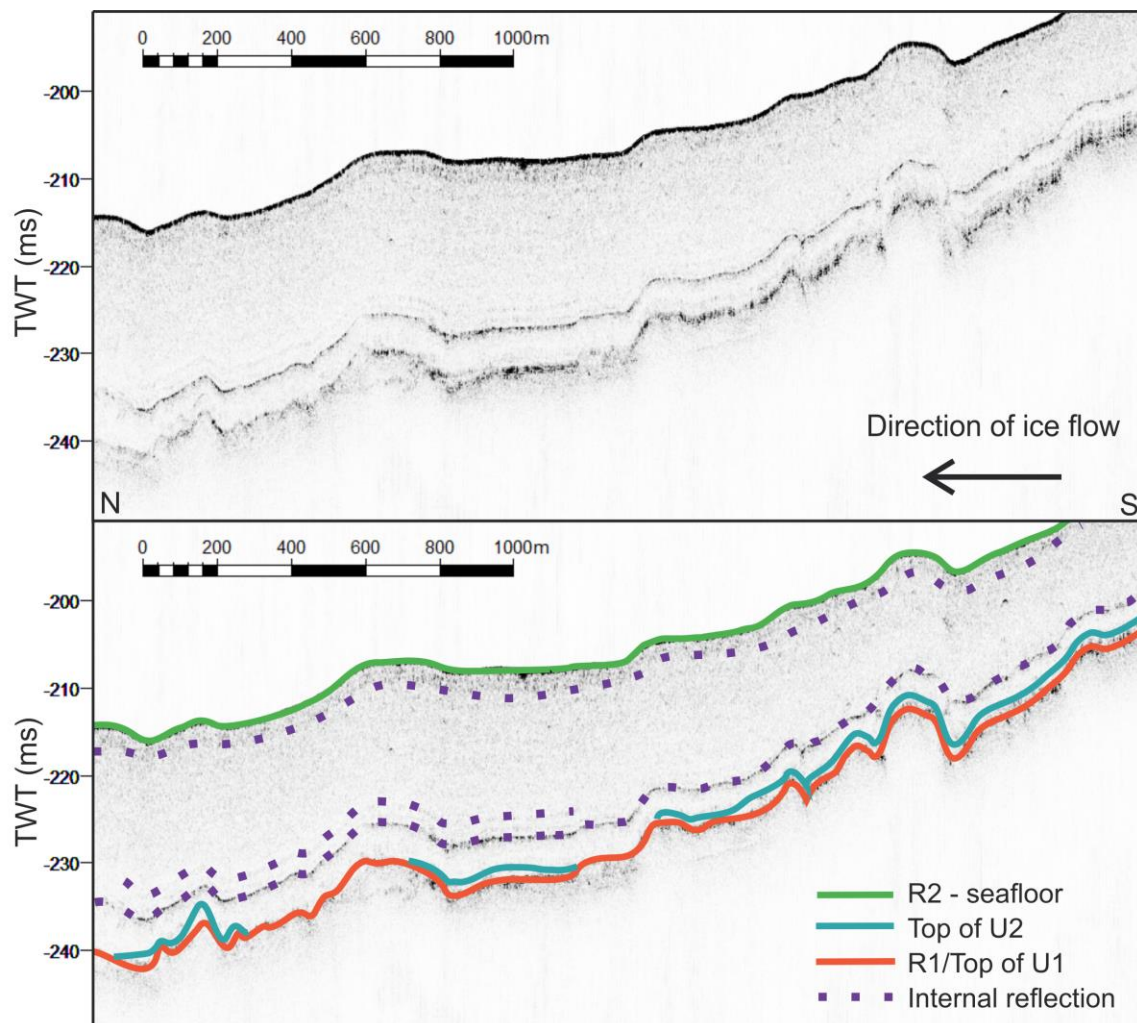


Figure 4-5. Chirp profile with interpretation of an area with a thick Unit 3 with multiple internal reflectors and with areas of Unit 2 overlying Unit 1 (for location of the section see Figure 4-1).

Near core 1100, the U2 and U3 units become thicker and less chaotic. The top of U1 is rough here, with U2 filling in the depressions between peaks, and U3 draping the units below. The units thin and become slightly more chaotic, or less transparent near core 1103. South of core 1103, there are two deep basins separated by a narrow high. In these basins, the sediments are very thick, at up to 39 ms TWT above the U1 reflector. In both basins, there are many internal reflections, and the uppermost ~10 ms TWT are less transparent.

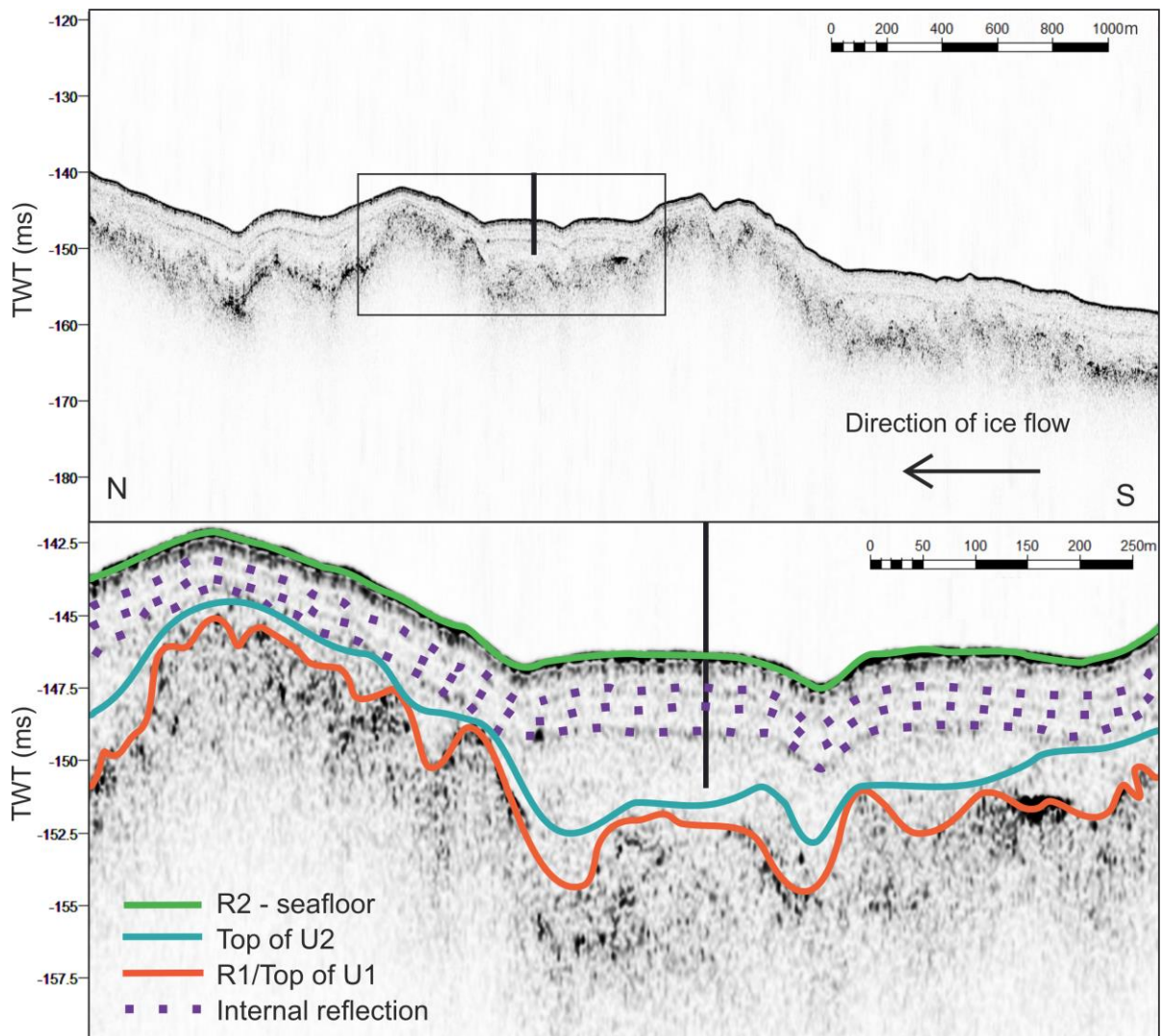


Figure 4-6. Chirp profile with interpretation of the area near core 1100 (for location of the section see Figure 4-1).

4.2 Lithostratigraphic results

Five sediment cores were retrieved from Wijdefjorden and the continental shelf to the north (Figure 3-1). The methods described in Chapter 2 were used to analyse the cores. The results are presented in this section, first as a broad picture of all cores, then in more detail for each core individually. Lastly, all radiocarbon results, and then the sedimentation rate calculations, are presented together. These results in conjunction with the seismostratigraphy results presented above form the basis for all interpretations in the following chapter.

Lithology and stratigraphy

The lithological logs of each sediment core are based on observations of the opened sediment core surface and the x-radiographs, as well as the grain-size data (Figure 4-7). The surface of the cores had visible clasts; some foraminifera, shells, and shell fragments; and colour changes ranging from abrupt to very gradational. Tactile observations, touching the sediments or inserting a pin, gave initial impressions of the grain size composition and sediment density or compaction. The x-radiographs revealed many density contrasts, clasts, and some shells not visible during observations of the surface of the core. The laser granulometry results reveal that silt is the dominant grain size fraction in all cores, with average values between 59 and 77%. The clay and sand contents fluctuate between ~13-20% and ~6-26%, respectively. In some cores, there are significant changes between sections of the core interpreted to be unit boundaries.

Physical properties

The physical properties included in this section are the wet bulk density and magnetic susceptibility of the sediments. At the very top and bottom of core sections the results were anomalous and removed; the results are presented as a continuous plot. P-wave amplitudes were frequently zero in all cores, rendering the P-wave velocity data unreliable. It is, therefore, neither described here, nor considered in the discussion.

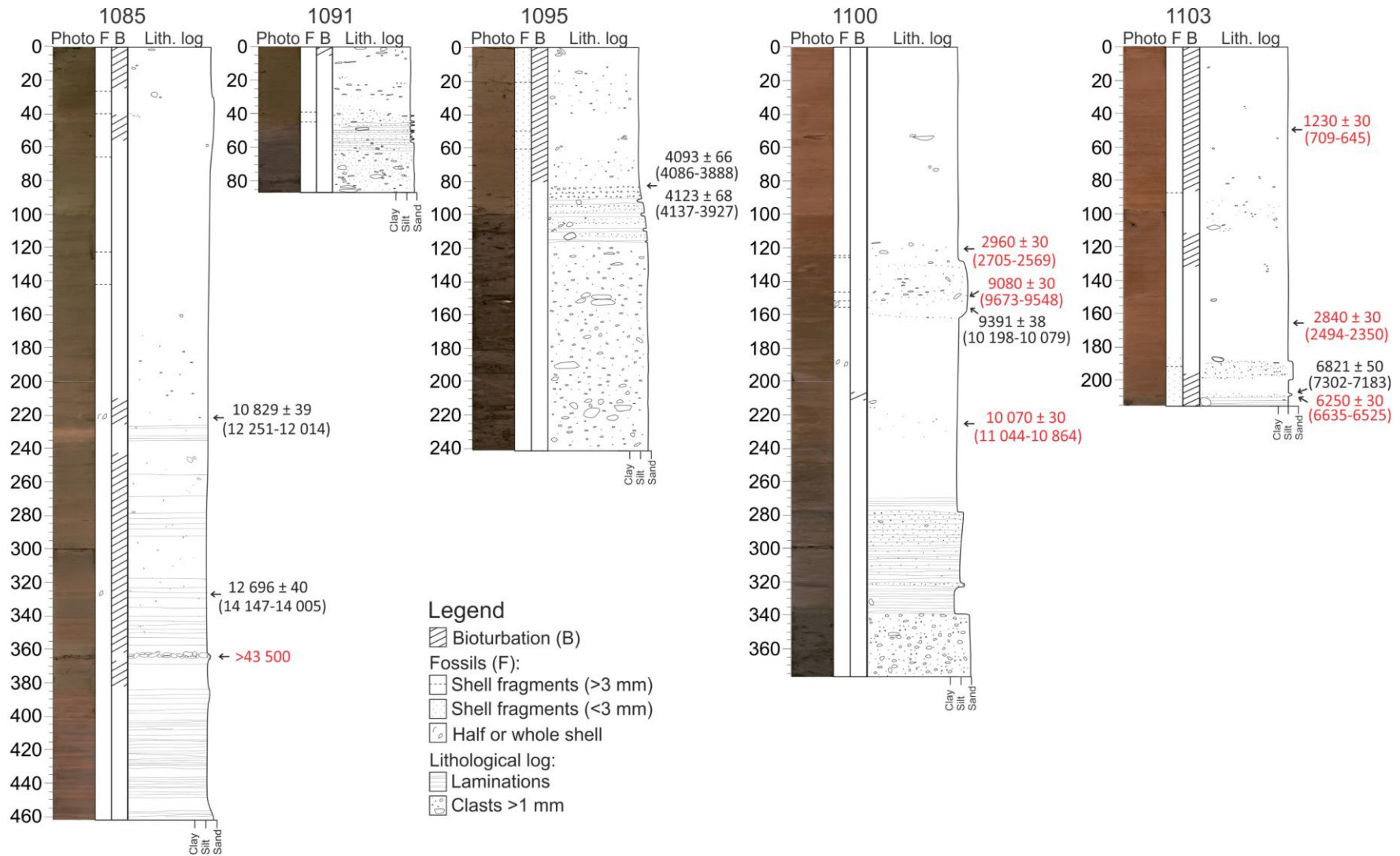


Figure 4-7. Lithological logs of all five cores, from north (left) to south (right). The depth of origin for the dated material is indicated with arrows, and the respective dates (¹⁴C years above and calibrated years B.P. below), including those from S.-I. Nam, pers. comm. (red). Columns show the core photos, presence of fossils (F), occurrence of bioturbation (B), and the lithological log with laminations and the distribution of clasts indicated.

Element geochemistry

The results from the XRF include the nine elements (Fe, Ca, Al, Si (Silicon), K, Ti, Rb, Sr, and Zr) that consistently had reliable counts. In all cores, all element ratios were calculated using the counts for the one element over the sum of all nine elements. The plots for core 1095 (Figure 4-16) have some gaps at 148-152, 165-169, and 215-217 cm. These gaps are due to poor contact between the landing unit and the sediments. Some large rocks protruding from the surface of the sediments had to be temporarily removed from these locations in order for the landing unit to be able to travel the length of the core. Data were considered outliers and removed when the counts changed by more than double between sampling depths in all elements.

Lithological units

Based on the lithology, physical properties, and element geochemistry (see Table 4-1), three lithological units have been identified: L1, L2, and L3. Units L2 and L3 are present in all cores, while L1 is only present in cores 1091, 1095, and 1100. Most properties change primarily at unit boundaries and are relatively similar between the different cores, hence they will be discussed generally in terms of changes by unit. The minimum, maximum, and mean values for the physical properties and select element ratios for each unit of each core are presented in Table 4-1. A schematic depiction of the units is presented in Figure 4-8.

L1 is present in three cores (1091, 1095, and 1100) and has high magnetic susceptibility, high wet bulk density, and high sand and clast content (Table 4-1). It is dark or very dark grey in all cores, however, core 1095 has the reddest undertone, followed by core 1100. The transition to L2 is abrupt and best defined by a decrease in density, observed both when inserting a pin into the sediments and the measured wet bulk density. The unit L2, in addition to having a lower wet bulk density, has higher silt and lower sand content than L1, increasing Ti and Fe/Zr ratios, and typically has lower magnetic susceptibility. There are still abundant clasts, except in core 1100, which has limited clasts until near the top of the unit. L2 is present in all cores and is defined by thin laminations of different colour and density. The transition to L3 is clear in the wet bulk density and the magnetic susceptibility, which both decrease. Other properties increase or decrease at and beyond the mouth of the fjord while doing the opposite in the fjord; for example, outside the fjord, sand and Ca/sum increase while decreasing in the fjord, and Fe/Zr and Ti/Zr decrease outside the fjord while increasing in the fjord (Table 4-1). L3 is generally slightly redder or browner than L2 and is massive, with no more reddish laminations.

Table 4-1. Average values of select properties by unit. *Note: W.b.d stands for wet bulk density and MS stands for magnetic susceptibility.*

		1085		1091			1095			1100			1103	
		L2	L3	L1	L2	L3	L1	L2	L3	L1	L2	L3	L2	L3
W.b.d. (g/cm ³)	Min	1.62	1.57	1.10	1.70	1.65	1.81	1.80	1.49	1.66	1.53	1.53	1.74	1.54
	Max	2.25	1.79	2.31	2.06	1.93	2.44	2.21	1.86	2.13	1.97	1.87	1.90	1.94
	Mean	1.72	1.67	2.04	1.86	1.81	2.21	1.96	1.67	2.04	1.66	1.60	1.80	1.70
MS (SI x 10 ⁵)	Min	19.40	22.70	19.20	26.40	19.40	23.40	48.10	27.70	63.20	31.90	25.90	25.10	21.30
	Max	59.70	33.30	57.30	48.10	34.90	96.30	64.60	85.70	90.10	71.80	49.20	37.60	37.00
	Mean	31.93	26.76	45.73	33.09	31.24	50.64	56.50	42.85	77.99	49.14	33.36	34.26	27.34
Clay %	Min	15.89	11.69	12.16	19.69	7.25	9.51	7.49	12.44	10.53	16.86	10.01	18.28	13.53
	Max	33.28	22.40	21.45	27.93	13.80	16.38	14.22	19.48	14.59	25.06	22.97	19.21	19.94
	Mean	23.22	16.91	16.60	23.83	11.30	11.94	11.59	15.73	12.42	21.69	16.41	18.74	17.39
Silt %	Min	62.96	63.19	37.46	59.96	57.16	44.72	37.30	68.25	44.97	61.48	68.77	74.80	71.26
	Max	76.86	78.25	59.20	70.41	69.95	68.05	68.75	80.49	55.70	77.92	80.63	77.04	80.32
	Mean	70.72	73.87	49.16	64.15	64.19	54.79	57.49	74.65	50.57	70.48	77.21	75.92	76.67
Sand %	Min	0.88	1.46	23.98	1.66	18.08	15.57	17.03	4.54	31.84	0.96	1.56	4.68	3.25
	Max	13.15	24.22	50.38	20.32	35.00	47.92	56.37	19.31	44.41	15.52	21.22	5.99	14.75
	Mean	6.06	9.22	34.77	11.91	24.46	34.22	31.16	9.62	37.00	7.82	6.39	5.34	5.94
Ca/Sum	Min	0.10	0.16	0.07	0.07	0.18	0.19	0.13	0.10	0.16	0.11	0.06	0.09	0.07
	Max	0.47	0.39	0.13	0.18	0.31	0.25	0.23	0.20	0.17	0.19	0.15	0.15	0.16
	Mean	0.19	0.23	0.08	0.10	0.24	0.21	0.17	0.12	0.16	0.16	0.08	0.12	0.10
Fe/Zr	Min	23.36	17.73	15.23	22.41	16.04	12.99	12.36	14.93	10.88	16.40	21.30	34.93	28.25
	Max	72.68	48.60	25.75	46.62	26.42	23.88	27.20	51.32	20.72	49.17	66.15	39.41	73.77
	Mean	44.08	29.06	21.37	33.36	20.25	18.71	20.66	38.51	16.40	34.28	45.78	36.99	58.54
Ti/Zr	Min	2.61	2.05	2.41	3.48	1.82	1.90	1.56	1.38	1.62	1.72	2.42	3.97	2.77
	Max	7.31	4.89	6.56	6.18	2.78	3.35	3.51	5.05	3.20	5.18	6.24	4.73	7.23
	Mean	4.67	3.24	3.63	4.51	2.36	2.59	2.61	3.81	2.63	3.93	4.49	4.29	5.39


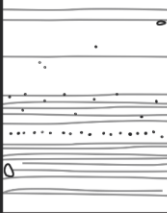
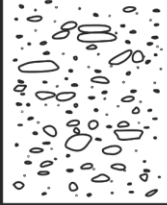
	L3	Glacier-distal
	L2	Glacier-proximal
	L1	Glacial till

Figure 4-8. Schematic depiction of the three lithostratigraphic units. L1 is interpreted as being glacial till. It is dense and has very high clast content. L2 and L3 are glaciomarine sediments, with L2 being the glacier-proximal sediments, and L3 glacier-distal sediments. L2 has laminations or stratifications of sediments with different colours, densities, and element geochemistry. L3 is massive, aside from some clast-rich layers present near the bottom of the unit in most cores. Both L2 and L3 also contain some scattered clasts (IRD).

4.2.1 Continental shelf: core HH17-1085-GC-MF

The core 1085 was retrieved from the continental shelf approximately 50 km north of Wijdefjorden's mouth (Figure 3-1) and is 462 cm long.

Lithology and stratigraphy

The colour of the sediments varies throughout the core (see Figure 4-7, Figure 4-9). The bottom 75 cm of the core are characterized by cyclic changes in colour, changing from dark reddish grey (5YR 4/2) to dark greyish brown (10YR 4/2). Above this, there is a section of 35 cm that is just dark greyish brown, and then wispy dark reddish greys return for 15 more centimetres. The wispy dark reddish grey patches remain but are more diffuse until 277 cm where they stop; meanwhile, the rest of the sediments transition gradually from the dark greyish brown to dusky red (2.5YR 4/2). From 238 cm, the relatively reddish wisps come in again though here they are classified as brown (7.5YR 4/2). By 232.5 cm, the whole core is this colour, and it remains so until 228 cm. Above the brown layer, the sediments return to the dark greyish brown of below. Between 195 to 170 cm the sediments imperceptibly graduate from this colour to weak red (2.5YR 4/2), and the colour then remains consistent through to the top of the core.

The percentages of clay, silt, and sand vary throughout the core, with silt sized grains being the dominant fraction (72.17%). The proportions of the three fluctuate most at the bottom (379 cm-end), with clay ranging from 15.9-33.3%, silt from 62.9-76.9%, and sand from 2.2-13.15%. In

this section we see the maximum clay and minimum silt values, with the respective spikes and dips occurring at the same depths. Above 379 cm, the clay content increases as the sand decreases, and the silt content fluctuates but remains stable overall until 250 cm. In the 249-250 cm sample, the sand content is much higher, and the silt and clay are low. After this, the sand increases gradually, beginning at values similar to those immediately below 250 cm, to its maximum at 19-20 cm (24.2%). The silt content also increases, though not as much as the sands, and then it decreases above 0 cm. The clay content decreases gradually until around 40 cm, after which it fluctuates between 12-14 and 16-19%. At the same time, the sand content fluctuates with differences of ~5-11% between samples in the upper 40 cm.

Clasts are not present until 375 cm and there is another section with no clasts between 160 and

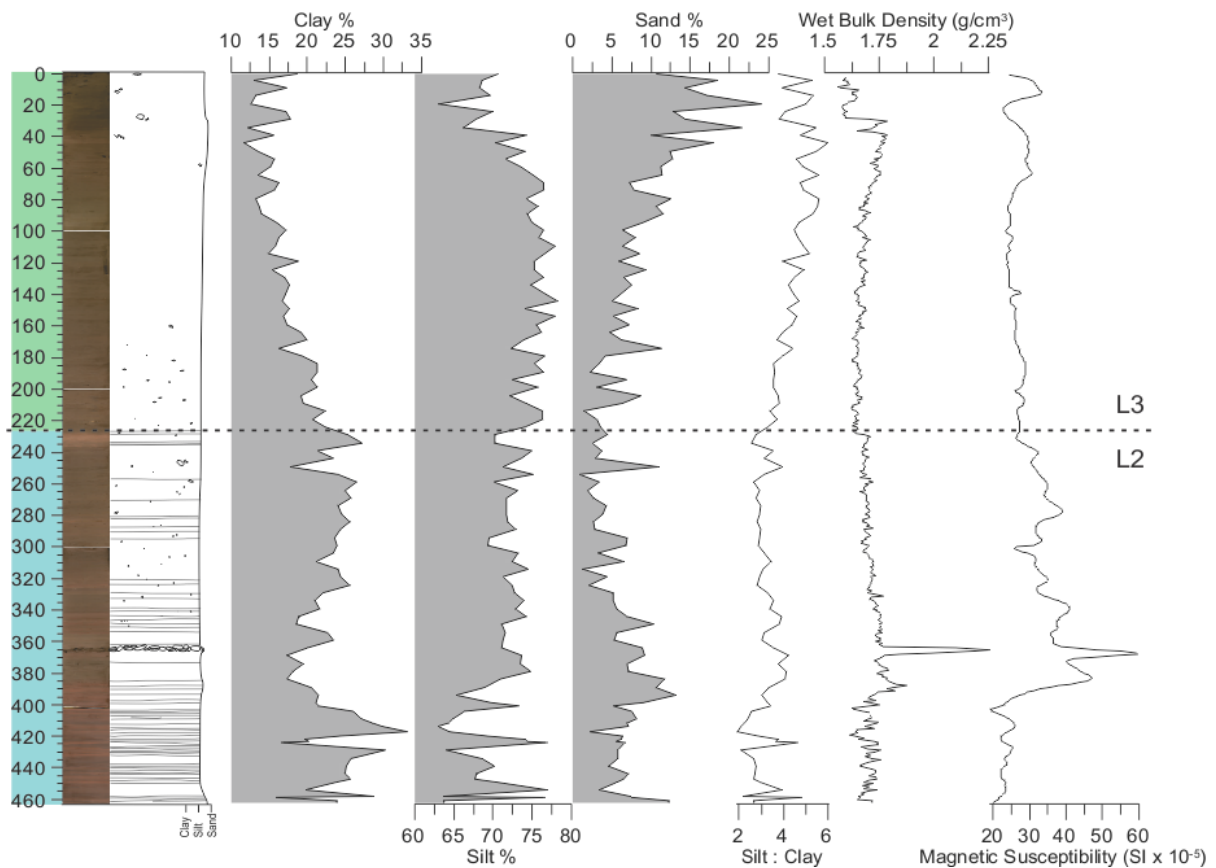


Figure 4-9. Grain size distribution and physical properties for core 1085, with line scan image and lithologic log. Lithological units are indicated.

72 cm. In the rest of the core, clasts are scattered infrequently and often occur singly, with occasional small clusters (Figure 4-10). The interval between 366 and 363 cm is exceptional: it is clast supported.

Some shells are present in the core around 221-222 cm (Figure 4-10) and 326 cm (Figure 4-7). Some shell fragments are present in the top 140 cm. In the upper 24 cm, worm tubes are visible on the split surface of the core, and the x-ray reveals additional bioturbation (Figure 4-10). Another worm tube is visible at 41 cm, but there is no more evidence of bioturbation until 210 cm, below which the bioturbation is almost continuous until around 385 cm (Figure 4-10).

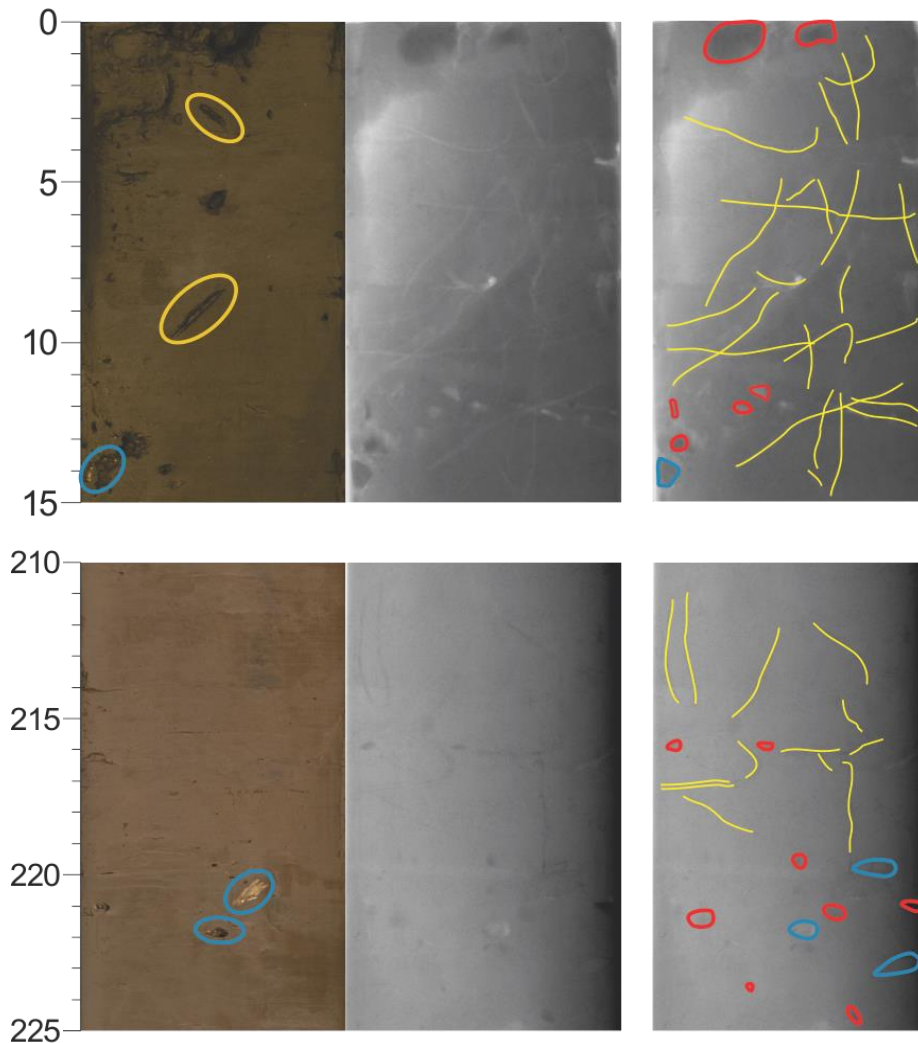


Figure 4-10. Line scan image and x-radiograph with interpretation to the right. On the photo, the yellow and blue circles indicate the location of worm tubes or shells, respectively, that are visible at the surface. In the interpreted x-radiograph, yellow lines indicate the location of burrows, and there are blue or red outlines around shells and clasts respectively. Note: denser material appears darker in the x-radiographs.

Physical properties

The wet bulk density (see Figure 4-9) of the core is generally close to the average of 1.7 g/cm^3 . It fluctuates, without increasing or decreasing, in the lower 60 cm of the core, before increasing

from 400 to 392 cm. Between 371 and 367 cm, values spike to the core maximum of 2.25 g/cm^3 , before returning to around 1.74 g/cm^3 . There is a gradual decrease to 1.62 g/cm^3 at 214 cm and then it remains stable with some fluctuations until 97 cm, before increasing to 30 cm. Throughout, it fluctuates less than in the bottom section of the core except for a larger dip at 36 cm. In the top 30 cm, the wet bulk density values are generally lower than the rest of the core; the core minimum of 1.56 g/cm^3 occurs at 8 cm. The magnetic susceptibility largely follows the same trend as the wet bulk density (Figure 4-9) except for an unmatched low around 302 cm and higher values from 16 to 4 cm. The lowest values (minimum 19.4×10^{-5} SI) occur in the bottom 60 cm of the core, and the high of 59.7×10^{-5} SI is part of the spike from 371 and 367 cm as in the wet bulk density, while the core average is around 30×10^{-5} SI.

Element geochemistry

Below ~405 cm in this core, all elements, when compared to the sum (Figure 4-11), remain stable with some fluctuations except Ca and Rb, which generally increase and decrease, respectively. Between 405 and 366 cm, Fe, Ca, Ti, and Rb continue the same, while Al and K decrease and Sr and Zr increase. From 366 to ~345 cm, Fe continues as before, while Ca, Rb, Sr, and Zr decrease and the rest (Al, Si, K, and Ti) increase. In the next 20 cm, Fe again continues as before while Ca and Rb increase and Al, Si, and Ti decrease. K, Sr, and Zr continue as they did in the section below.

From around 325 to 258 cm, Fe, Ca, K, Ti, and Zr remain stable while Al and Si decrease and Rb and Sr increase slightly. Over the next ~70 cm, Fe, K, Ti, Rb, and Zr increase for about 15 cm, then decrease sharply over 10 cm, before increasing again, sharply for the first 5 cm, and then less after that. Over this same period, Ca does the opposite and Al, Si, and Sr remain stable. Above 186 cm, all elements continue as they did just below, except Fe and Ca, which decrease and increase respectively to ~50 cm below the top of the core. In these last 50 cm, Fe, K, Rb, and Zr increase rapidly in the first ~20 cm before stabilizing; Ca does the opposite. Of the remaining elements, Al and Si decrease, and Rb and Sr increase through to the top of the core. The Fe/Zr and Ti/Zr ratios both fluctuate the most below ~365 cm while decreasing, before stabilizing until ~200 cm, after which they decrease slightly to the top of the core.

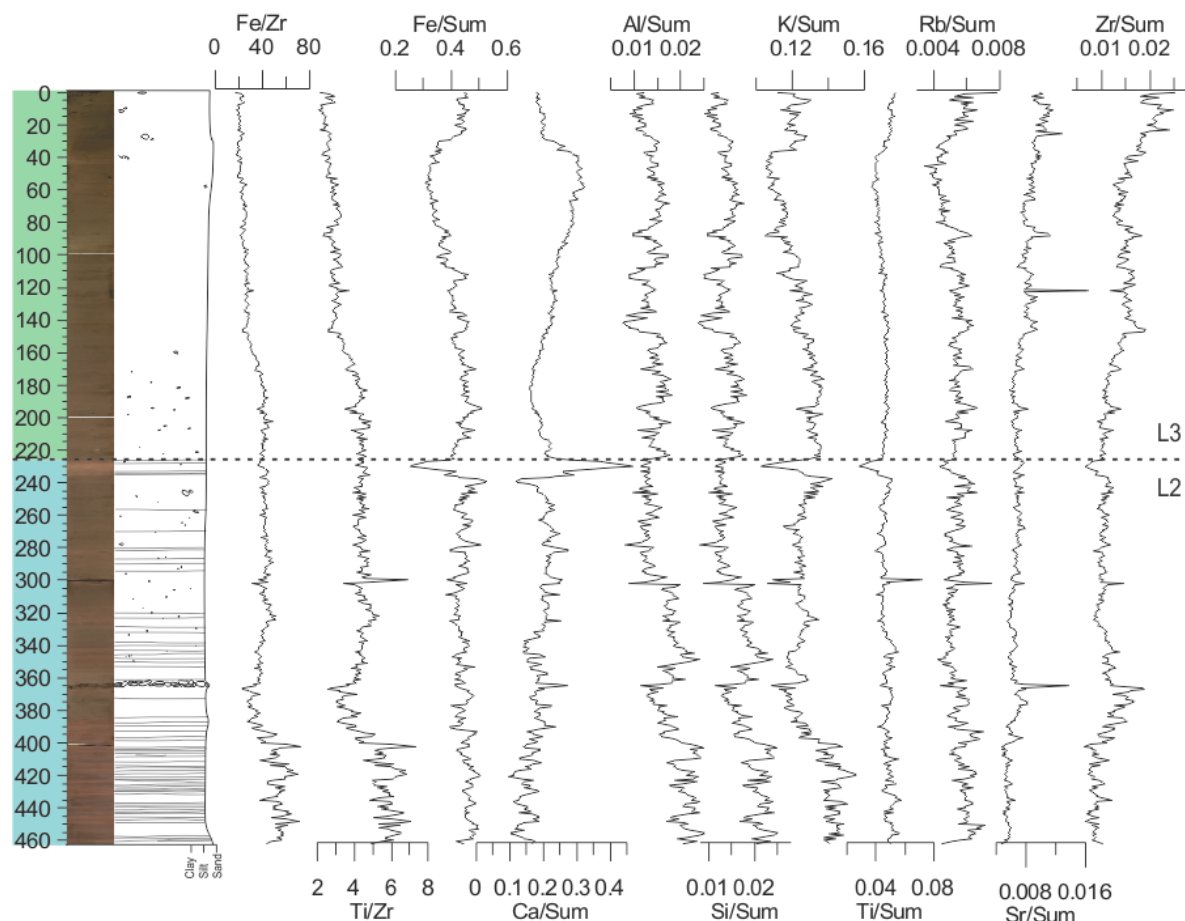


Figure 4-11. Element ratios for core 1085, with line scan image and lithologic log. Lithological units are indicated.

Summary and correlations

The variability in grain size, colour, wet bulk density, and element ratios in the bottom portion of the core reflect oscillating changes of the sediment source. The redder, clay- and Ca-rich layers, dominant in the lowest part of the core, become less frequent, though there are several intervals where they are more prevalent. The dominance of the other sediment source begins to be established in this section. Clasts, absent from the lowest portion of the core, are present only infrequently from within the red intervals to the top of the core, with the exception of a clast-supported layer about one metre from the bottom of the core. This layer corresponds to a spike in magnetic susceptibility and wet bulk density but little change to the element geochemistry. Core 1085 comprises two units: L2 and L3. Unit L2 extends from the bottom of the core to the top of the last reddish lamination at 228 cm, and L3 extends from 228 cm to the top of the core. Radiocarbon dates for this core are from within one of the intervals where the redder sediments are dominant and then from just above the last of the red layers.

4.2.2 Fjord mouth: core HH17-1091-GC-MF

The 88-centimetre-long core 1091 was retrieved from near the fjord mouth (Figure 3-1).

Lithology and stratigraphy

The bottom of the core is very dark grey (7.5YR 3/1) and it transitions to dark greyish brown (10YR 4/2) between 57 and 47 cm. In this transition, there are also brown (7.5YR 4/3) wisps and laminations that appear pink in comparison with the surrounding sediments. From 47 to 41 cm, the colour transitions in an alternating fashion between the dark greyish brown and very dark greyish brown (2.5Y 3/2). From 35 cm to the top, it is consistently very dark greyish brown (2.5Y 3/2).

The clay content of the core is relatively stable (Figure 4-12), with a peak in the samples from 49-50 cm and 54-55 cm where it makes up 26-28% of the sediments. It accounts for between ~17 and 20% of the sediments below this point, except at 69-70 cm and in the bottommost sample (87-88 cm), and consistently less (~7-14%) above. Silt is the most abundant grain size except for its minimum value (37.2%) from the bottommost sample. It, like clay, is low at 69-70 cm and has higher values in the samples from 49-50 cm and 54-55 cm, however it stays close to these higher values through to the top of the core, unlike clay. Both have slightly lower values in the samples from 19-20 and 24-25 cm, as well as in the uppermost sample (0-1 cm). The sand content of the core is high when silt and clay are low, and low when they are high. The minimum of 1.65% occurs at 49-50 cm and the maximum of 50.4% at 87-88 cm. The average of the values below 55 cm is higher than that above 49 cm. The silt to clay ratio is around ~2-3 below 49 cm and around ~5-7 above. Clasts are very frequent below 60 cm and common from 60-40 cm (Figure 4-14), in the interval between 32-22 cm, and in the top 10 cm. Between those intervals, clasts are not present.

Visible shell fragments occur in two sandy layers, at 42 and 45 cm but are absent from the rest of the core. There is limited bioturbation in the top 10 cm of the core only (Figure 4-7).

Physical properties

The wet bulk density (Figure 4-12) fluctuates while generally increasing to the core maximum of 2.31 g/cm³ at 68 cm. It decreases quickly, with some fluctuations (Figure 4-12), to a low of 1.70 g/cm³ at 52 cm before increasing slightly, after which it decreases less rapidly to the top of the core. The magnetic susceptibility follows a similar trend, increasing from the core

minimum of 19.2×10^{-5} SI at the bottom to a double peak of 57.3×10^{-5} SI and 56.1×10^{-5} SI at 72 and 66 cm respectively (Figure 4-12). It decreases to a new low of around 26.5×10^{-5} SI at 50 cm. The magnetic susceptibility then increases by 8×10^{-5} SI to 44 cm, after which it gradually increases to the top of the core, before decreasing sharply by 15×10^{-5} SI in the last 7 cm.

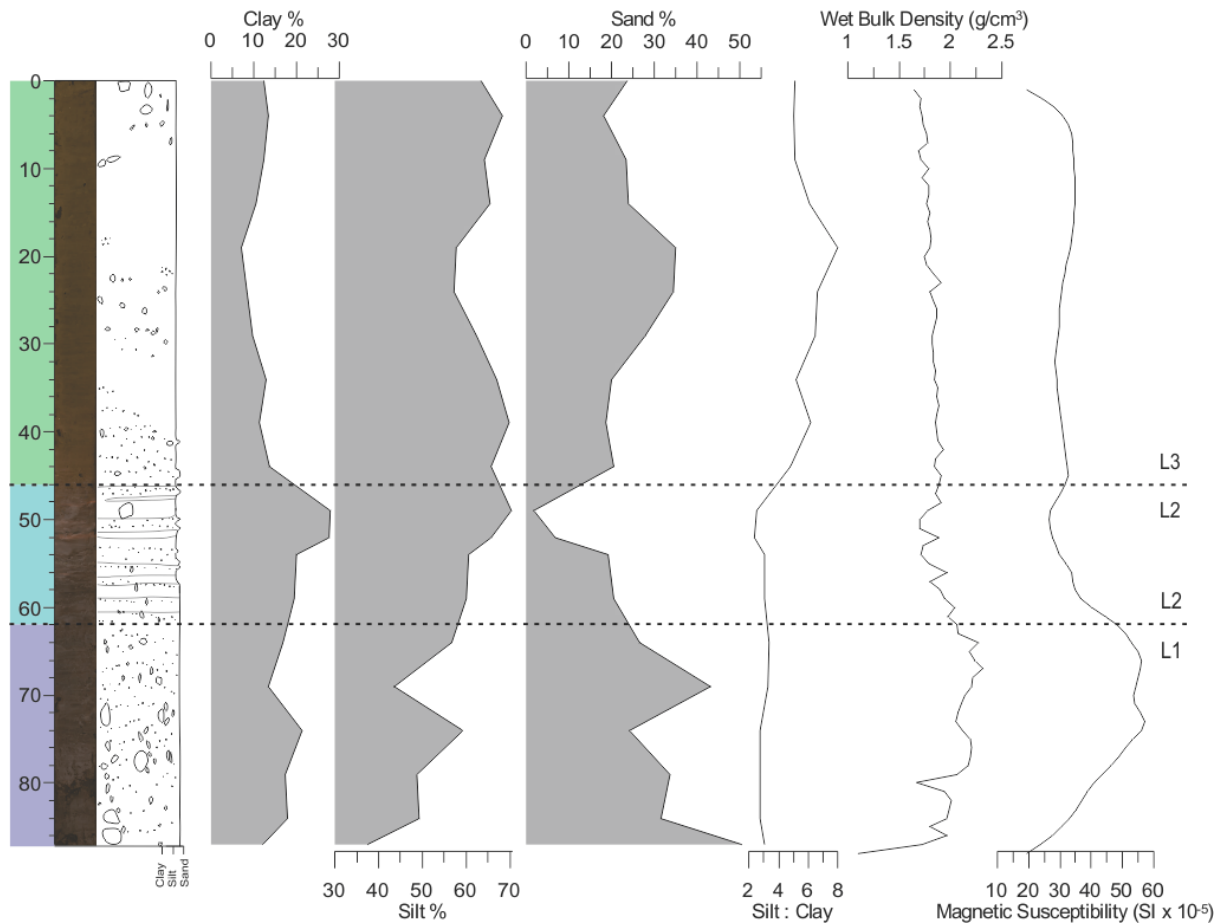


Figure 4-12. Grain size distribution and physical properties for core 1091, with line scan image and lithologic log. Lithological units are indicated.

Element geochemistry

The core can be divided into three sections with different characteristics, the bottom (88-62cm), the middle (62-46.5 cm), and the top (46.5-0 cm). In the bottom most included elements divided by the sum are stable (Figure 4-13), with only minor fluctuations except for the bottom 10 cm where Ca, Rb, Sr, and Zr have a peak, and Al, Si, and K dip. In the top, the element over sum ratios are also very stable and generally steady. Here, Ca decreases slightly, and Fe, Rb, Al, Si, and K increase slightly. In the middle section, the different elements exhibit one of three behaviours: they decrease (Ti) over the whole interval; they remain stable until 51 cm, then

decrease (Fe, Al, Si) or increase (Ca, Sr) until 46 cm, after which they stabilise at the new level; or they increase (K, Rb) or decrease (Zr) to a maxima/minima at 52-53 cm before decreasing/increasing again. The Fe/Zr and Ti/Zr ratios both are fairly stable below 62 cm and above 46.5 cm, and have a jagged peak between those points.

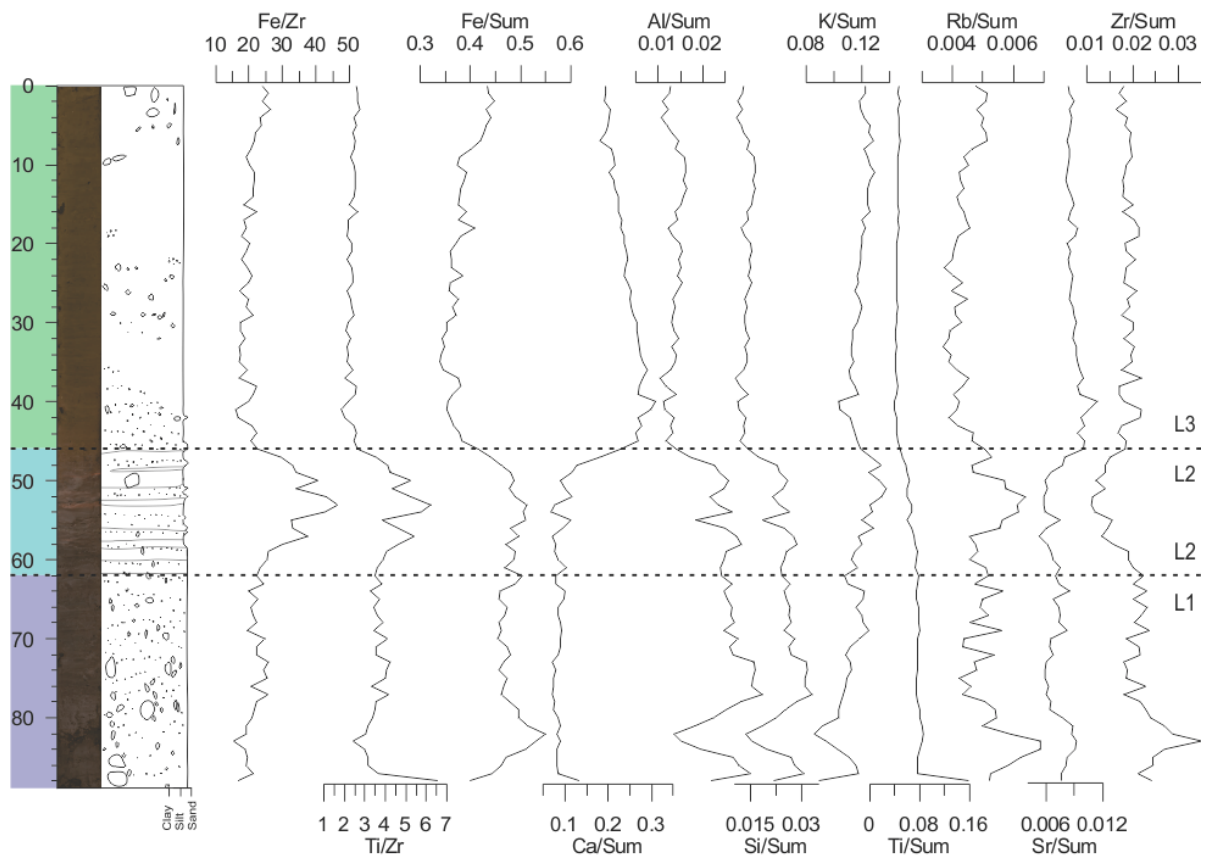


Figure 4-13. Element over sum ratios for core 1091, with line scan image and lithologic log. Lithological units are indicated.

Summary and correlations

The core undergoes a marked change between 62 and 46.5 cm. Below this, the core is dark, clast-rich, sandy, and rich in Fe, Al, and Si. Above, it is more brown, rich in Ca, Sr, and Zr, with fewer clasts, sand and clay, and more silt. These changes indicate a transition away from a system dominated by sediments with a terrestrial source. There are a few small reddish intervals in the middle of the transition similar to those in core 1085, likely indicative of sediments from a different location (Figure 4-14). Core 1091 includes all three units (L1-L3). L1 extends from the bottom of the core to 62 cm, L2 from 62-46.5 cm where the reddish laminations occur, and L3 from 46.5 cm to the top of the core. No datable material was retrieved from this core.



Figure 4-14. Line scan image and x-ray of the L2 in core 1091, showing the changes in colour and density associated with the laminations that define that unit. Also visible is the effect of coring dragging down the edges, and at ~50 cm is a clast, interpreted to be a dropstone, with disturbed laminations below. Note: denser material appears darker in the x-radiograph.

4.2.3 Outer Fjord: core HH17-1095-GC-MF

The core 1095 was retrieved from outer Wijdefjorden (Figure 3-1); 240 cm were recovered.

Lithology and stratigraphy

The core is consistently dark grey (7.5YR 4/1) from the bottom to 100 cm, aside from a centimetre-thick dark reddish grey (5YR 4/2) layer at 115 cm and a few red wisps above this. Above 100 cm, the core is brown (7.5YR 4/1). The end of the core section also occurs at 100 cm, so the character of the colour transition is impossible to determine, though it must have occurred over a small interval.

The distribution of clay in the core is fairly consistent, with clay accounting for ~10-15% of the sediments <2 mm throughout the bottom of the core, rising slightly to 15-20% of the sediments above 100 cm. Below 100 cm, the silt and sand contents both fluctuate inversely to each other, increasing or decreasing by up to 30% (silt) and 35% (sand) between samples. The sand content ranges from ~21 to 56% with an average of 35%, while the silt content ranges from 36 to 68%, with an average of 54%, in this section. They are much more stable above this point, and the sand content is generally much lower (average of ~12%), and the silt higher (average of ~72%), than below. The sand content decreases slightly while the silt content increases slightly through to the top of the core. The silt to clay ratio varies around the average of ~4.6 throughout the core. Clasts are abundant in the lower 105 centimetres of the core. Between 105 and 84 cm, there are multiple gravel layers with few larger clasts. In the upper 84 cm, clasts are present but much less frequent.

There were shell fragments at 21, 50, and 58 cm, and many foraminifera visible on the sediment surface in the upper 105 cm (Figure 4-7). Bioturbation was also consistently present in the upper 105 cm but not below.

Physical properties

The wet bulk density (Figure 4-15) is consistently around 2.1 g/cm^3 with a total range of $\sim 1.8\text{-}2.4 \text{ g/cm}^3$ below 116 cm. Above this, it decreases quickly over $\sim 20 \text{ cm}$ and then remains stable at around $1.6\text{-}1.7 \text{ g/cm}^3$ with some fluctuations. The magnetic susceptibility of the core shows a strong peak ($96 \times 10^{-5} \text{ SI}$) at 232 cm, after which magnetic susceptibility values are stable around $50 \times 10^{-5} \text{ SI}$, with minor fluctuations until a double peak with maxima of 64.6 and $60.4 \times 10^{-5} \text{ SI}$ at 107 and 96-96 cm respectively (Figure 4-15). Above this, the magnetic susceptibility decreases steadily to around 60 cm. From 60 to 45 cm, it is stable around $\sim 27.7\text{-}27.9 \times 10^{-5} \text{ SI}$, before increasing more quickly to the top of the core. The magnetic susceptibility decreases in the uppermost three centimetres of the core.

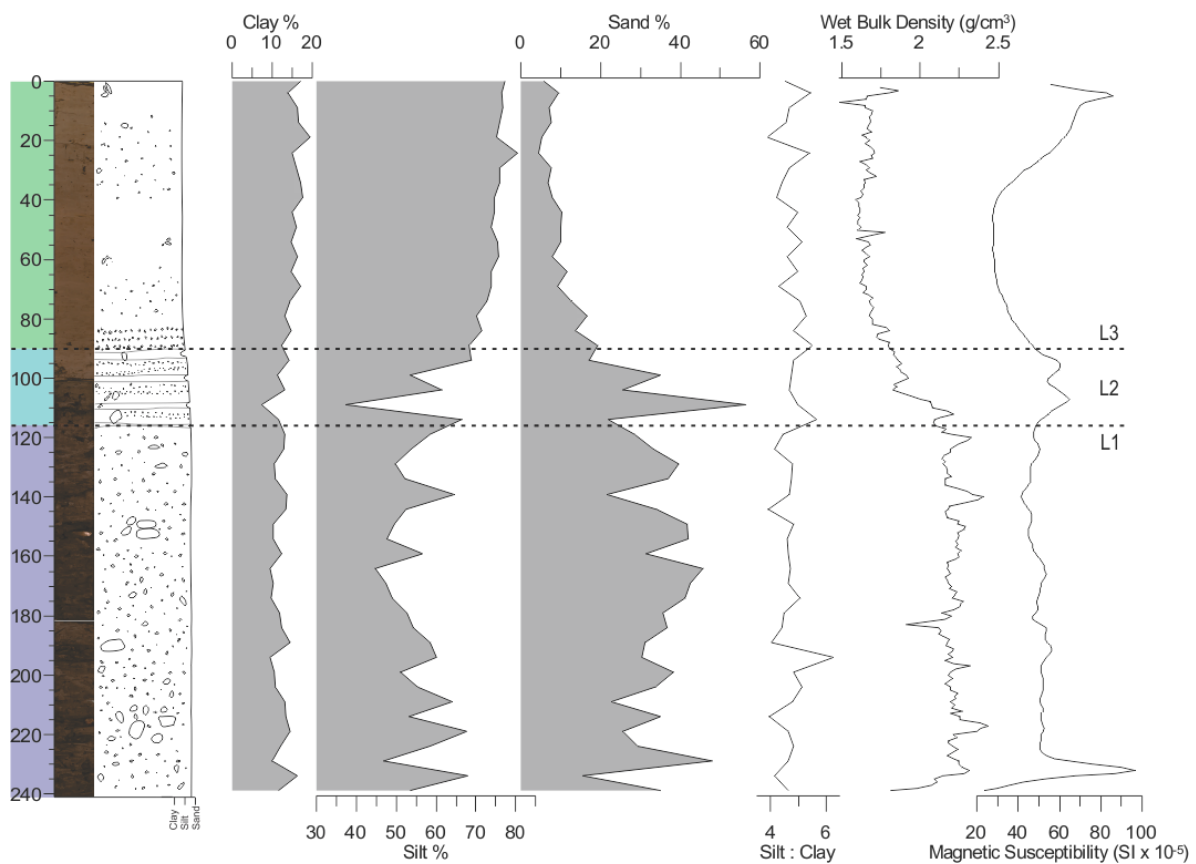


Figure 4-15. Grain size distribution and physical properties for core 1095. Lithological units are indicated.

Element geochemistry

In this core, the Al, Si, K, Ti, Rb, Sr, and Zr to sum ratios remain relatively stable throughout the core, with a peak (Al, Si, K) or dip (Ti, Rb, Sr, Zr) at 137 cm, and with a section of multiple peaks (Al, Si, K, Ti) or dips (Ti, Rb, Sr, Zr) between 116-87 cm (Figure 4-16). The Ca and Fe to sum ratios behave slightly differently than the rest. They both have a peak at 137 cm as the others do, but consistently decrease (Ca) or increase (Fe) over the 116-87 cm interval. Both stabilise after this change, with only minor fluctuations except for an additional Ca peak at 6 cm. The Fe/Zr and Ti/Zr ratios both are stable to 116 cm, fluctuate more until 87, after which they rise through to the top of the core.

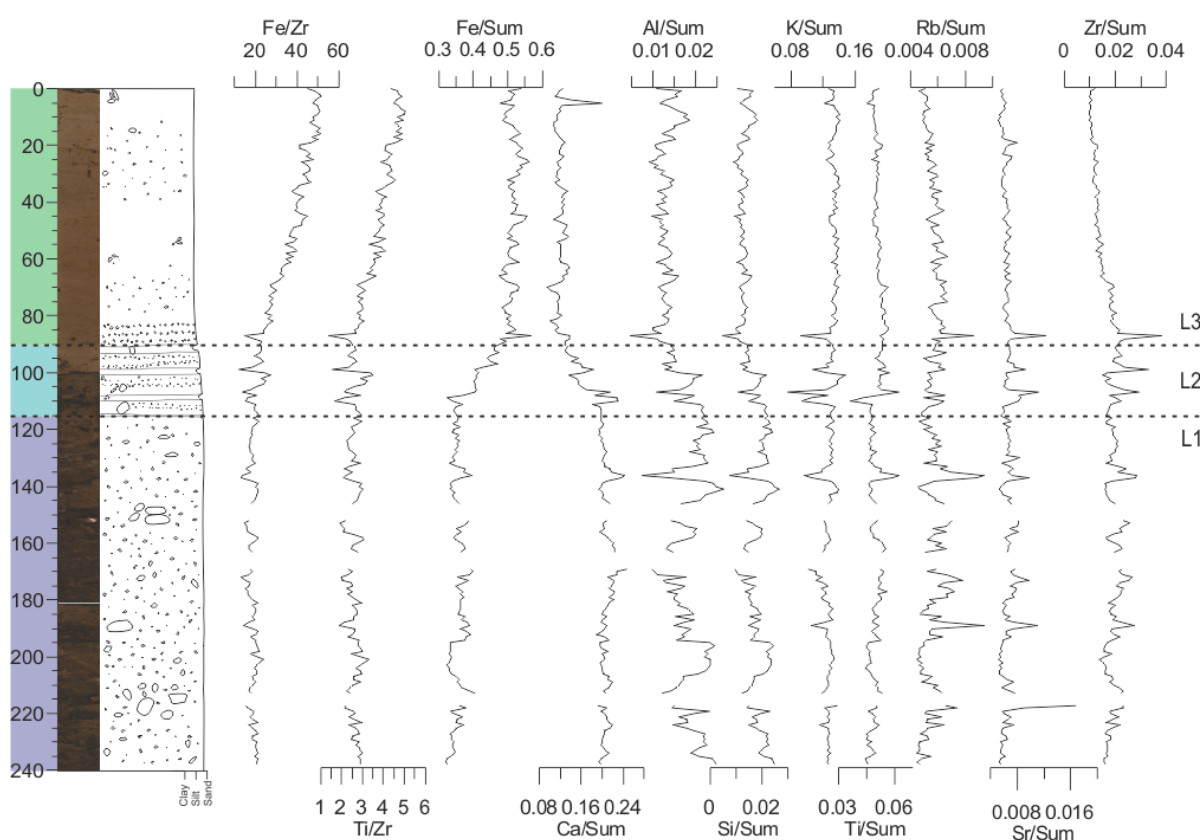


Figure 4-16. Element over sum ratios for core 1095. Note: the three gaps are due to a rough core surface rendering the results for those areas unreliable. Lithological units are indicated.

Summary and correlations

Core 1095 can be divided into two sections with a transitional area between ca. 112-80 cm. Below, it has many large clasts, is sandier, and has higher Ca. Above, Fe increases, there are fewer clasts, the sediments are siltier, and the wet bulk density is lower. There is also consistent

bioturbation in this section and visible foraminifera on the surface of the sediment core. Around 90-116 cm, there are redder layers with less sand, lower density (as in core 1091, Figure 4-14), and higher Ca and Sr compared to the other elements. Of note is the core's proximity to the mouth of Nordbreen, one of the few glaciers in the fjord that still have an active calving front, to the east and a glacier valley with a large delta to the west. These sources are likely the major contributors of sediments to the core, however this will be further analysed and discussed in section 5.3.3. Core 1095 includes all three units, with L1 from the bottom of the core to 116 cm, L2 between 116 and 90 cm, and L3 from 90 cm to the top of the core. Two radiocarbon dates from the same interval at the top of the transitional area were obtained.

4.2.4 Middle Fjord: core HH17-1100-GC-MF

The core 1100 was retrieved from near the middle of the fjord (Figure 3-1); it is 378 centimetres long.

Lithology and stratigraphy

This core is very dark grey (10YR 3/1 to GL1 3/N) from the bottom to 335 cm, at which point it changes to dark grey (7.5YR 4/1). Between 335 and 280 cm, there are also patches of dark grey (GL1 4/N). Between 280 and 278 cm, there is a well-defined layer of very dark grey (10YR 3/1). Above this, the core is dark greyish brown (10YR 4/2), transitioning gradually to brown (7.5YR4/2) by ~150 cm. By ~120 cm, the sediments are brown (7.5YR4/3), and they remain so through to the top of the core.

The bottom samples up to and including the sample at 339-340 cm have very high (>30%, <44.5%) sand content relative to the rest of the core (Figure 4-17). It drops dramatically to ~5% over the next two samples (10 cm). There are two peaks from 315 to 304 cm and 290 to 279 cm where the sand content reaches around 15% after which it remains between ~1-5% until 160 cm. Shortly after, at 144-145 cm, there is another peak, this time of ~20%. After this peak, the sand content decreases and stabilises, varying between ~4 and 10%. The silt and clay contents are the opposite: low in the bottom, before rising dramatically and staying high aside from some dips when the sand content increases. Between 279 and 160 cm, the clay content generally decreases slightly while the silt content increases similarly. Overall, the silt to clay ratio is lower in the bottom, increases from 275 cm, and then is consistently high in the upper 160 cm. Clasts are abundant and large (up to ~4 cm) in the bottom section (below 335 cm), and there is one ~3 cm clast just above this point. Additionally, between 390 and 378 cm there are

abundant sand and small-gravel-sized clasts, and the area between 150 and 115 cm has more sand- and gravel-sized clasts. Aside from those intervals, the core above 335 cm has very few scattered clasts; of note, two large clasts, one of which is ~6 cm wide, are located between 56 and 53 cm. There were two shells around 196 cm and a half shell at 154 cm. Most of the core has evidence of bioturbation except below 338 cm, around 290-275 cm, and between 265-225, and 185-115 cm (Figure 4-7).

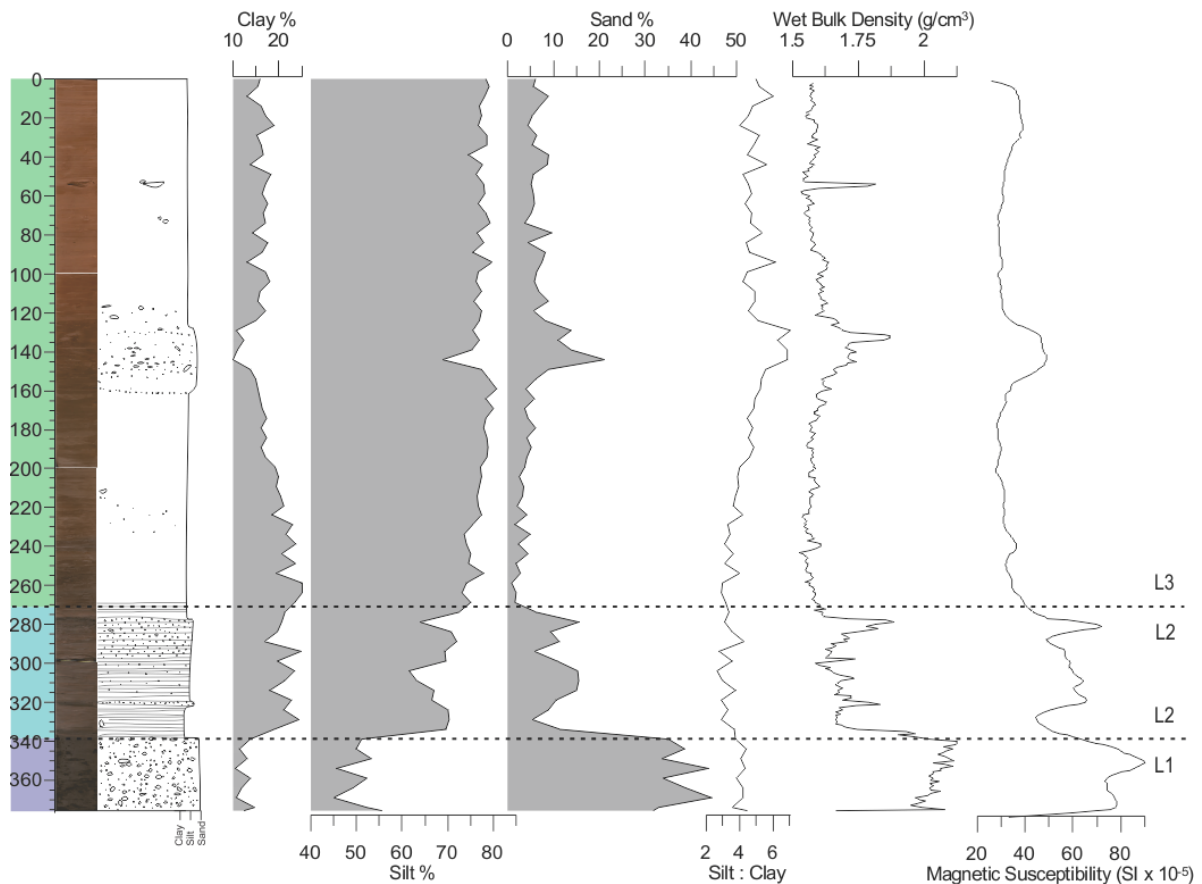


Figure 4-17. Grain size distribution and physical properties for core 1100. Lithological units are indicated.

Physical properties

The wet bulk density of the core is high below about 338 cm (Figure 4-17), above which it is lower and variable before a second high around 278-280 cm. After this, the wet bulk density stabilises. However, there are higher values from 152 to 123 cm, with a peak at 132 cm. It is again stable after this, except for a peak in bulk density from ~56 to 53 cm. The magnetic susceptibility values show a very similar trend, missing only the peak from ~56 to 53 cm (Figure 4-17).

Element geochemistry

From the bottom of the core to 338 cm, all individual elements over the sum appear to fluctuate with little overall increase or decrease (Figure 4-18). In the 5 cm above 338 cm, Fe, K, Rb, and Sr experience a rapid increase, while Al, Si, Ti, and Zr decrease. Until 271 cm, all elements behave as they did below 337 cm, fluctuating without overall increases or decreases, but around new higher or lower values. Between 271 cm and 252 cm, all elements fluctuate less. Some are stable, but Fe, Ti, and Rb increase, and Ca, Al, and Si decrease over this range.

From 252 to 238 cm, there are renewed fluctuations over thinner intervals in most element ratios. Until around 179 cm, all element ratios fluctuate but over greater intervals, not increasing or decreasing, except for Ca decreasing and Ti increasing slightly. Between 179 and 117 cm, the fluctuations in all elements strengthen again. In the upper 117 cm of the core, most elements fluctuate around stable values, through Ca increases and Ti decreases slightly overall. Between 56 and 53 cm, and 48 and 21 cm, most elements peak (Fe, Ca, Rb, Sr, Zr) or dip (Al, Si, K, Ti) slightly. The Fe/Zr and Ti/Zr ratios both are low below 338 cm, fluctuate the most between 338 cm and 270 cm. They decrease to 120 cm, before increasing to the top of the core.

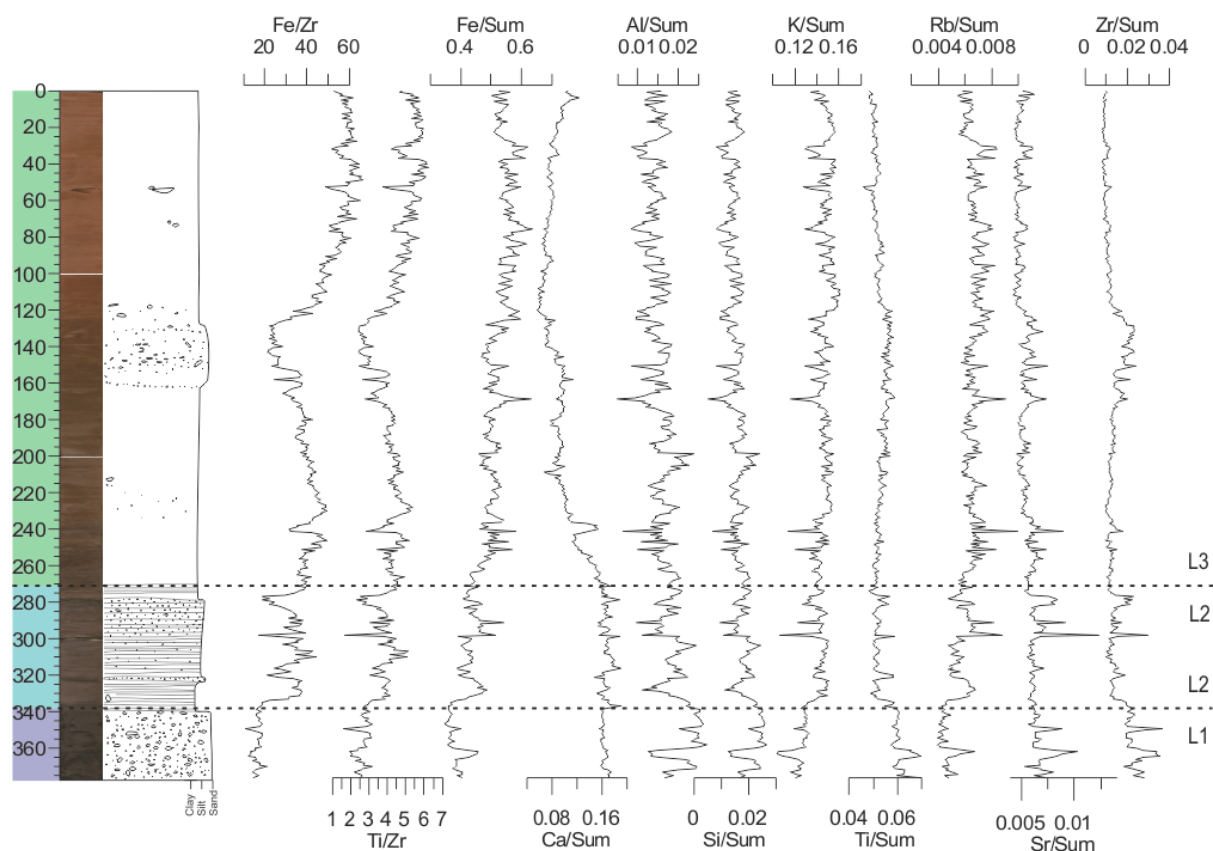


Figure 4-18. Element over sum ratios for core 1100. Lithological units are indicated.

Summary and correlations

The core 1100 can broadly be divided into three sections, the bottom of the core to 338 cm, from 338 to 271 cm, and above 271 cm to the top of the core. The very bottom has very high wet bulk density, sand content, and magnetic susceptibility. From 338 to 271 cm, these are still higher than in the rest of the core, but not as high as below. The element ratios also reflect these shifts with Fe and Rb successively increasing and Ca, Al, Si, and Ti decreasing. There is one exception to the limited number of clasts in the upper section between 150 and 115 cm, a coarse section where the sediments become sandier and clasts are more common. The majority of the core has evidence of bioturbation. Core 1100, like cores 1091 and 1100, includes all three units, with L1 from the bottom of the core to 338 cm, L2 from 338-271 cm, and L3 from 271 cm to the top of the core. The radiocarbon date from this core is from immediately below the coarser interval in the upper section.

4.2.5 Inner Fjord: core HH17-1103-GC-MF

The 215-centimetre-long core 1103 is the innermost core and was recovered from just south of where Austfjorden joins Wijdefjorden (Figure 3-1).

Lithology and stratigraphy

The colour of the core is dark grey (7.5YR 4/1) at the very bottom, but the rest of the core is more uniform in colour, though it does change slightly up-core (Figure 4-7). The transition from brown (7.5YR 4/3) to dark reddish grey (5YR 4/2) occurs almost imperceptibly around 75 cm where it was difficult to decide between the two colour codes.

The sand content of the core (Figure 4-19) is stable (~3-7%) except for between 195 and 184 cm, where it rises to ~13-15%. At those depths, the silt content is low (~71-72%), though it is stable (~75-78%) for the rest of the core as well. The clay content is also stable (~16-20%) throughout the core except between 205 and 184 cm where it makes up only ~14-15%. All three fluctuate more in the upper 65 cm of the core. There are a few clasts in the bottom 185 cm with sandy layers between 209 and 206, and 199 and 188 cm. Above this, there are few scattered clasts from 174-10 cm, with a higher number of clasts between 113 and 92 cm.

Bioturbation occurs throughout most of the core (Figure 4-7). There is no bioturbation between 192 and 142, and between 114 and 92 cm. Bioturbation is most intense in the upper part of the

core, between around 72 and 20 cm. There were shell fragments visible at 188 and 89 cm, and foraminifera or very small shell fragments from 210 cm through to 180 cm.

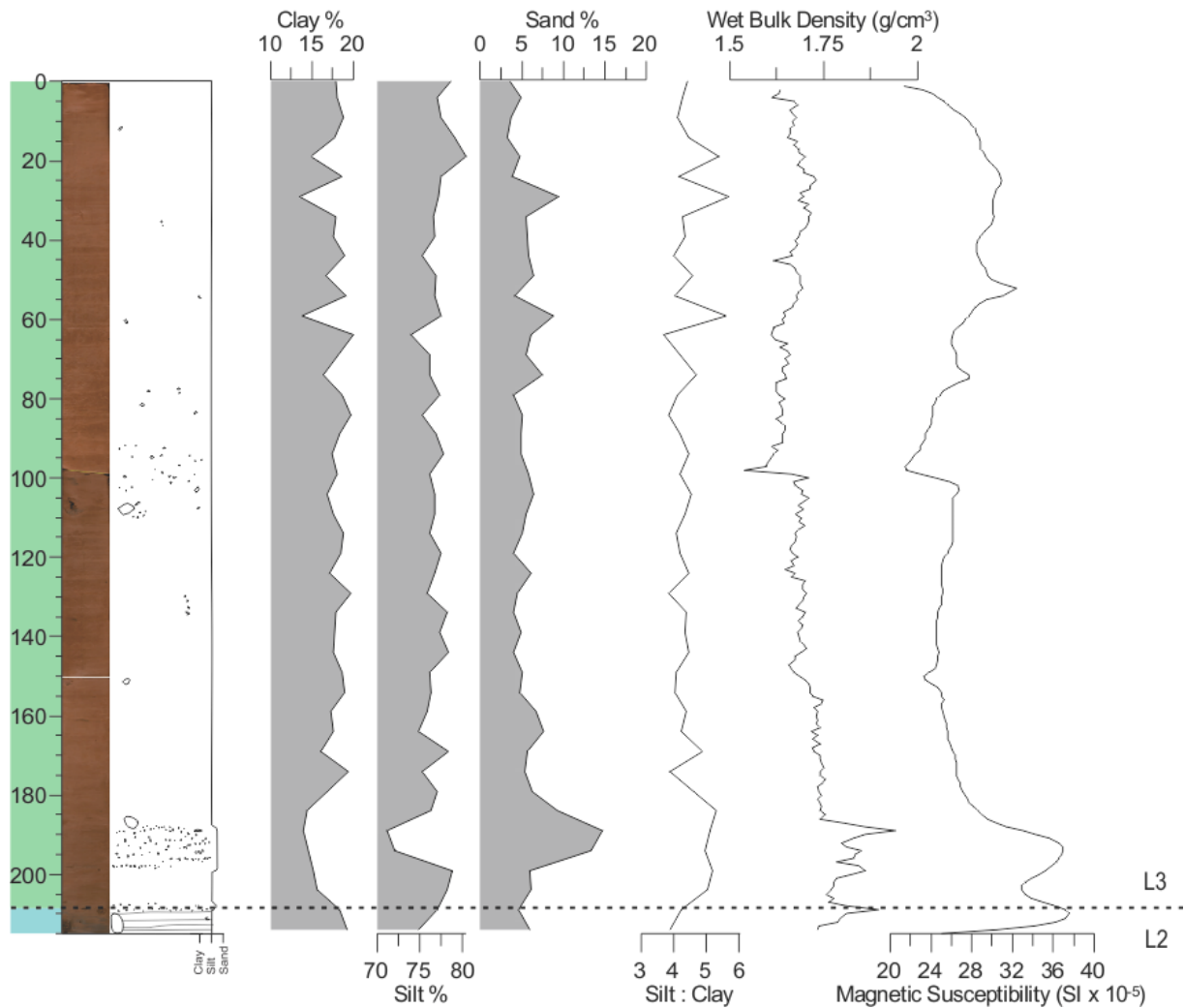


Figure 4-19. Grain size distribution and physical properties for core 1103. Lithological units are indicated.

Physical properties

The wet bulk density is highest at the bottom of the core (Figure 4-19), and though it fluctuates, it is high ($1.75\text{-}1.95\text{ g/cm}^3$) until 187 cm. From there to 100 cm, it varies little while steadily decreasing over the interval, aside from a slight dip between 151 and 145 cm, corresponding to a core section change and the 5 centimetres of material at the bottom of the second core section. There is a decrease of $\sim 0.13\text{ g/cm}^3$ between the wet bulk density values of the two sections of core that meet at 100 cm, but the values below are consistently $\sim 0.08\text{ g/cm}^3$ higher than above. From 100 cm to around 30 cm, the wet bulk density increases slightly, before decreasing to the top of the core. The magnetic susceptibility (Figure 4-19) follows the same

pattern, except the slight increase from 100 cm to around 30 cm begins earlier, at around 140 cm. Additionally, the dip at the lower core boundary (150 cm) does not persist as it does in the wet bulk density. The magnetic susceptibility also decreases at the section boundary at 100 cm and then remains lower above it.

Element geochemistry

In the bottom 30 cm of the core (Figure 4-20), Fe, K, and Rb increase, while Ca decreases relative to the sum, at first quickly then more slowly after ~7 cm. Ti, Sr, and Zr are stable until ~198 cm before increasing and then decreasing over the next ~13 cm. Above 185 cm, Ca fluctuates slightly but overall increases gradually to the top of the core, with only a small decrease between 130 and 127 cm and a larger increase between 10 and 5 cm. The Fe ratio also increases above 185 cm, but from around 90 cm to the top of the core, it decreases. Al and Si fluctuate perfectly in tandem while decreasing slightly throughout the core. Ti also decreases slightly through to the top of the core. The remaining elements (Rb, Sr, and Zr) remain relatively stable aside from a small peak from 151-149 cm and a small rise and fall from 105-80 cm. The Fe/Zr and Ti/Zr ratios are both low in the bottom of the core, with a peak around 205 cm, before increasing to 180 cm, and thereafter remain stable, except for a dip at 112 cm.

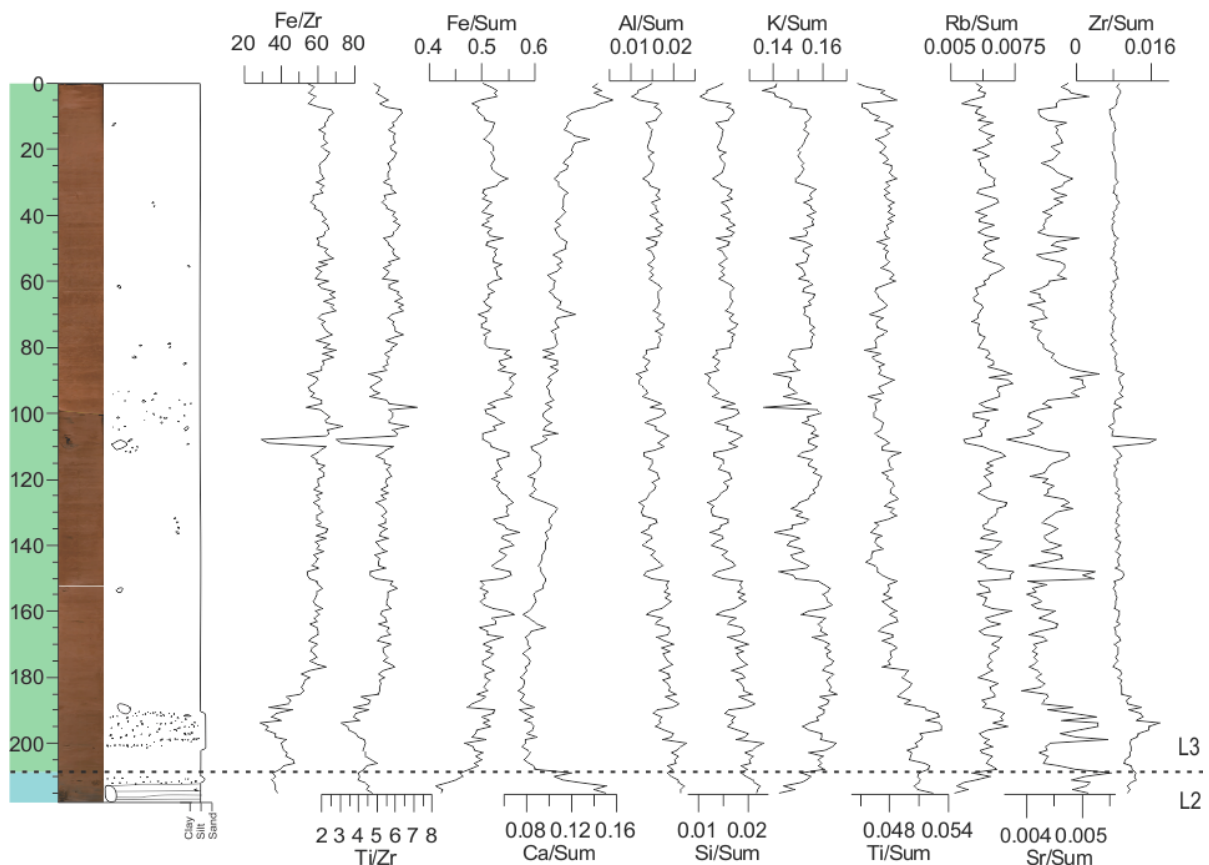


Figure 4-20. Element over sum ratios for core 1103. Lithological units are indicated.

Summary and correlations

This core is generally uniform except for the bottommost 25 cm, where there are two coarse intervals separated by muds with some grey wisps contrasting with the nearly uniform brown of the rest of the core. These intervals have higher sand content, wet bulk density, and magnetic susceptibility, as well as higher Ca and lower Fe and K than the rest of the core. Most element ratios do not change considerably throughout the rest of the core, though Ca does increase steadily after the initial decrease. Core 1103 contains just two units, with L2 from the bottom of the core to 208 cm, where the grey wisps end, and L3 from 208 cm to the top of the core. The radiocarbon date is from the bottom of the core, at the top of the lower coarse layer.

4.2.6 Chronology

The results of the radiocarbon dating and their calibrated ages are presented in Table 4-2 below and are indicated in Figure 4-7. Additionally, dates acquired by Seung-Il Nam, who had sampled dating material from the same cores prior, are included in Table 4-2 and Figure 4-7. All calibrations were performed using Calib 7.1 (Stuiver et al., 2019) with the marine13.14c data set (Reimer et al., 2013) and a delta R of 105.0 ± 24.0 after Mangerud et al. (2006). The dates from the two different foraminifera species separated from the same sediment sample give ages that agree within the error margin.

Table 4-2. Radiocarbon dating and calibration results

Core	Depth (cm)	Species	C ¹⁴ age BP	Cal. yr BP (1σ)	Cal. yr BP (mean)
1085	221.5	<i>Yoldiella lenticula</i>	10 829 ± 39	12 251-12 014	12 144
1085	326	Unknown	12 696 ± 40	14 147-14 005	14 077
1085	365	Mollusc indet.	>43 500 ¹	-	-
1095	82-83	<i>Nonionellina labradorica</i>	4123 ± 68	4137-3927	4035
1095	82-83	<i>Cibicidoides lobatulus</i>	4093 ± 66	4086-3888	3996
1100	120	Mollusc indet.	2960 ± 30 ¹	2705-2569	2627
1100	150	Mollusc indet.	9080 ± 30 ¹	9673-9548	9626
1100	154.5	<i>Macoma calcarea</i>	9391 ± 38	10 198-10 079	10 130
1100	225	Mollusc indet.	10 070 ± 30 ¹	11 044-10 864	10 948
1103	50	Mollusc indet.	1230 ± 30 ¹	709-645	679
1103	165	Mollusc indet.	2840 ± 30 ¹	2494-2350	2444
1103	208.5	<i>Nonionellina labradorica</i>	6821 ± 50	7302-7183	7248
1103	210	Mollusc indet.	6250 ± 30 ¹	6635-6525	6579

¹Dates from S.-I. Nam, pers. comm.

4.2.7 Sedimentation rates

The dates, including those from S.-I. Nam, pers. comm. are used to calculate the sedimentation rate for each core. However, with the limited dates, precise sedimentation rates are impossible to determine. Here, estimated linear sedimentation rates are presented (Table 4-3, Figure 4-21), assuming a constant sedimentation rate between dated intervals and that the top of each core represents the seafloor the year the cores were retrieved (2017) giving them an age of -67 cal. yr BP. This assumes the modern seabed was preserved during coring, but since coring can result in the loss of some of the surficial sediments, all sedimentation rates to the top of the core should be considered minimum estimates.

Table 4-3. Linear interpolated sedimentation rates for all cores

Core	Depth (cm)	Lithological unit	Cal. yr BP mean	Sedimentation rate (cm/ka)	Age range (cal. yr BP)
1085	221.5	L3	12 144	18.1	12 144-top
1085	326	L2	14 077	54.1	14 077-12 144
1085	365	L2	not included in calculations		
1095	82-83	L3	4035	20.2	4015-top
1095	82-83	L3	3996		
1100	120	L3	2627	44.5	2627-top
1100	150	L3	9626	4.3	9262-2627
1100	154.5	L3	10 130	8.9	10 130-9626
1100	225	L3	10 948	86.2	10 948-10 130
1103	50	L3	679	67.0	679-top
1103	165	L3	2444	65.2	2444-679
1103	208.5	L2	7248	9.1 ¹	7248-2444 ¹
1103	210	L2	6579	10.9 ¹	6579-2444 ¹

¹ Due to the age reversal between these two samples, both sedimentation rates were calculated to the unaffected sample above, from 165 cm.

The dating results from 1085 include two dates from 221.5 and 326 cm. Above 221.5 cm, the sediments are mostly consistent, however the unit boundary marks a change. Assuming consistent sedimentation in both areas, the sedimentation rate is 18.2 cm/ka above 221.5 cm and 54.1 cm/ka between 326 and 221.5 cm. If the sedimentation rate from the transitional area applies below as well, the bottom of the core would have an age of around 16.6 cal. ka BP. The

sample from 365 cm was $>43\,500$ ^{14}C yrs BP so it was not used to calculate sedimentation rates.

From one sediment sample in core 1095, two species of foraminifera were dated separately. Both are infaunal and live in the upper 5 cm of the sediments (Wollenburg & Mackensen, 1998). The ages for both foraminifera samples from the same depth are very similar, each within the standard deviation of the other. To calculate the linear sedimentation rate, I have used the average of the two values (4015 cal. yr BP), which gives a rate of 20.2 cm/ka above 82.5 cm. Since the samples tested are from a transition from clast-rich to clast-poor material, as well as a change in units, this rate likely does not resemble the sedimentation rate below the transition.

Core 1100 has a linear sedimentation rate of 44.5 cm/ka above the sample from 120 cm, 4.3 cm/ka from 120-150 cm, 8.9 cm/ka from 150-154.5 cm, and 86.2 cm/ka from 154.5 to 225 cm. Assuming this rate was constant for the like sediments from below this point to 277 cm, the age of the bottommost sediments of L3 is $\sim 11\,480$ cal. yr BP.

The dating samples from core 1103 show that sedimentation rates were 67.0 cm/ka from 50 cm to the top of the core and 65.2 from 50 to 165 cm. The dates from 208-209 cm and 210 cm show an age reversal. Calculating the linear sedimentation rate between each of these dates and the date from 165 cm gives values of 9.1 cm/ka or 10.9 cm/ka respectively. This will be discussed further in the discussion (section 5.4).

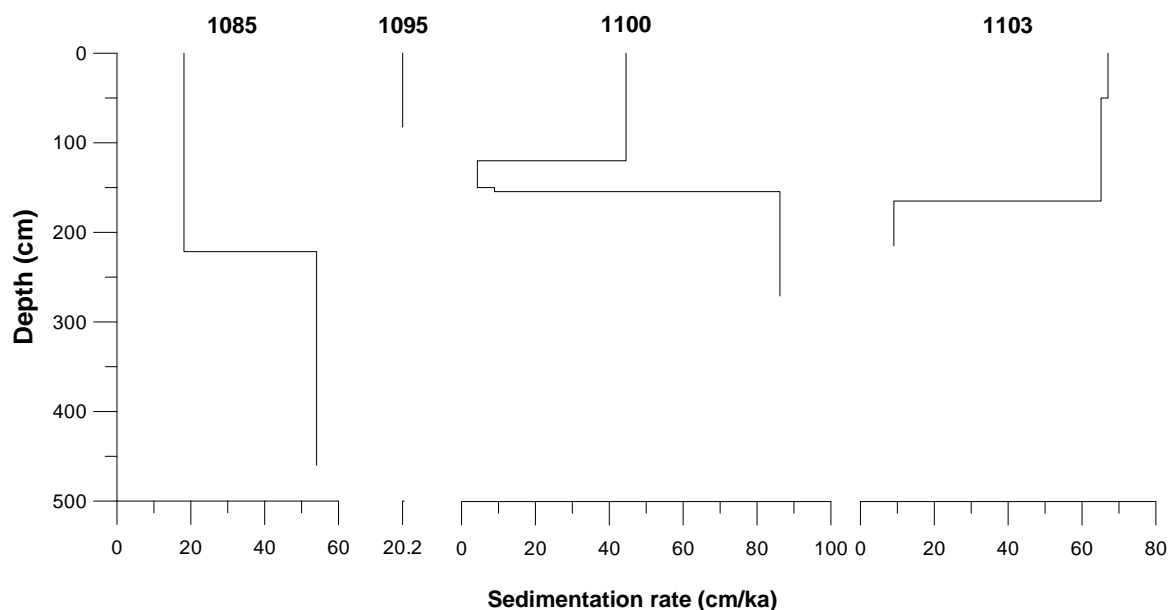


Figure 4-21. Linear sedimentation rates in each dated core, with extrapolation down to unit boundaries when possible (as explained in text).

5 Discussion

In this chapter, I first discuss the acoustic data, interpreting the units and large-scale trends in the distribution of the units. This is followed by a correlation of the acoustic data and the sediment cores, with interpretations of the local sedimentary environments.

Following discussion of the acoustic data, the sedimentary results are discussed, beginning with the sedimentation processes. I discuss the sedimentary processes that are dominant in the fjord and on the shelf, as well as the likely provenance of the sediments. I then discuss the sedimentation rates and compare the different rates within and between cores and to other cores from similar environments in other Svalbard fjords.

The culmination of the discussion is a summary of the overarching processes controlling the sedimentation from the shelf to the inner fjord, and the way these change after the deglaciation in the Late Weichselian, through the Holocene, to the present.

5.1 Acoustic data

The three units identified in the chirp data (e.g., Figure 4-2) are irregularly distributed; this and other characteristics, such as their thickness, can be used to gain a broad picture of the processes operating within the fjord at the time of deposition.

5.1.1 Units

The acoustic basement is likely bedrock in most areas due to the scouring that occurs as ice streams remove pre-glacial material (Batchelor et al., 2011; Forwick and Vorren, 2011; Syvitski et al., 1989). Unit 1 is interpreted to be of glaciogenic origin, e.g., a basal till, and generally overlies the acoustic basement, though in some areas (e.g., Figure 5-6) it appears that Unit 1 is part of the acoustic basement. Areas with large mounds or spike are interpreted to be recessional moraines forming at the glacier front during stillstands and/or small re-advances during the deglaciation (Baeten et al., 2010; Forwick et al., 2011; Ottesen et al., 2005; Ottesen and Dowdeswell, 2006).

Overlying Unit 1 in some places is Unit 2, interpreted to be glacier-proximal deposits. Acoustic stratification is likely due to the frequent lithological changes that occur in such environments (Forwick and Vorren, 2011; Kempf et al., 2013; Syvitski et al., 1989). The general homogeneity and occasional internal stratification of Unit 3 is interpreted to reflect relatively stable glaciomarine or glacier-distal deposits. The internal reflections, present within U2 and

U3, are likely due to layers with more clasts deposited during intervals of increased ice-rafting (Forwick and Vorren, 2011; Kempf et al., 2013).

5.1.2 Distribution

In general, U1 is well developed beyond the fjord mouth, in the outer parts of the fjord, on the plateau or outer sill, as well as immediately south of the plateau. U2 and U3 occur typically as a drape with varying thickness; they are thin in shallower parts and over sills and thicker in depressions (Figure 5-1).

In the north of the chirp profile (Figure 5-1, A), U2 and U3 are thick (~12 ms TWT) with internal reflections while U1 is absent. The thicker glaciomarine sediment sequence is indicative of high sedimentation rates, and the lack of U1 is most likely simply due to the limited penetration of the chirp echosounder. Moving south, U1 appears near to the surface where the bathymetry shallows as a very chaotic unit (Figure 5-1, B). This likely is indicative of limited glaciomarine sedimentation above the till, perhaps due to the shallower bathymetry. In this area, it is also possible that winnowing has removed much of the finer clays and silts, leaving only coarser sediments, and that U1 represents these coarser sediments in addition to the glacial till. Winnowing of current sediments has been identified from the shelf north of core 1091 to within the fjord near Nordbreen (Görlich, 1988) (for location of Nordbreen see figure Figure 2-6) and it is possible that this process has been active for the majority of the Holocene as it has been on shallow banks in northern Norway (Vorren et al., 1984).

Near the fjord mouth and core 1091, U2 and possibly U3 are present but thin and hard to differentiate. In areas where there are depressions in U1, U2 and U3 are thicker, filling them in, allowing for a relatively flat seafloor. The ice likely retreated more quickly on the shelf and in the outer part of the fjord (Ottesen et al., 2007), which, as well as the ongoing winnowing observed in the surface sediments, could explain the thinness of U2 and U3 and the more chaotic or coarse U3.

In the outer fjord, near core 1095, when U2 is thinner, U3 is thicker and has stronger internal reflections, and vice versa, likely due to alternating periods of slower and faster glacial retreat. Over the plateau, or outer sill, sediment cover is typically thin except in some areas with thicker, chaotic U2. Those areas could correspond to grounding-zone wedges, interpreted in this part of Wijdefjorden by Forwick et al. (2011), and are similar to those identified in other Svalbard fjords (Dowdeswell et al., 2016; Ottesen et al., 2007).

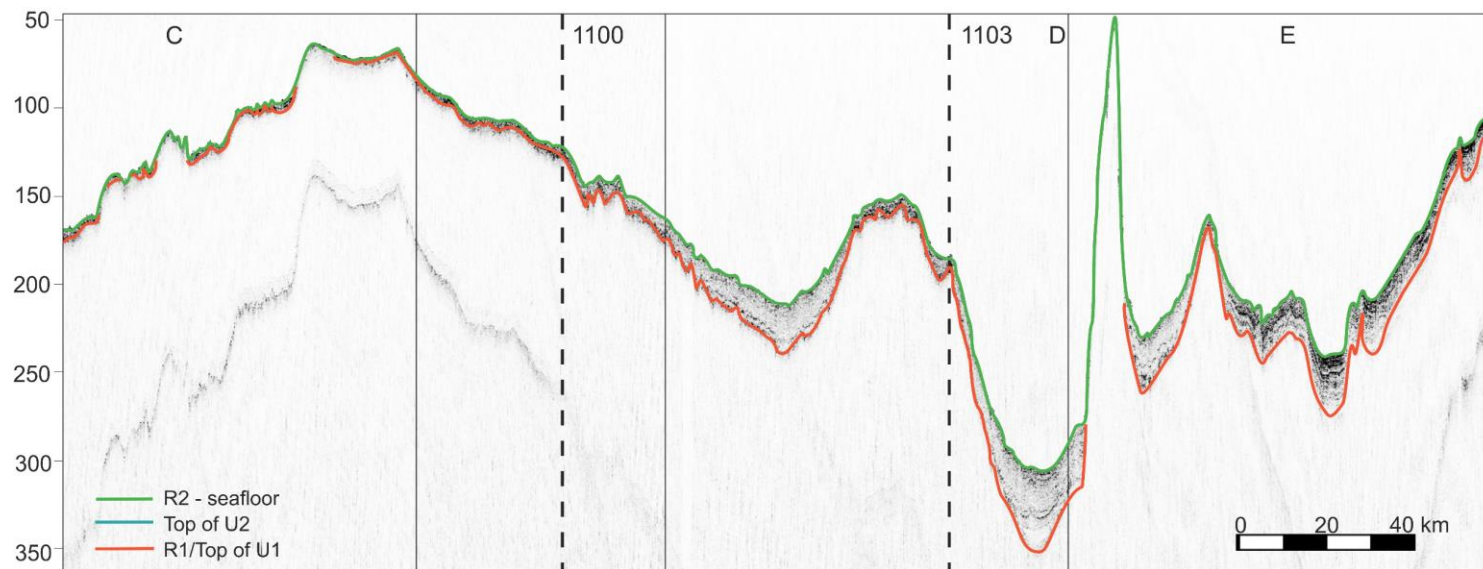
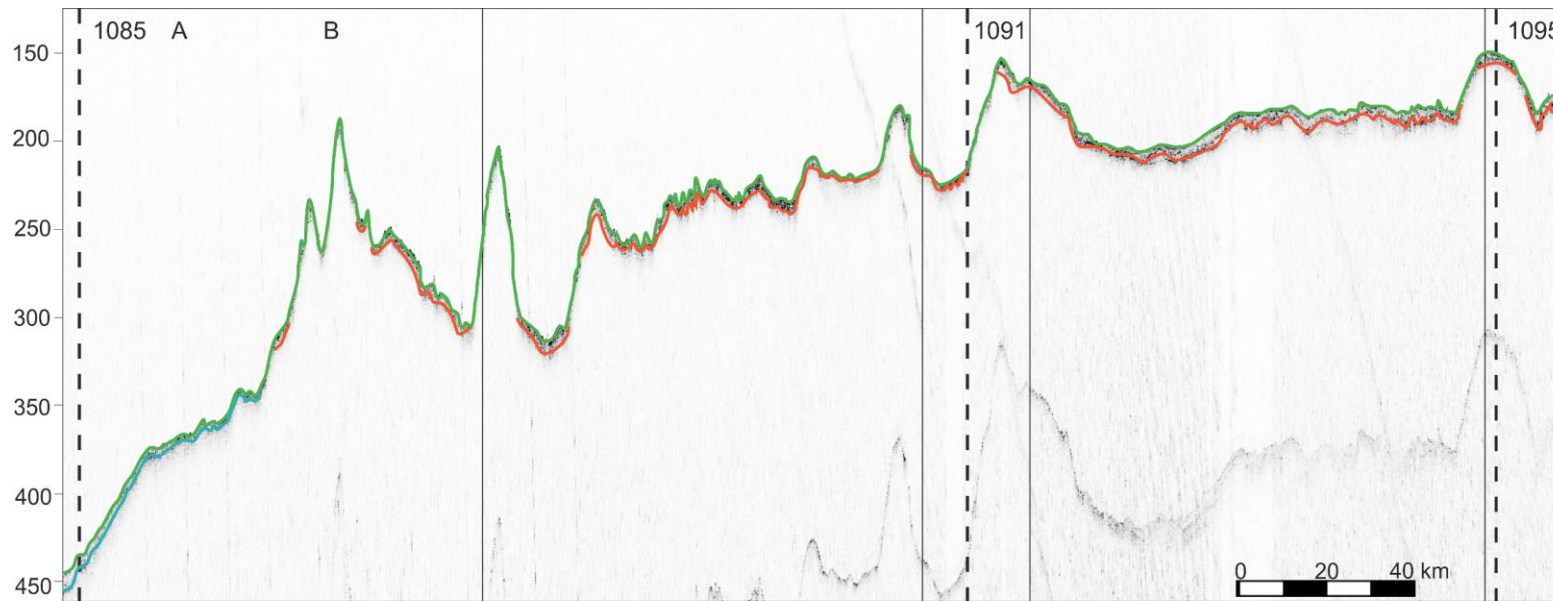


Figure 5-1. Interpreted composite chirp profile, with the seafloor (R2, green) and the top of the till, U3 or bedrock (R1, red). In most places, the seafloor and till are too close together to interpret the top of U2, indicated, when possible, in blue. Cores are indicated (dashed line). Letters A-E indicate areas mentioned in the text.

When the top of U1 is rough with U2 filling in the depressions between peaks (Figure 5-1, C), and U3 draping the units below, it is interpreted as potentially being a series of moraines. Moraines have been identified here by Forwick et al. (2011), and they do resemble other moraines in chirp profiles (e.g., Plassen et al., 2004; Streuff et al., 2018), however, without a 3-D view, it is not possible to make a determination.

The units thin and become slightly more chaotic, or less transparent, in the inner fjord, south of core 1100. This is likely due to the reduced sedimentation rates associated with bathymetric highs. Conversely, in the basins in inner Wijdefjorden (Figure 5-1, D, E), the sediments are very thick, at up to 39 ms TWT above the U1 reflector. In the basins, there are many internal reflectors, and the uppermost ~10 ms TWT are less transparent. These likely represent thick sequences of glaciomarine sediments, with frequent intervals with higher clasts (e.g., Batchelor et al., 2011; Forwick and Vorren, 2011; Plassen et al., 2004; Svendsen et al., 1992) accumulating in the basins above the glacial till. The decreased transparency in the upper part of the profile (Figure 5-1, E) suggests that coarser sediments are more common in the relatively recent sediments.

5.2 Correlation of acoustic data and sediment cores

The correlation of the acoustic data and the sediment cores requires projecting the core locations and thicknesses to the chirp profile. The location is based on GPS measurements taken at the time of coring; however, the GPS unit is not located directly at the coring unit, hence introducing some error. Additionally, the corer may not reach the sediments directly below the coring unit due to currents deflecting the wire and potential drift of the ship. In some cases, the projected core location has been moved slightly (<15 m) from the direct GPS location to reflect better correlation between the core and the acoustic profile at that location. Estimating the core thickness in TWT also introduces sources of error. For all cores, the P-wave amplitudes were often 0, rendering the P-wave velocity and therefore the acoustic impedance (AI) values unreliable. As such, a uniform velocity of 1600 m/s (Elverhøi et al., 1995; Forwick and Vorren, 2011; Plassen et al., 2004) is used in correlations between core thickness and TWT in the chirp profiles. Additionally, cores can undergo shortening during the coring process, artificially raising some sediments or units in the cores (Löwemark et al., 2006). Acoustic profiles rely on changes in the sediment properties, as it is differences in the sediments, specifically the AI, that lead to reflections. Since the AI is unreliable, clast content and sediment density are used

instead. Despite these limitations, features in the cores are often easily correlated to features in the chirp profiles.

5.2.1 Core 1085

The core 1085 was retrieved from the Wijdefjorden cross-shelf trough as it meets the Hinlopen Trough (Figure 3-1). The core contains two units, the stratified muds of L2, including one rocky layer, and the massive muds of L3. This core contains little IRD. The chirp profile at this location shows a relatively thick (~6.3 ms TWT) U3 above U2 (Figure 5-2). The total sediment thickness here is at least 10.9 ms TWT thick, or ~8.72 m. Within U3, there are three reflections interpreted to be internal reflections starting at 4.1 ms TWT (Figure 5-2). They correspond well to changes between the redder (less dense) and greyer (more dense) sediments in the core, as well as the rocky layer, however not every colour change in the core is visible in the chirp profile. Because this area is relatively flat and the reflections are parallel, it is likely that small differences in the coring location would have little effect on the appearance and properties of the core, and that those correlations are sound.

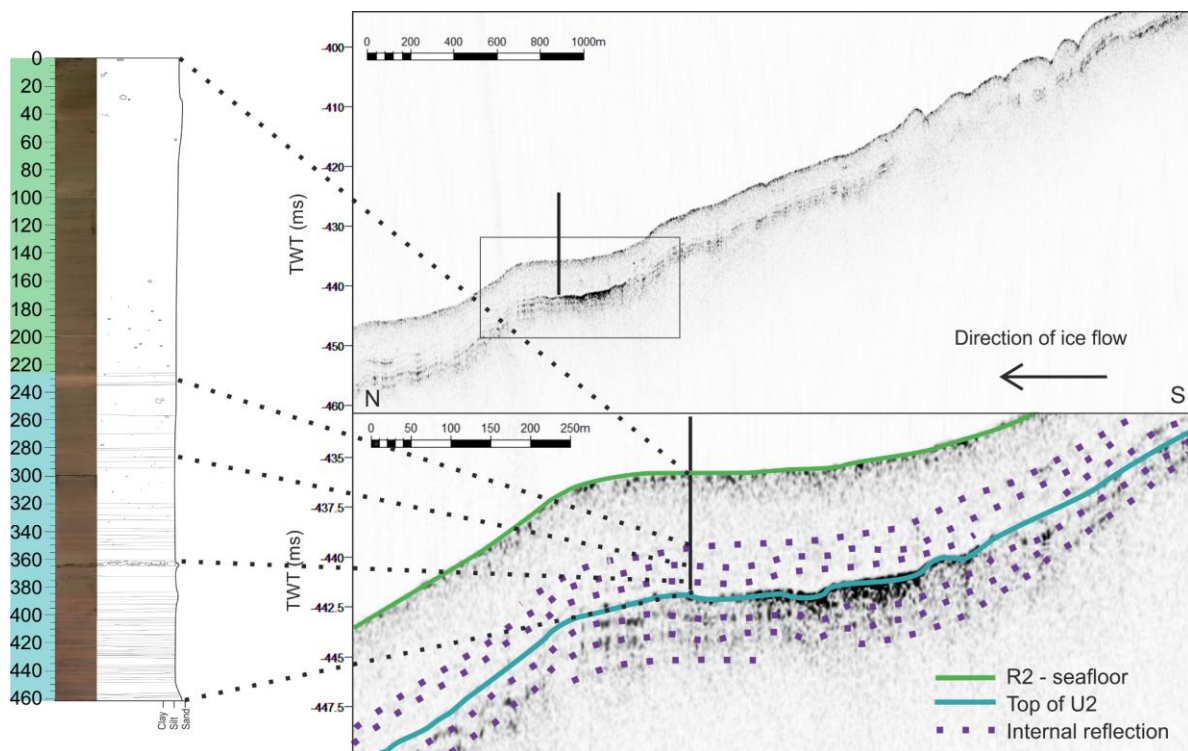


Figure 5-2. Chirp profile with interpreted section showing the internal reflections, the acoustic units present, and the projected location of core 1085, correlated with the lithological log.

The change in the core from L2 to L3 is gradual, without any major changes in core properties (e.g., clast abundance or density) that could be reflected in the chirp profile, it is therefore

reasonable that this transition is not clear in the chirp profile. The core nears but does not reach the stronger reflection at the top of U2, which, along with the internal reflections below, are interpreted to be layers with more coarse material, deposited in a more proximal glaciomarine environment (Forwick and Vorren, 2011; Svendsen et al., 1992; Syvitski et al., 1989). In this location, U3 contains lithological units L3 and L2, and the L2 sediments likely continue throughout U2 (Figure 5-2).

5.2.2 Core 1091

Core 1091, from just outside the mouth of Wijdefjorden, contains all three lithological units despite being only 86 cm long. In the chirp profile, U1, U2, and U3 are present, but the sequence of seismic units is thin: the top of U1 is at most 1.5 ms TWT (~1.2 m) from the seafloor reflector (Figure 5-3). U2 is rough, very close to the seafloor, and more transparent than U1 and U3. There is a weak internal reflection where it fills the lows in U1 and becomes thicker, again, likely due to coarser layers. (Note: this internal reflection was too discontinuous to indicate in the chirp profile.) The top of U1 is very rough, often nearing the seafloor. The high clast content of L1 and L3 is reflected in the chaotic nature of U1 and U3. In this area, U1 corresponds well to L1, U2 to L2, and U3 to L3.

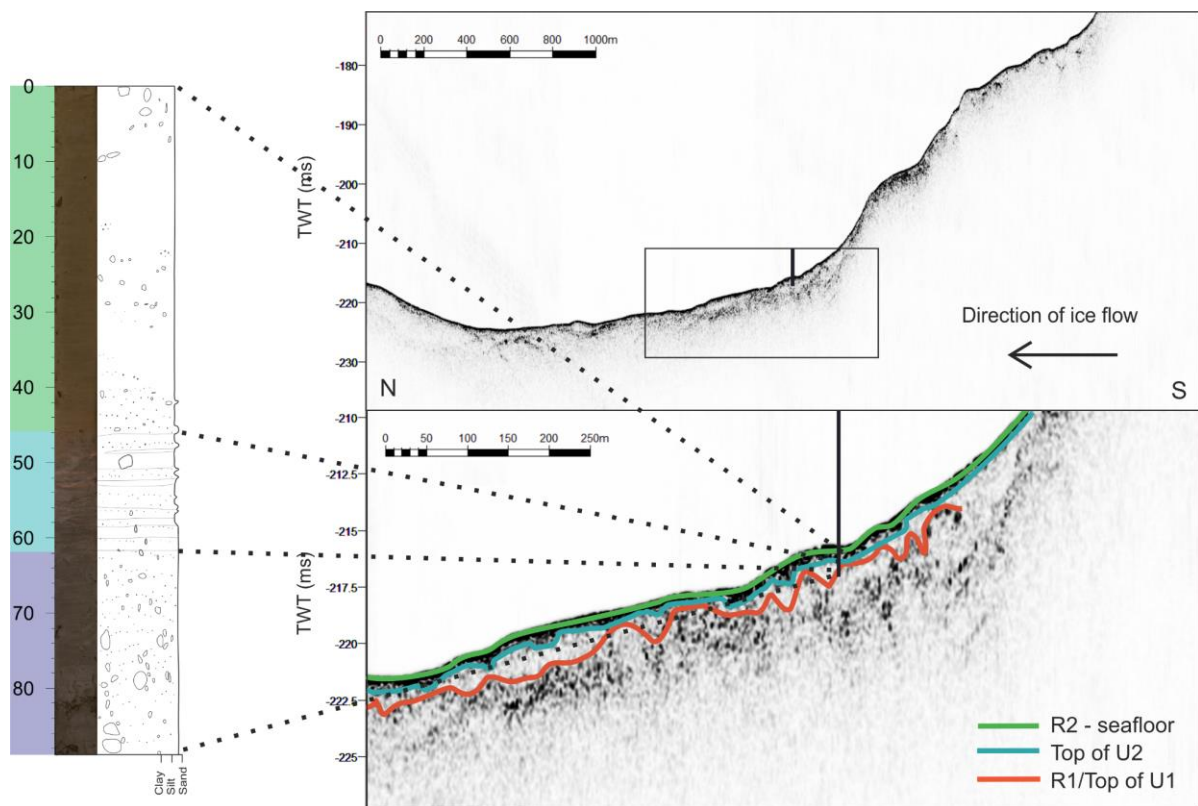


Figure 5-3. Chirp profile with interpreted section showing the projected location of core 1091 in relation to the three acoustic units, correlated with the lithological log.

5.2.3 Core 1095

This core, 1095, was taken on a small high in the bathymetry in the outer fjord (Figure 5-1, Figure 5-4). It, like 1091, also contains all three lithological units, though they are thicker in this core. As in the area around core 1091, Units U1, U2, and U3 are present in the acoustic data. U1 is hummocky here, with U2 and U3 being thicker in the depressions. The density of the core is relatively uniform and high in units L1 and L2, decreasing gradually in the top of L2 to L3. The U1 reflection here is weak, which could be due to the uniform density and similar clast content of L1 and L2. In unit L2, the laminations are thin and more clasts-rich than in the other cores, likely leading to the less transparent nature of U2 in this area. Additionally, the change in density between L2 and L3 change roughly corresponds to the top of U2. In this area, the acoustic units correspond well to the lithological units.

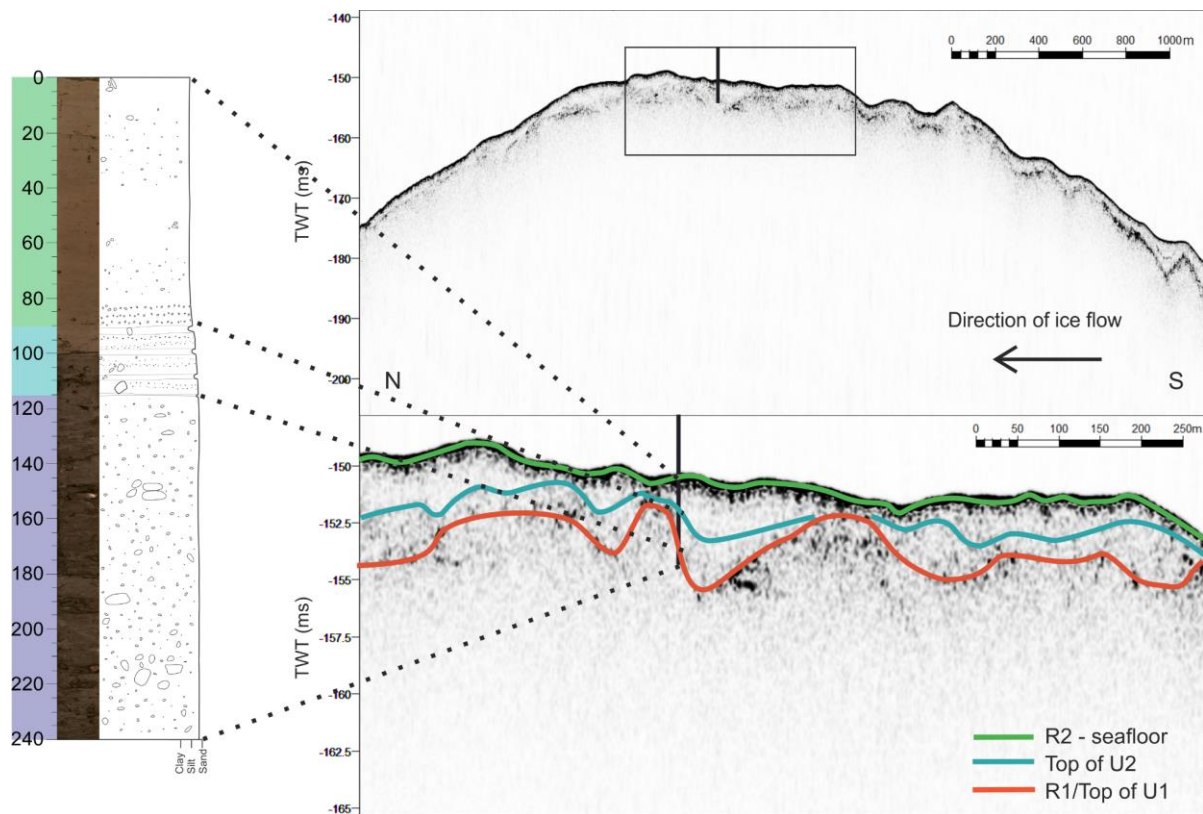


Figure 5-4. Chirp profile with interpreted section showing the three interpreted acoustic units and the projected location of core 1095, correlated with the lithological log.

5.2.4 Core 1100

Core 1100 was taken from a depression between two small rises (Figure 5-5), possibly moraines (Forwick et al., 2011), on the slope to the south of the northern sill near the middle of the fjord (Figure 5-1). To the north and south of the projected core location, U1 rises and the

overlying sediments are thinner. However, it is difficult to interpret where the boundary between U2 and U3 is in the chirp profile. In the core, there is little difference in density between L2 and L3, so they are likely to appear similar in the seismic section. The internal reflections are again likely to correspond to coarser layers in the sediments. The density of the sediments does decrease just above a coarse layer within L2, and at the boundary between L1 (clast-rich) and L2 (clast-poor). These changes are not easily correlated to the acoustic profile (Figure 5-5). However, the sediments possibly experienced some shortening during coring, and a small decrease in the assumed sediment velocity could lower the bottom of the projected core as well. Given that the appearance of the profile seems to match the core, it is likely that the acoustic units correlate well to the respective lithological units.

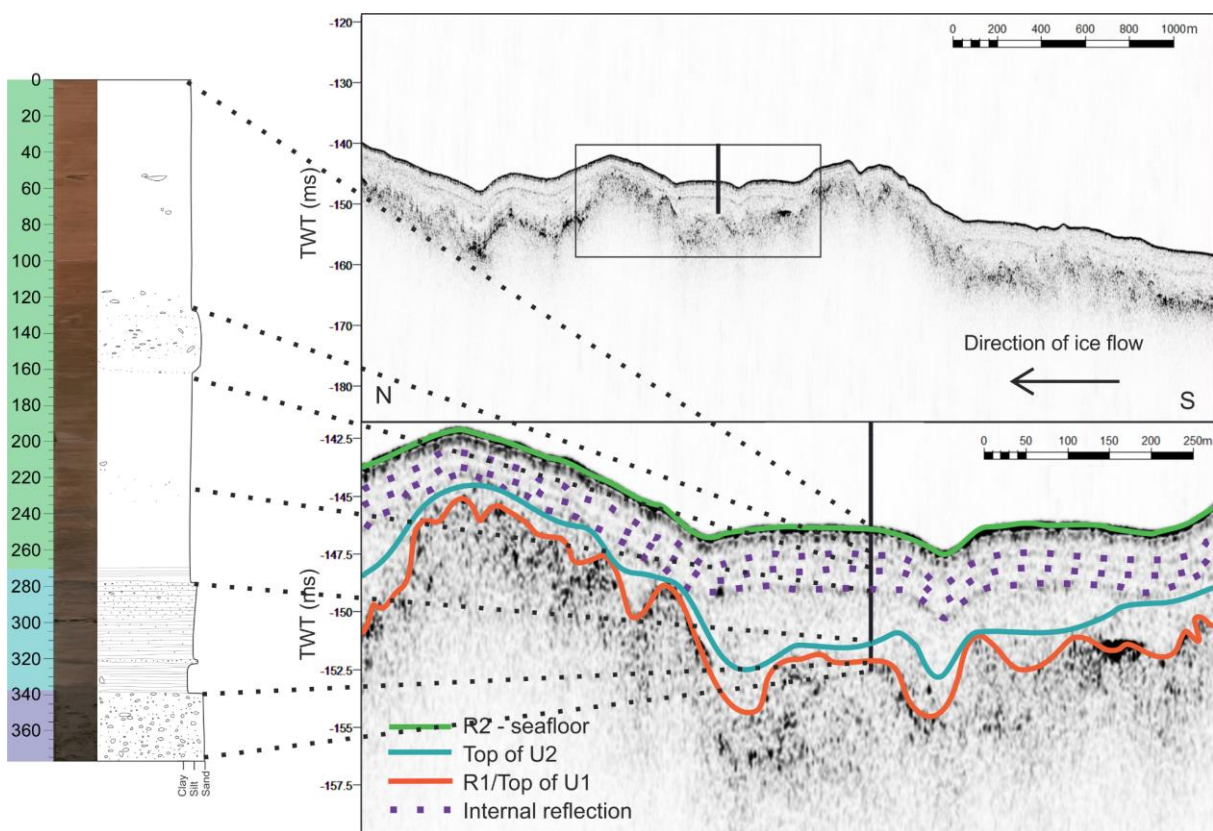


Figure 5-5. Chirp profile with interpreted section showing the units and internal reflections and the projected location of core 1100, correlated with the lithological log.

5.2.5 Core 1103

The innermost core (1103) was taken on a small bump on a larger rise (Figure 5-6, Figure 5-1). It is almost exclusively L3, with only a few centimetres of L2 at the bottom. The bottom ~20 cm of L3 are the coarsest and sandiest of the core, though a few large clasts are present in the L2 muds, and there are many clasts scattered throughout the rest of the L3 unit. The clasts do not

correspond to the internal reflection, but the diameter of the core is very small in relation to the vertical and horizontal resolution, and the beam width for the chirp profile; additionally IRD are not distributed evenly. It is possible other cores taken from the same location would have a higher number of clasts in the upper L3 and that the internal reflection is indeed the result of a coarser layer here, as in the other cores and profiles. In the chirp profile, the projected core appears to just miss the top of U2. As explained with regards to core 1100, the projected core depth and locations are estimates, and small changes in core shortening during coring, the core location, or assumed sediment velocity can affect this. It is likely that U2 does correlate to L2, and U3 to L3 as in the other cores. The distribution of U2 in this section of the profile is largely in the depressions between the smaller U1 highs, but U2 is also present capping the larger U1 rises as at the projected coring location and to the north, at the far left of Figure 5-6.

In summary, the acoustic units correlate well to the lithological units in most cores and internal reflections correspond well to depths in the cores with more IRD.

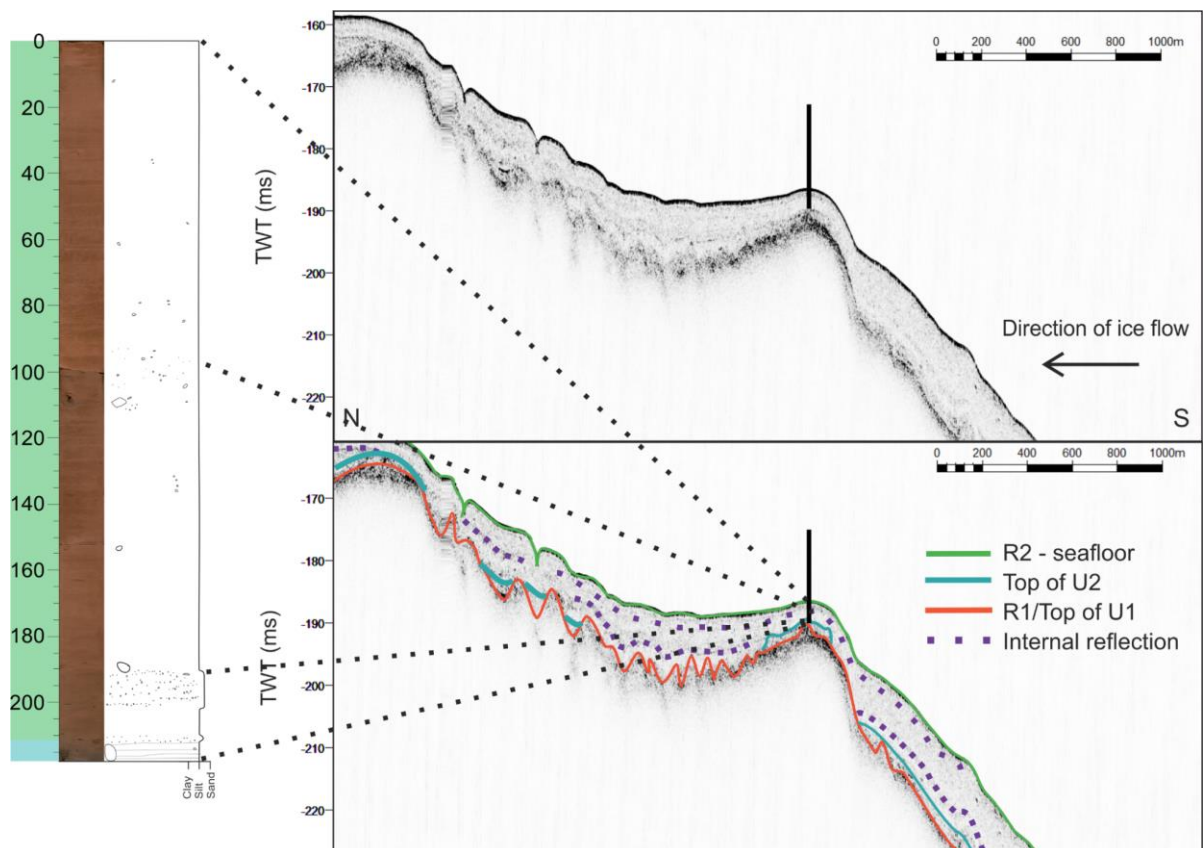


Figure 5-6. Chirp profile with interpreted section showing the projected location of core 1103, correlated with the lithological log.

5.3 Sedimentary processes and provenance

Sediments can enter and be transported within a fjord via glaciers (ice-contact processes, iceberg rafting), fluvial sources, rafting by sea ice, terrestrial mass wasting, and by deep-water currents (Hambrey, 1994; Howe et al., 2010b). The dominant sedimentation processes in a glaciated fjord vary primarily with proximity to the glacier front and other sediment sources, with the local hydrographic regime (tidal activity, internal waves, Coriolis effect, etc....) and with the morphology and depth of the fjord floor (Howe et al., 2010b; Syvitski et al., 1987). Figure 5-7 shows the main sedimentation processes and deposits in glaciated fjords. The dominant post-glacial sedimentation processes operating in Wijdefjorden, based on the five sediment cores analysed, are suspension settling and IRD; these will be discussed further below, followed by a discussion of sediment provenance.

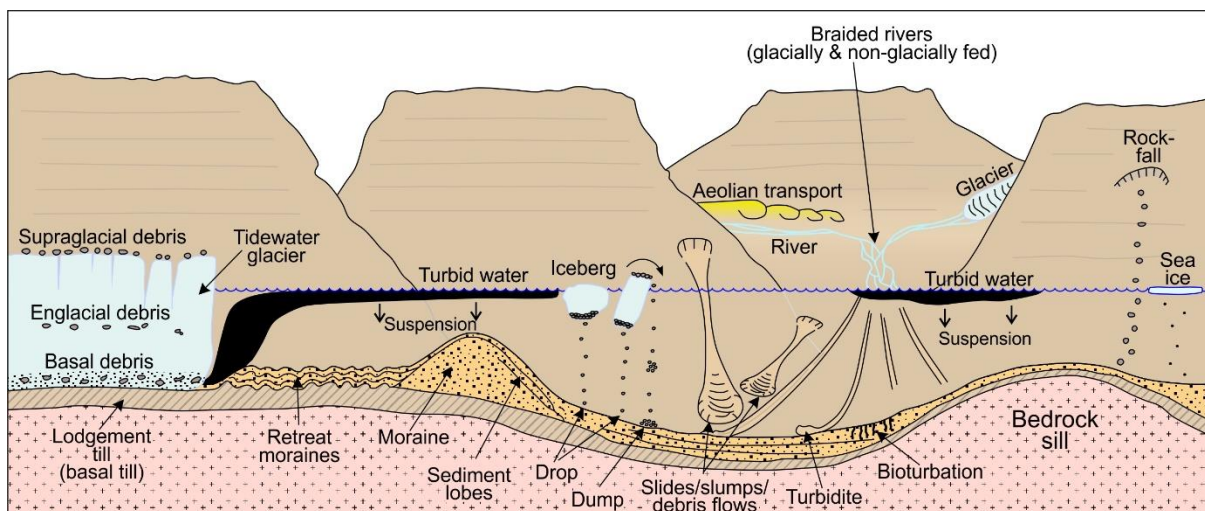


Figure 5-7. Main sedimentation processes and deposits in a glaciated fjord (from Dallmann, 2015 after Hambrey, 1994; Howe et al., 2010a).

5.3.1 Suspension settling

Suspension settling occurs when fine-grained sediments rain-out from sediment-rich meltwater plumes or fluvial inputs (Figure 5-7, Figure 2-9). The meltwater plumes originate from sub- or englacial meltwater tunnels at the glacier fronts (Syvitski et al., 1987) and carry high sediment loads (Görlich, 1988). The coarsest fraction is deposited almost immediately, while the fines are transported away from the glacier front by the meltwater plume (Elverhøi et al., 1983; Görlich, 1988; Hambrey, 1994; Syvitski et al., 1987). Deposition of the fine fraction occurs most intensely near the source, with an exponential decrease in sediment accumulation rates away from the source in tidewater environments (Elverhøi et al., 1983; Hambrey, 1994; Syvitski et al., 1987), including Wijdefjorden (Görlich, 1988). Turbulence proximal to the

glacier-front forces flocculation (aggregation) of the clay particles, though at this stage only the larger single grains and immature flocs settle. The smaller single grains and more mature flocs settle more distally, as advection slows (Görlich, 1988; Syvitski et al., 1987). Laminated fine sand to muds occur most proximally, while homogeneous mud, with or without IRD, occur more distally (Görlich, 1988).

Glacifluvial and fluvial inputs are currently of roughly similar importance to the glacial meltwater inputs (Görlich, 1988). Their relative importance will not have been as strong during periods of more extensive glaciation, and of course varies seasonally, as they and their sources often freeze in the winter, and annually as well (Cottier et al., 2010; Nilsen et al., 2008; Plassen et al., 2004). Rivers connect lakes and valley glaciers to the fjord, carrying considerable sediment loads (Forwick et al., 2010; Syvitski et al., 1987). Deposition occurs in much the same way as it does for the glacial meltwater inputs (Syvitski et al., 1987).

5.3.1.1 Distribution

All five cores contain primarily stratified/laminated and massive muds, corresponding to units L2 and L3, indicating that suspension settling is the primary source of sediments both in and beyond the fjord (Elverhøi et al., 1983; Forwick et al., 2010; Forwick and Vorren, 2009; Görlich, 1988). The homogenous muds with intermittent IRD of L3 correspond to suspension settling in a glacier-distal environment, while the laminated muds (discussed further in section 5.3.3.3), typically containing less IRD, correspond to suspension settling in a more glacier-proximal environment (Elverhøi et al., 1983; Forwick et al., 2010; Forwick and Vorren, 2009; Görlich, 1988). This has, however, not occurred uniformly throughout the fjord, as evidenced by the acoustic profile. While U2/L2 and U3/L3 typically occur as a drape, the thickness of these units is reduced in some areas. Lack of infill of depressions between some moraines and the lack of, or reduced, sediment drape over bedrock highs indicates that advection of the suspended sediments has locally dominated over the deposition of said sediments, limiting deposition in these areas. This is likely due to local currents and circulation patterns, as well as the associated winnowing processes possibly acting on deposited sediments (Syvitski et al., 1987). The influence of bottom currents through winnowing has been documented on surficial sediment samples from within Wijdefjorden, north of Nordbreen (Görlich, 1988). Winnowing of the fine fraction can lead to a coarsening of the sediments and artificially elevate the IRD signal (Benn and Evans, 2010; Stein, 2008; Vorren et al., 1984).

5.3.2 Ice rafting

Floating ice, be it from a glacier or sea ice, can transport sediments throughout the fjord and across the shelf. Sea ice can incorporate anything from suspended sediments in the water as the ice freezes to beach sediments several metres in diameter (Gilbert, 1990). Calving ice from the glacier fronts can carry large volumes of coarse sediments of sub-, en-, or supraglacial origin, which are freed as the ice melts. Debris in sea ice or icebergs can be released individually or as a rain out of many clasts from the bottom of an iceberg, through outwash if meltwater collects on the upper surface, or through dumping of freed clasts from the surface as an iceberg overturns (Figure 5-8) (Benn and Evans, 2010; Gilbert, 1990; Thomas and Connell, 1985).

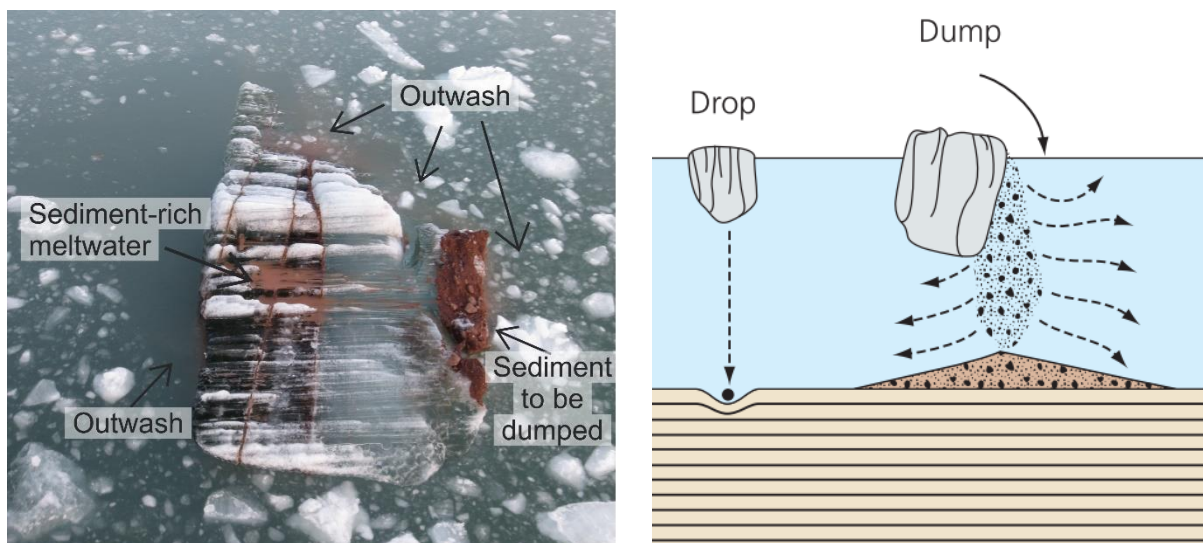


Figure 5-8. Ice rafting processes. Left: Photo of iceberg from SE of Nordaustlandet with active processes indicated. Right: Depiction of sediment dropping and dumping from icebergs (modified from Benn and Evans, 2010).

Most of the sediments are released within 200 km of the glacier front, though this is dependent on external factors such as the temperature of the water and the movement of the iceberg (i.e., speed, direction, stability), and sedimentation of IRD does occur beyond this (Benn and Evans, 2010). One important factor to consider is sea ice. When sea ice is abundant it can restrict calving, thereby reducing the sedimentation of IRD (Benn and Evans, 2010; Ó Cofaigh and Dowdeswell, 2002). It is also important to note that major dumps can deposit up to two metres of sediments, and occur less frequently with distance from the glacier front as the icebergs gradually develop a more stable shape and orientation (Benn and Evans, 2010). Other factors, such as the rate of suspension settling, can overshadow the IRD signal, leading to potentially misleading apparent increases or decreases (Plassen et al., 2004).

5.3.2.1 Distribution

IRD are present in all cores. Most cores have intervals limited IRD as well as increased IRD. In some cases, this reflects enhanced IRD deposition, however it can be due to changes in the sedimentation rate. For example, the relatively clast-rich interval between 120 and 160 cm in core 1100 represents ~6 cal. ka, while the 40 cm below this, representing just ~1 cal. ka, appears clast-poor. In this case, the rate of suspension settling changed considerably, while the deposition of IRD likely changed less. Alternatively, winnowing of the fine fraction can artificially elevate the IRD signal, as discussed in section 5.3.1. The frequency of IRD in the cores is discussed further in section 5.5. The rocky layer near the bottom of core 1085 is characteristic of an iceberg dump, with a relatively flat bottom and coarser grains on the bottom (Thomas and Connell, 1985). There is bioturbation above and below, suggesting that there was no associated change in conditions at this time, and the density of the sediments above and below is also the same, indicating that there was no unusual consolidation of the sediments. As such, the deposition of this layer in association with a surge or other depositional processes is unlikely. In the chirp profile, internal reflections are likely due to coarse layers within the sediments as discussed above (section 5.2) and are common throughout the fjord.

5.3.3 Sediment provenance

The cores contain three units, each with distinct characteristics and different provenances. The glacial till (L1) was deposited beneath the glacier or at the glacier front, while the sediments of L2 and L3 were deposited in a glaciomarine environment where suspension settling dominates and ice rafting of sediments occurs. The provenances of the sediments within each lithological unit, as well as variations between cores, will be addressed in this section, based largely on their magnetic susceptibility and the results of the XRF core scanning.

5.3.3.1 Magnetic Susceptibility

The Atomfjella complex to the east of Wijdefjorden has a strong positive magnetic anomaly that continues south, while the area to the west of Wijdefjorden is slightly negative (see section 2.1) (Dallmann, 2015). This will influence the magnetic susceptibility of a sediment core, though it is also influenced by properties such as grain size and sorting (Andrews and Jennings, 1986) and element, specifically Fe, abundance (Croudace and Rothwell, 2015). Surrounding Wijdefjorden, Fe is present in high concentrations everywhere except in the southwest.

Unit L1, glacial till, is present in cores 1091, 1095, and 1100, and always has a higher magnetic susceptibility ($\sim 46-78 \times 10^{-5}$ SI) than in L2 and L3 ($\sim 27-33 \times 10^{-5}$ SI), except L2 in core 1095 (57×10^{-5} SI) (Table 4-1). In the L1, values decrease from south to north. This suggests that sediments from the east and/or south are more common in the southern till than to the north, and than in the glaciomarine sediments. Values from L2 and L3 are highest in the middle core, decreasing more steeply to the north than the south, indicating that cores 1095 and 1100 likely receive more material from the east and south. It is possible core 1100 receives more material from the south than 1095, however, due to the outer sill that separates the two cores.

5.3.3.2 XRF results: Fe, Ti, Zr

Ti and Zr are each present in much higher concentrations in the sediments on only one side of the fjord, the east or west, respectively (Ottesen et al., 2010). Zr does deviate from this slightly, being less concentrated in the inner fjord, and present in medium concentrations in the very north of the east coast. Higher Ti/Zr ratios suggest higher sedimentation from the east. Fe has a very similar distribution and variations in concentration in the west to Zr, but is also present in the east. As such, higher Fe/Zr ratios indicate greater influence from the east as well. The Ti/Zr ratio will be used here along with the Fe/Zr ratio to examine east-west differences.

The results show that the two ratios fluctuate almost perfectly in tandem with one another. In the till, the ratios are highest in core 1091, and are similarly low in cores 1095 and 1100. This suggests a growing influence of sediments from the east in the north of the fjord. In the L2 sediments, the ratios are both lowest in core 1095, rising more to the north than to the south. The rising ratios suggest a weakening of sediment input from the west to the north and south. In L3, the ratios both steadily decrease from the south to the north, rising again slightly for core 1085. This suggests that the relative proportions of sediments from the east decrease to the north of the fjord, and that there is higher input from the west in the north, with slightly more input from the east in core 1085 than core 1091. Due to the Coriolis effect, the water masses should be deflected to the right, and that does occur in Wijdefjorden (Figure 2-9). However, the out-fjord transport of surface waters appears to be stronger, deflecting the suspended sediments from the west, originally traveling south, across the fjord and then north along the east coast of the fjord (Figure 5-9). Similar circulation could explain the weakened input from the east in the north of the fjord, and those sediments are forced closer to the coast as sediments from the west cross the fjord.

5.3.3.3 XRF results: Ca

The ratio of Ca to the sum within the cores can vary due to two factors: the concentration of lithogenic Ca in the sediments, and the rate of biogenic Ca production (Croudace and Rothwell, 2015). Ca is very high in the overbank sediments south of the fjord, and while much lower immediately surrounding the fjord, it is relatively higher to the west, and the southwest in particular (Ottesen et al., 2010). This latter corresponds to the location of the Wood Bay formation, which is also in inner Woodfjorden, and the headland to the west (Reinsdyrflya, for location see Figure 2-4). In the Woodfjorden fjord system, the high Ca in red sediments has been attributed to increased sediment delivery from the Woodfjorden branch (Hansen, 2014). In all investigated Wijdefjorden cores, higher Ca is present in sediments with a redder colour, and Ca peaks occur at the same depths as the redder laminations or stratifications. As in Woodfjorden, these layers should correspond to increased sediments from the Wood Bay formation. When high Ca (to sum) ratios are present without these redder sediments in the L1 tills, high Ca ratios are more likely to be due to material transported from the south, where there are greyish Carboniferous carbonates and evaporites. Colour differences between sediments from different areas are visible in current satellite imagery of the fjord (Figure 5-10). In the glaciomarine L2 or L3, the Ca to sum ratio can reflect the sediment sources but is more likely to have been additionally influenced by biogenic Ca production. Due to the more complex

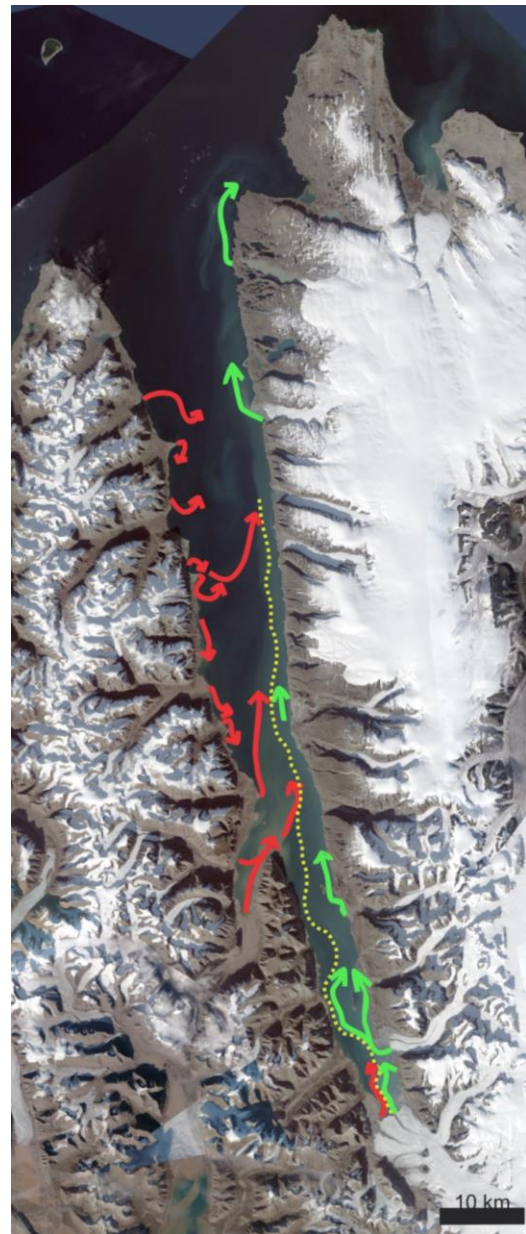


Figure 5-9. Satellite imagery from TopoSvalbard (Norwegian Polar Institute, 2018) showing suspended sediment deflection throughout the fjord. Red and green arrows show sediment plumes from the west and east respectively, while the yellow dotted line indicates where visibly red sediments (west) meet the grey (east) sediments.

factors influencing the Ca to sum ratios, this section will provide a more in-depth study of the changes and subsequent interpretations than those of the other factors above.

Within the fjord, core 1103 shows higher average Ca ratios in L2 than L3, though after the sharp decrease at the unit boundary, it does increase throughout the L3 to values near those of L2. The L2 has greyish wisps, corresponding to higher Ca ratios, within the brown sediments, likely indicating shifting environmental conditions near the glacier fronts (Forwick et al., 2010; Forwick and Vorren, 2011). Similarly, core 1100 has high Ca ratios in L1 that decrease only slightly but continuously in the L2, and lower Ca ratios in L3. The L1 in this core is predominantly very dark grey, while the L2 is grey but gradually becomes browner, with reddish wisps throughout. Here, spikes in the Ca ratio correspond to the redder intervals and the general decreasing trend is attributed to the shift from grey to brown. The L3 is brown, though it does become slightly redder (Munsell: 7.5 YR 4/2 shifts to 4/3) near the top of the core, corresponding to a slight increase in Ca through to the top of L3. Combined, this suggests that the grey sediments containing high Ca, likely sourced from south of Wijdefjorden (Figure 5-10), are most common in the till, and are present as wisps or laminations with decreasing frequency throughout the glacier-proximal sediments. The red sediments from the Wood Bay formation are present intermittently in the L2 of core 1100 only, however, they likely contribute the reddish hue to the brown sediments in the L2 and L3 of both cores, with lower, but increasing strength throughout the L3 sediments.

Moving up the fjord, the L1 of core 1095 has the highest average Ca ratios of the three tills. It is a slightly redder dark grey than the L1 of 1100 (Figure 5-11). This suggests the till has an increased proportion of Ca-rich sediments from the southwest of the fjord, and a decrease in sediments from the south. In the L2, there is a more gradual shift between the greyer sediments to the brown sediments, and it has fewer distinct red wisps. This likely indicates that the conditions in the glacier-proximal environment shifted more gradually and evenly than in the more inner cores. The red layers, however, do indicate that there were still periods of more abrupt changes with greater sediment input from the southwest. The average Ca ratio for L3 is higher in 1095 than in 1100, but still lower than in L1 and L2. It is less red than the L3 of 1100, which would be expected to lower the Ca ratio; however, there are also abundant, visible foraminifera and some shell fragments, which will raise the Ca ratio.

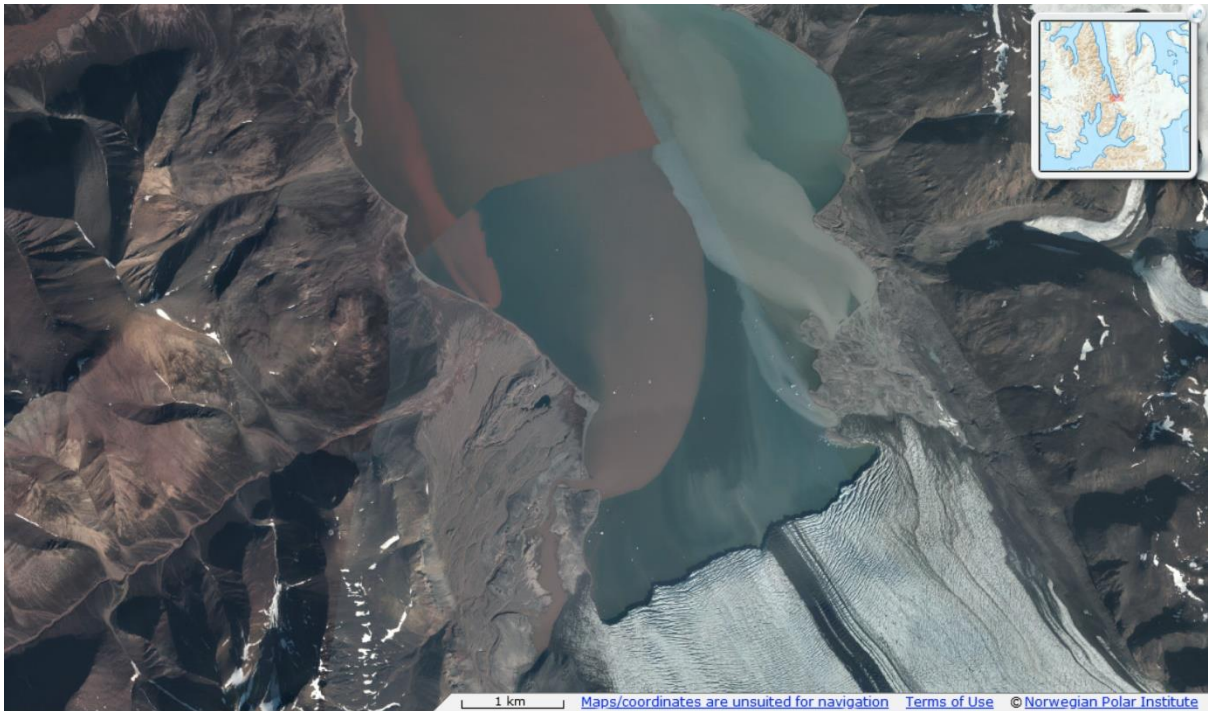


Figure 5-10. Satellite imagery from Topo-Svalbard (Norwegian Polar Institute, 2018) showing sediment-laden waters from the west (red), southeast (left glacier front, grey), and east (grey).

At the fjord mouth, core 1091 has a very low average Ca to sum ratio in the L1 and L2, that increases nearly threefold in the L3. The colour of the L1 sediments is slightly redder than the L1 in core 1100, and greyer and less red than the L1 in core 1095 (Figure 5-11). Combined with the low Ca, this suggests a decreased influence from the southwest, and thus an increasing influence of Ca-poor sediments from the northwest and perhaps the east. In L2, there are few reddish wisps, corresponding to peaks in the Ca ratio. The transition between the greyer and browner sediments occurs more quickly than in the inner cores and corresponds to a similarly sharp increase in the Ca ratio. Note, the L2 is also much thinner, and potentially low sedimentation rates could exaggerate the suddenness of this change. Comparing it to all other cores, it has the lowest Ca to sum ratio. The lower Ca values here might indicate that, while there are still some sediments from the southwest, most of the sediments are coming from the northwest and east of Wijdefjorden. In the L3, the sediments continue to have very little red and are greyer than the other cores. However, this lack of red sediments does not correspond to low Ca; in fact it has the highest average Ca to sum ratio of all units and cores. This suggests that the biogenic production of Ca increased after the transition from glacier-proximal to glacier-distal processes.

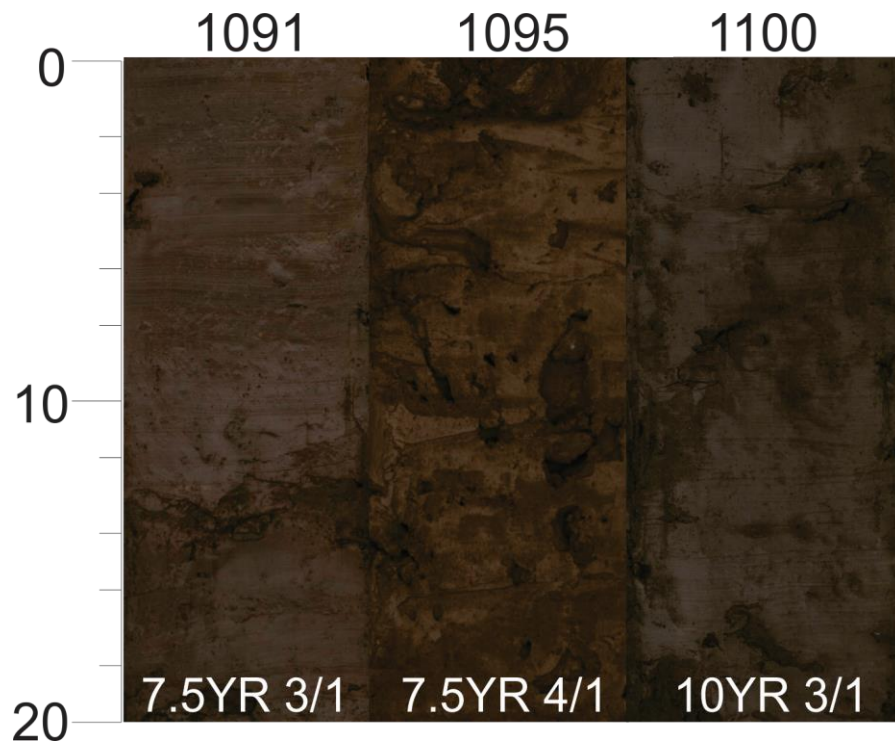


Figure 5-11. The colour difference between the L1 unit in the three cores (Munsell code indicated).

Beyond the fjord, core 1085 has high Ca ratios in both L2 and L3, though they are slightly higher on average in the L3. The correlation between Ca spikes and the redder sediments is strongest in this core, as the redder layers are often thicker than in the other cores, especially in the upper L2. In the lower part of the core, the oscillations between greyish, brownish, and reddish sediments are more like those in the other cores. The rocky layer around 365 cm, in the upper L2, likely corresponds to an iceberg dump deposit, as outlined in section 5.3.2 above. It has a high Ca ratio and other element ratios similar to those of the tills. The Ca ratio drops in the top of the core, corresponding to a decrease in the clay and an increase in the sand content, as well as a weakening of the red tint in the brown sediments. Given its location beyond the mouth of Wijdefjorden, it is probable that this core location also receives red sediments from Woodfjorden and the Wood bay formation present on Reinsdyrflya.

Combined, this suggests that the grey sediments containing high Ca, likely sourced from south of Wijdefjorden, are most common in the southern cores and the till. The reddish sediments, sourced from the Wood Bay formation, also contribute high levels of Ca to the sediments and are more present in the inner cores (1100 and 1103) and core 1085. This largely agrees with the interpretation of sediment provenance using magnetic susceptibility.

Oscillations between the greyer, redder, and browner laminations are likely representative of sediments from different sources, with the grey sediments coming from the south and east, the reds from the southwest or from Woodfjorden, and the brown possibly representing a combination of the two end-members. This likely reflects changing conditions near the glacier fronts as in other Svalbard fjords, with different areas of the fjord having periods of higher activity at different times (Forwick et al., 2010; Forwick and Vorren, 2011, 2009; Hansen, 2014; Ó Cofaigh and Dowdeswell, 2002). However, another explanation is possible. While centrifuging sediments for the grain size analysis, I observed that the red sediments often formed a layer covering the grey sediments in many samples from areas with reddish wisps (L2) but without both obviously grey and red sediments. Also, there were more particles that remained suspended in the water after being in the centrifuge, giving the water a red tinge. Comparing this to the x-rays, red sediments correspond to less dense areas with a gradational bottom and more defined upper contact (Figure 4-14). It is therefore possible the different grey-red sets could also represent more synchronous meltwater depositional events between the different areas of the fjord, but with differential settling between the grey and red sediments due to a density contrast. In the most distal core (1085), the red layers are often much thicker, though generally less well defined, near the top of the L2. This is possibly the result of longer periods with more frequent meltwater pulses alternating with periods with less frequent or less intense meltwater pulses. The more frequent pulses obscure the effect of differential settling, while in periods with weaker output, the denser material is perhaps largely deposited before reaching the core site and the finer red sediments are still transported over a longer distance.

5.3.3.4 Summary

In general, the estimates of provenance based on the different XRF results largely suggest the same trends. However, the estimates of sediment contributions from the east compared to the west differ between the Ti/Zr and Fe/Zr ratios and the magnetic susceptibility (Figure 5-12). This is likely because many factors can influence the magnetic susceptibility, and while the positive magnetic anomaly is located only in the south and east, there is also Fe throughout the catchment area, which also impacts the magnetic susceptibility. As such, this summary of sediment provenance will rely more heavily on the element ratios.

The properties of the till (L3) show that the primary provenance of the sediments is from south of each core location, and that the further north the core is from a specific area, the less influence there is from those sediments (Figure 5-12). Core 1095 (outer fjord) appears to have

the most sediment input from the southwest of Wijdefjorden. Core 1100 (central fjord) is close enough to the south to still receive more of those sediments, diluting those from the southwest, while core 1091 (fjord mouth) is further away and receives a smaller contribution of sediments from that far south. The composition of till deposits depends on many factors, among which are the basal sliding velocity. Since Wijdefjorden has been identified as the location of an ice stream, transport distances for the till material should be relatively large, possibly on the order of 50-100 km, but will also reflect the composition of the area immediately up-flow (e.g., Clark, 1987). The low Ca in core 1091, ~75 km from the northernmost Wood Bay formation, could suggest an approximate limit for the transport of those sediments northward by the ice sheet.

In the glacier-proximal sediments, the properties again suggest a relative abundance of sediments from the area immediately surrounding the core sites. On the shelf (1085), the provenance of the sediments is varied, including both Wijdefjorden headlands, and Reinsdyrflya or Woodfjorden as well. At the head of Wijdefjorden, the influence of Woodfjorden is lost. The influence from the southwest and west appears to increase in the fjord in the element ratios, however, so does the magnetic susceptibility, implying an increase in provenance from the east. In the inner fjord, the element ratios and the magnetic susceptibility agree, both suggesting an increased provenance from the south and east (Figure 5-12).

In the glacier distal sediments, the interpretation of the results suggests that the main source of the sediments is largely the area south of the core location, with core 1085 again also receiving sediments from Woodfjorden (Figure 5-12). At the mouth of Wijdefjorden, it appears the sediments are sourced from both sides of the fjord, and potentially include sediments from Woodfjorden as well. Both the element ratios and the magnetic susceptibility suggest greater provenance from the east in core 1095. In the inner fjord, the element ratios suggest an increased influence of sediment from the east, and the sediments from the southwest do not appear to influence the properties of core 1100 as much as core 1103.

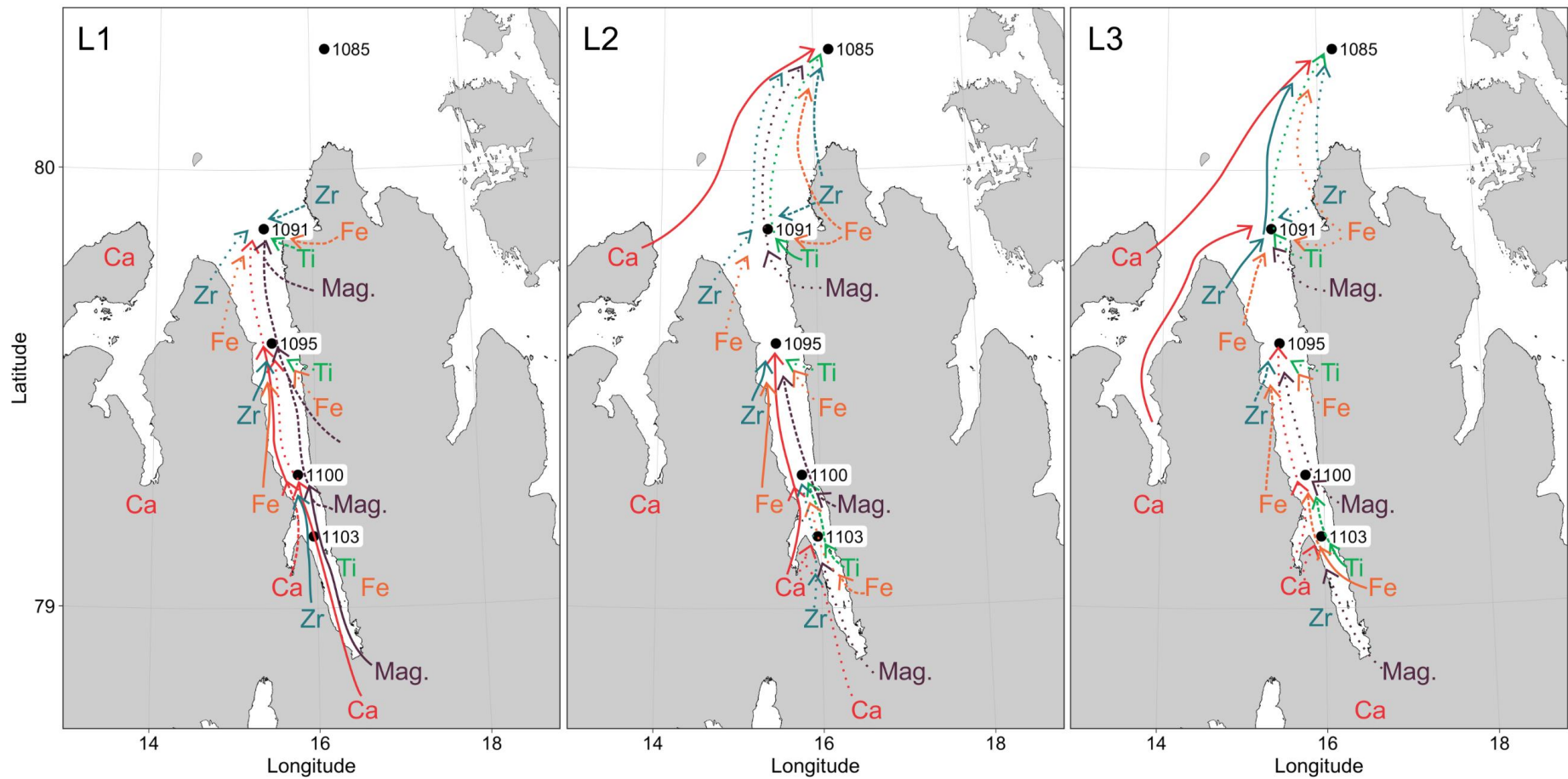


Figure 5-12. Schematic map showing possible provenance of sediments in the three units based on the magnetic susceptibility, select element ratios, and colour of the units. Solid arrows represent stronger correlation between the source and the core site, dashed arrows a moderate correlation, and dotted arrows represent a weak correlation.

5.4 Sedimentation rates

This section first addresses the calculated sedimentation rates presented in section 4.2.7, Table 4-3 (see also Figure 5-13) and how they relate to the sediments and lithological units. In some cases, cores from other studies are used to gain a better understanding of the sedimentation rates in Wijdefjorden. When possible, these rates are extrapolated to unit boundaries (Figure 5-13). Note that the top of the core has a fixed age, based on the assumption that the modern seafloor was preserved while coring, while extrapolations downcore from the lowest dates require different, additional assumptions. Due to the fixed top age and the decreased certainty of the extrapolated dates, all rates are discussed from the top of the core down in this initial discussion. Following this analysis of the rates in each core, the rates are correlated between the cores and then interpreted in a broader context with comparisons to other fjords in Svalbard; this occurs chronologically.

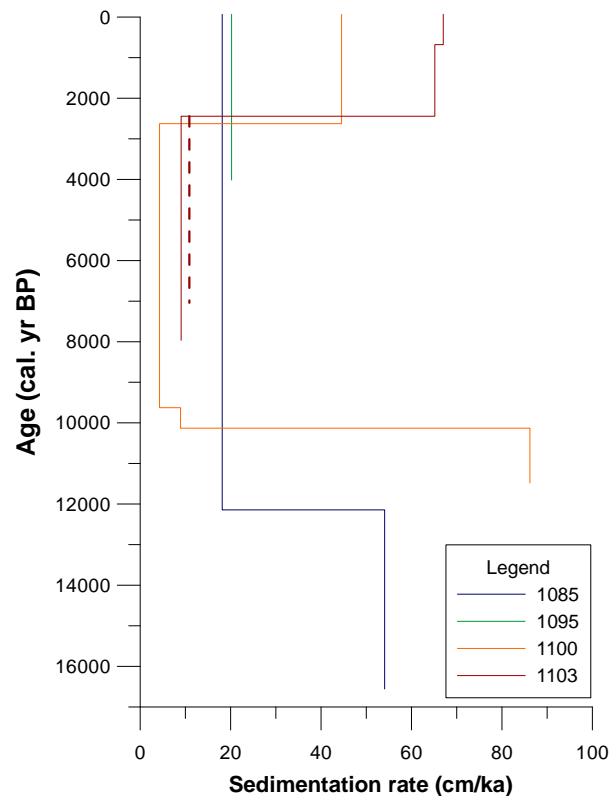


Figure 5-13. Calculated linear sedimentation rate for all dated cores, including downcore extrapolations.

5.4.1 Core 1085

There are three dates from core 1085, collected from the Wijdefjorden trough, from depths of 221.5, 326, and 365 cm (Table 4-2, Figure 4-7). The age of the mollusc sample from 365 cm was beyond the dating limit of this method. This depth corresponds to the rocky layer within

the core, suggesting these sediments are redeposited glacial sediments (Brückner and Schellmann, 2003), interpreted as being an iceberg dump deposit (see section 5.3.2). As such, it was not included in the sedimentation rate estimates. Above 221.5 cm (12 144 cal. yr BP), the sediments are mostly consistent, and the linear sedimentation rate is 18.1 cm/ka. Just below this date, at 228 cm, there is a unit boundary (L3 to L2). In the interval between 221.5 and 326 cm (12 144-14 077 cal. yr BP), the linear sedimentation rate is 54.1 cm/ka. The sediments above and below 326 cm are part of the same unit; however, their character changes around 388 cm as the laminations of different coloured sediments become thinner. Assuming this change does not correspond to a change in the sedimentation rate, the bottom of the core is ~16 650 cal. yr BP.

Comparing core 1085 to core NP94-51 from the east of the Hinlopen Trough (Figure 5-15), Ślubowska et al. (2005) found slightly higher sedimentation rates on average, and the bottom of each core has a very similar age (Figure 5-14). The lower sedimentation rates in the Wijdefjorden trough than at the east of the Hinlopen Trough could be due to the currents. Currently, there is inflow along the western side and outflow along the eastern side of the Hinlopen trench (Menze et al., 2019). This means that the Wijdefjorden site is more likely to have greater open-ocean waters, which are sediment poor, while the outflowing water will transport sediments from the Hinlopen Strait to the Hinlopen Trough site.

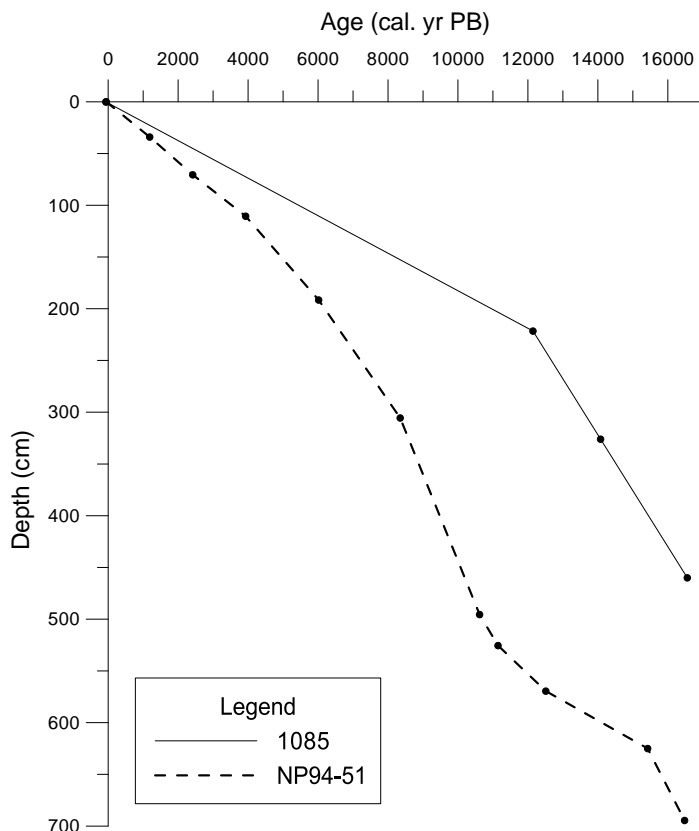


Figure 5-14. Age-depth plot comparing core 1085 to a core from the east of the Hinlopen Strait (NP94-51, for location see Figure 5-15) (Ślubowska et al., 2005). Note: the deepest/oldest point for core 1085 is an extrapolation based on the sedimentation rate above the lowest dated interval (326 cm).

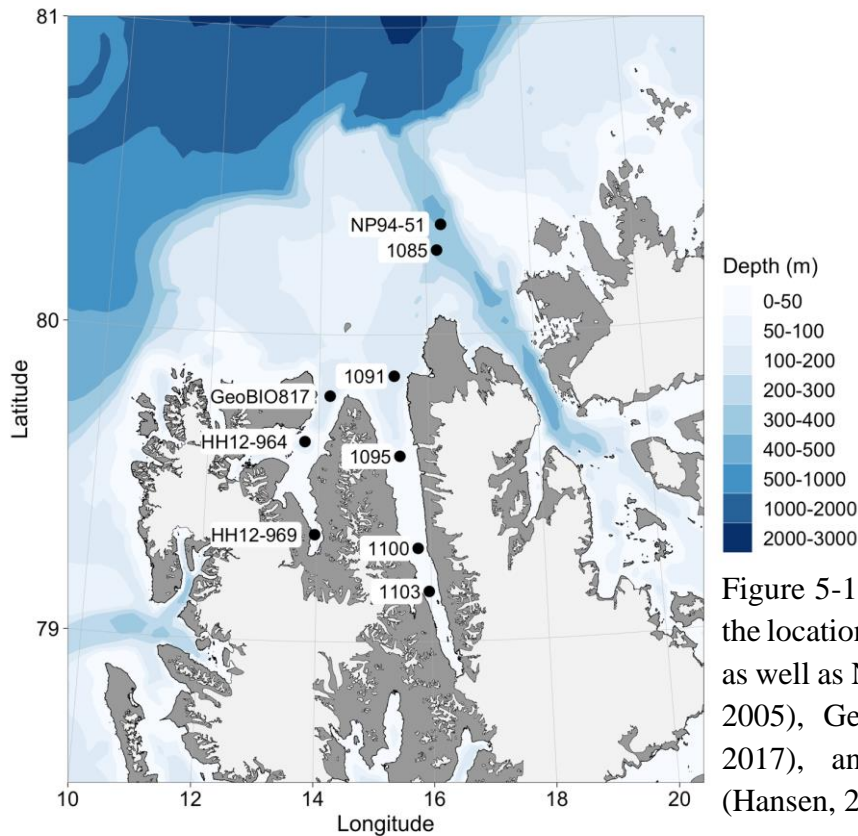


Figure 5-15. Overview map showing the locations of the cores in this study, as well as NP94-51 (Ślubowska et al., 2005), GeoBIO817 (Bartels et al., 2017), and HH12-964 and -969 (Hansen, 2014).

5.4.2 Core 1091

As no datable material was collected from this core, no sedimentation rates have been calculated. However, the presence of all three lithological units in this 86 cm long core indicate that sedimentation rates are much lower than in the other cores.

5.4.3 Core 1095

In core 1095, the linear sedimentation rate is 20.2 cm/ka above 82.5 cm (4015 cal. ka BP) (Figure 5-13). This encompasses the majority of L3, since the top of L2 is at 90 cm. Below the dated interval, the sediments are much coarser in general, and include glacial till. As such, I cannot assume the sedimentation rate is similar below this point and have not extrapolated the values downcore. A core (JM-09-11) retrieved from between cores 1095 and 1100, on the plateau in Wijdefjorden, has been dated as well (Forwick et al., 2011). It has a date of 4701-4821 cal. yr BP at a transition from coarse to finer sediments, like the transition within the L3 of 1095. Only ~10 cm below this date is another of 8918-9064 cal. yr BP, indicating very low sedimentation rates during that period. It is therefore possible the transition from L2 to L3 occurred much earlier in core 1095 than the sedimentation rate for the upper core suggests.

5.4.4 Core 1100

The uppermost sample (120 cm) from core 1100 shows that the linear sedimentation rate has been relatively high (44.5 cm/ka) in mid-Wijdefjorden since 2627 cal. ka BP. From 150-120 cm (9626-2627 cal. yr BP), the linear sedimentation rate was much lower: 4.3 cm/ka. In this part of the core, the sediments are slightly coarser, with more sand and clasts. The rate between 154.5-150 cm (10 130-9626 cal. yr BP) was also low, at only 8.9 cm/ka (Figure 4-21), and marks the lower bound of the coarse section. However, the sedimentation rate was much higher (86.2 cm/ka) between 10 948 and 10 130 cal. yr BP (225-154.5 cm). The physical properties and appearance of the sediments between 154.5 cm and 271 cm, i.e., the bottom of L3, are consistent, and relatively similar to those of the top of the core. Assuming the sedimentation rate above 225 is the same as below, the bottom of L3 would have an age of approximately 11 480 cal. yr BP.

Comparing this again to JM-09-11, the low sedimentation rates around 3-9.4 cal. ka BP correspond well to each other. However, the minimum date (~9.3 cal. ka BP) for the transition from the grounding-zone wedge to glacier-proximal sediments in JM-09-11 is approximately 2 ka younger (Forwick et al., 2011) than the estimated date for the bottom of the L3 in core 1100. While it is possible that the estimated date is too old, with three dates greater than 9 cal. ka BP within the L3 sediments it is unlikely that it is that much too old. As such, I suggest that the glacier front retreated from the mid-fjord before ~11.5 cal. ka BP, and not shortly prior to 9.3 cal. ka BP.

5.4.5 Core 1103

The dates from inner Wijdefjorden (core 1103), show that the linear sedimentation rate was high (67.0 cm/ka) from 679 cal. yr BP (50 cm) to 2017. Between 2444 and 679 cal. yr BP (165-50 cm), it was only slightly lower, at 65.2 cm/ka (Figure 5-13). The sediments throughout the top of the core are quite consistent, with only a slight increase in IRD around 110-75 cm. Below this, the dates from 208.5 cm and 210 cm show an age reversal: the sample from 208.5 cm is 669 cal. years older than that from 210 cm (Table 4-2). It is a small reversal, though large enough that the dates do not fall within the 1σ ranges of the other.

Age reversals can occur for many reasons and are commonly due to sediment reworking (Lloyd et al., 1996). However, the lamination of different coloured sediments and the absence of any erosional features in this section of the core do not support this possibility, as they suggest uninterrupted sedimentation. Therefore, I assume the age difference is a result of using different

species for the analysis; the lower, or younger, date is from an unidentified mollusc species (S.-I. Nam, pers. comm.), whereas the upper, or older, date is from a monospecific (*N. labradorica*) foraminifera sample. The different species may have lived at different places on or within the sediments. *N. labradorica* are infaunal, living within the top 5 cm of the sediments, with higher abundances between 1-2 cm below the surface (Wollenburg, J. E. & Mackensen, 1998). The mollusc could have been infaunal, like the foraminifera, or epifaunal. If it was an infaunal bivalve, it could have been living potentially up to 20-25 cm (Zwarts and Wanink, 1989) deeper in the sediments than the foraminifera, resulting in the younger, deeper, age. Additionally, without knowing the class or condition (i.e., whole, half, or fragment) of the mollusc sample, it is impossible to accurately evaluate the reliability of the resultant date. Given the similarity between the dates obtained from the *N. labradorica* sample and the other foraminifera species from the same depth in core 1095, it is more likely this date is more reliable. As such, the sedimentation rate (9.1 cm/ka) from the *N. labradorica* date will be used. Extrapolating this sedimentation rate to the bottom of the core (215 cm) gives an age of ~7966 cal. yr BP. However, due to the change in lithological unit just below the dated interval, there is a greater probability of the sedimentation rate having changed and this date being incorrect.

5.4.6 Correlations between Wijdefjorden cores

The highest sedimentation rates in the Wijdefjorden trough (core 1085) occurred from ~14.1-12.1 cal. ka BP, representing almost exclusively L2 sediments. This is the only rate for L2 sediments from any core. Sedimentation rates are typically highest near the glacier front (Elverhøi et al., 1983), so it follows that the highest rates occurred there. The approximate age of the transition between L2 and L3 sedimentation is ~12.2 cal. ka BP in the Wijdefjorden trough (1085), before 4.1 cal. ka BP and possibly before ~9 cal. ka BP, as discussed above, in the outer fjord (1095), ~11.5 cal. ka BP in the inner fjord (1100), and ~7.2 cal. ka BP in the inner fjord (1103). Note that the date from 1103 is very young compared to the others, and likely does not represent the first change from glacier-proximal to glacier-distal sedimentation in the inner fjord; this is discussed further in section 5.5.2. Only two cores, 1100 and 1085, have dates older than 10 cal. ka BP. The oldest dates in core 1100 suggest that sedimentation rates are higher in the fjord (86 cm/ka) between ~10.1 and 10.9 cal. ka BP, and possibly earlier. The high sedimentation rate at that time is within the range of those at the mouth of Woodfjorden, where there were rates of ~120 cm/ka between 11 and 10.5 cal. ka BP and of ~65 cm/ka from 10.5 to 10 cal. ka BP, associated with high levels of meltwater runoff due to

further glacier disintegration (Bartels et al., 2017). These are also oldest L3 sediments, which were deposited during the generally warm period of the early Holocene (e.g., Butschek et al., 2018; Chauhan et al., 2016b; Salvigsen and Österholm, 1982), therefore it is likely that these higher rates are due to a rapid retreat of the glaciers in Wijdefjorden.

During the period between ~10.0 and 2.5 cal. ka BP, sedimentation rates were lower (~4-20 cm/ka), with the lowest values occurring in the innermost two cores (~4-11 cm/ka). The slightly higher rates from the Wijdefjorden trough (1085) could indicate that sediments were bypassing the inner core locations, and that core 1085 on the shelf receives additional sediments from sources other than Wijdefjorden itself (section 5.3). Low sedimentation rates at this time are also found in central Woodfjorden (~18-19 cm/ka, Hansen (2014)). This roughly corresponds to the cooling since ~8 cal. ka BP (Baeten et al., 2010; Forwick and Vorren, 2009, 2007; Hald et al., 2004; Plassen et al., 2004; Svendsen and Mangerud, 1997), which allowed glacier growth and reduced meltwater input.

The two innermost cores (1100 and 1103) have high sedimentation rates (44-67 cm/ka) in the last ~2.5 cal. ka BP (Figure 5-13). Higher sedimentation rates for the last ~2-3 cal. ka BP are also present in other Svalbard fjords; for example rates of ~60 cm/ka since 2.3 cal. ka BP (Plassen et al., 2004) and ~80 cm/ka since 1.3 cal. ka BP (Rasmussen et al., 2013) in different areas of Isfjorden, and 49-81 cm/ka since ~2.7 cal. ka BP in inner Woodfjorden (Hansen, 2014). These higher rates generally correspond with increased meltwater production (Rasmussen et al., 2013). The lack of dates in the upper sections of cores 1085 and 1095 make it impossible to tell if this most recent higher sedimentation rate applies to cores beyond the sill in central Wijdefjorden. As many of the larger remaining glaciers and the highest glacier cover is currently in the Austfjorden SDB (Figure 2-5), most of the sedimentation in the fjord is likely to occur in the inner fjord. In general, sedimentation rates decrease with distance from the head of Wijdefjorden (Figure 5-13), as in other fjords (e.g., Hansen, 2014). Additionally, low sedimentation rates from the Hinlopen Strait (Ślubowska et al., 2005) support continued low sedimentation rates beyond the mouth of the fjord at least.

5.5 Paleoclimate and environment of Wijdefjorden since the Late Weichselian

The reconstruction of conditions during the Late Weichselian and early Holocene is based primarily on the dates from cores 1085 and 1100, as they are the most well dated, though only core 1085 has dates from the Late Weichselian. Dates from the mid to late Holocene are present

in cores 1095, 1100, and 1103, though only 1103 has more than one date from this time period. Core 1091 was not dated and is therefore not included in this reconstruction.

5.5.1 Late Weichselian (>11.65 cal. ka BP)

The extrapolated age of the bottom of core 1085 indicates the shelf beyond Wijdefjorden was presumably deglaciated before ~16.6 cal. ka BP, similar to a minimum date from the Hinlopen Strait (Ślubowska et al., 2005) and from the Kongsfjorden trough (Henriksen et al., 2014). It is possible this occurred even earlier, as the chirp profile reveals additional sediments, interpreted as glacier-proximal glaciomarine sediments with clast-rich layers, below the bottom of the core. Deglaciation on the Svalbard margin began around 20 cal. ka BP (Jessen et al., 2010). However, parts of the shelf north of Nordaustlandet were not deglaciated until after 14.0 cal. ka BP (Fransner et al., 2018), and others have found that the retreat of ice on the shelf north of Svalbard did not start until ~16 ka (Hormes et al., 2013; Knies et al., 2000) so this date may reflect the minimum deglaciation age of the Wijdefjorden cross-shelf trough only, and not that of the whole shelf.

Within the fjord, there are only dates from the Holocene; however, the extrapolated date for the transition from L2 to L3 in core 1100 of ~11.5 cal. ka BP shows that the majority of the L2 in that core was likely deposited during the Late Weichselian as well (Figure 5-16). This indicates that most glaciers must have retreated to an inner fjord position by the end of the Late Weichselian. As such, the L2 of the cores from the outer fjord and fjord mouth (1091 and 1095) were likely also deposited prior to the Holocene. This is consistent with a deglaciation of central Wijdefjorden by around ~14 ka (Hormes et al., 2013).

On the shelf (core 1085), suspension settling was the primary sediment source, indicating high levels of meltwater from the retreating ice. The sediments are characterized by thin laminations of sediments with different colours and densities. The redder sediments are interpreted to have come from Woodfjorden and Reinsdyrflya (for location see Figure 2-4), as in Hansen (2014), while the grey sediments are derived from northern Wijdefjorden, suggesting oscillations in the strength of the meltwater inputs from each area. After ~15.6 cal. ka BP, larger intervals with brownish sediments are present between sets of redder laminations to stratifications. Deglaciation of Reinsdyrflya occurred around 15-14 ± 1ka, which could correspond to the shift from laminated to stratified sediments. Within the stratified sediments, the brown intervals are interpreted to reflect periods of more uniform meltwater output from Wijdefjorden, with contributions from Woodfjorden, while the redder sediments are again interpreted to

correspond to periods of greater meltwater output from Woodfjorden. This correlates well to periods of intensive meltwater outflow recorded in a core at the mouth of Woodfjorden prior to ~14 cal. ka BP identified by Bartels et al. (2017).

There are internal reflections interpreted as clast-rich intervals below the bottom of core 1085, likely associated with fluxes of coarser sediments during the initial deglaciation. In the core itself there are no clasts >1 mm (IRD) until a clast-rich interval ~3 cm thick, interpreted as being from an iceberg dump, with an extrapolated age of around 14.8 cal. ka BP. After this iceberg dump deposit, IRD are more common in the core. This renewed IRD deposition corresponds well to observations suggesting AW returned to the bottom waters south of Svalbard around 15 cal. ka BP (Bauch et al., 2001; Rasmussen et al., 2007) and to the north of the Hinlopen Strait at the same time (Ślubowska et al., 2005). As in other fjords, the AW likely helped destabilise the ice in the fjord and increase IRD production (e.g., Bartels et al., 2017; Nielsen and Rasmussen, 2018). The timing of increased IRD on the shelf contrasts, however, with findings from the mouth of Woodfjorden, which appears to have experienced this effect earlier, and less continuously. At Woodfjorden, there are records of high IRD until ~14.6 cal. ka BP, then no IRD until ~14 cal. ka BP, after which it started increasing again (Bartels et al., 2017).

The three cores from the fjord mouth to the central fjord (1091, 1095, 1100) have few IRD in the bottom of the L2, though cores 1091 and 1095 do have some clast-rich laminations, while in the top, clasts and clast-rich laminations and lenses are more abundant. Core 1100 has increasing IRD near the top of the L2, but has no IRD in the uppermost section of L2. From the shelf to the mid-fjord, this suggests a general increase in ice-rafting at some point in the Late Weichselian, likely as the glaciers in the fjord retreated further. However, a lack of dates from the L2 means the timing of this shift within the fjord remains unknown. Despite the mismatch in IRD records from Woodfjorden to the shelf, the trend of greater IRD and a general coarsening in the core from Woodfjorden between ~14 and 12.7 cal. ka BP does correspond well to the increased IRD in the top of the L2 in most fjord cores. In Woodfjorden, it has been interpreted as a retreat of at least some glaciers to a more distal position (Bartels et al., 2017), associated with advection of warm AW to the fjord (Bartels et al., 2017). It is possible that this occurred in Wijdefjorden as well.

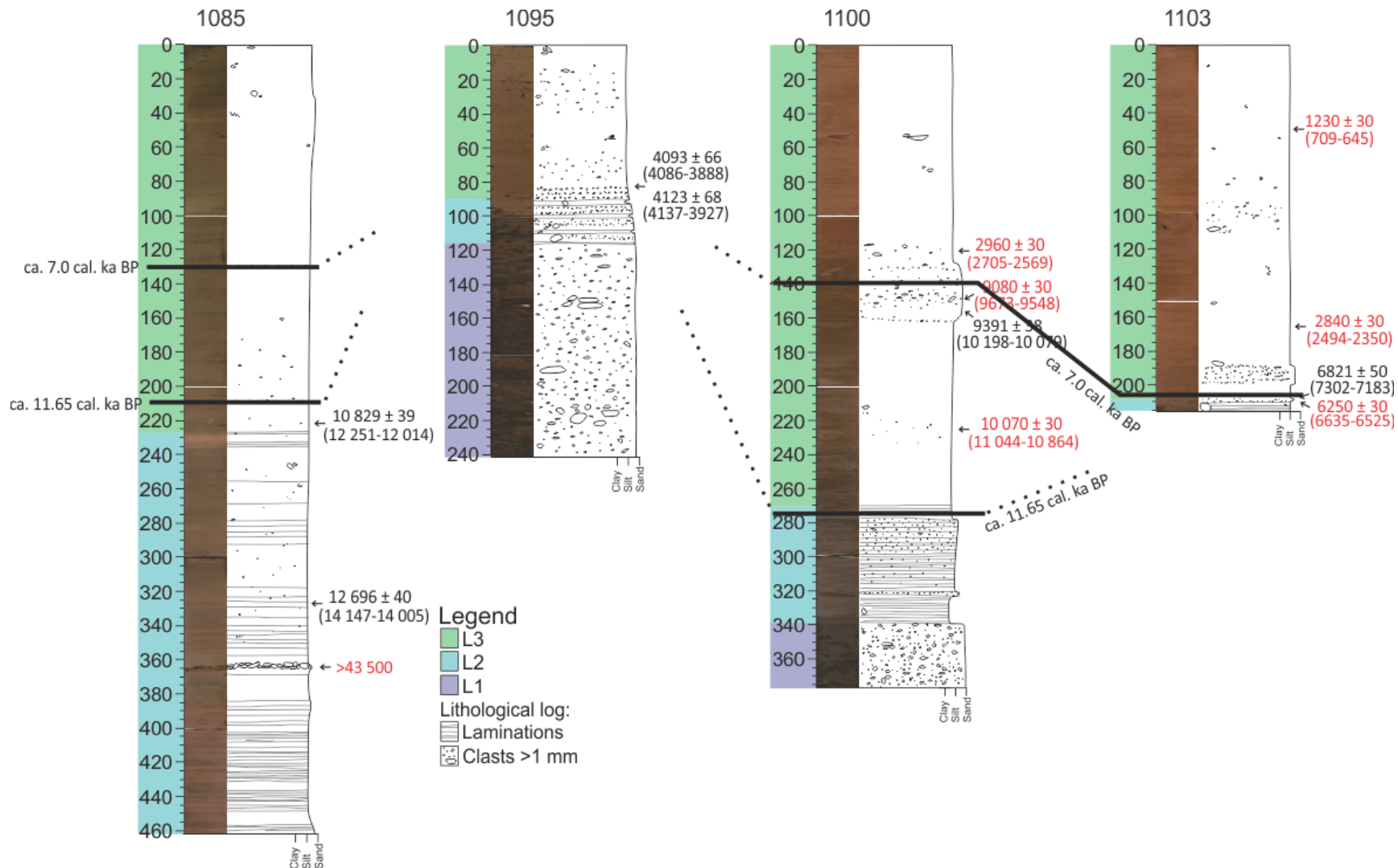


Figure 5-16. Lithological logs and photos of the four dated cores, from north (left) to south (right). The dates are indicated (^{14}C years above and calibrated years B.P. below), including those from S.-I. Nam, pers. comm. (red), and the approximate depths of the Late Weichselian to early Holocene boundary (11.65 cal. ka BP) and the early to mid-Holocene boundary (7.0 cal. ka BP).

The transition from L2 to L3 on the shelf (1085) occurs near the end of the Late Weichselian, around 12.2 cal. ka BP, in the middle of the Younger Dryas. It is marked by the top of the last interval of red laminations and stratifications, after which the homogenous brown sediments continue to the top of the core. This transition marks a slight decrease and a steadying of the influence of sediments from Woodfjorden, and likely further retreating glaciers (section 5.3.3). Any potential influence of the Younger Dryas cooling is not clearly reflected this far away from the fjord. In core 1100, an extrapolated date shows that the end of the Late Weichselian corresponds roughly to an abrupt decrease in IRD after it increased for some time. The increase in IRD could be indicative of increasing glacial activity due to the Younger Dryas cooling. However, at this time enhanced meltwater production isolated the warm AW from the air causing the sea surface temperature (SST) to fall, which may have enabled sea ice expansion and the suppression of glacier calving (Bartels et al., 2017; Butschek et al., 2018; Chauhan et al., 2016a). Other studies have also found low IRD during this time (e.g., Forwick and Vorren, 2009). In general, the Younger Dryas period meant greater sea ice, and cold surface and bottom waters north of Spitsbergen. The Polar Front was likely near the Hinlopen Strait before moving northward at the end of the Younger Dryas (Ślubowska et al., 2005). As such, greater IRD during the Younger Dryas is unusual, but could be due to enhanced sea ice rafting or glacier calving in a seasonally sea-ice free environment.

5.5.2 Early Holocene (11.65-7.0 cal. ka BP)

The early Holocene was a period with higher temperatures and a greater influx of AW to northern Svalbard (Bartels et al., 2017; Butschek et al., 2018; Chauhan et al., 2016b; Salvigsen and Österholm, 1982). A two-step warming has been observed in Svalbard (Koç et al., 2002; Lehman and Forman, 1992; Ślubowska et al., 2005). The final collapse of the SBIS, likely related to further advection of AW, is indicated by high IRD fluxes to the Svalbard shelf immediately prior to 10 cal. ka BP (e.g., Landvik et al., 2005; Lehman and Forman, 1992; Nielsen and Rasmussen, 2018; Ślubowska et al., 2005). Conditions, climatically and oceanographically, were warm in the south and west of Svalbard between ~11.2 and 8 cal. ka BP (Forwick and Vorren, 2009; Hald et al., 2004; Rasmussen et al., 2013, 2007). Conditions appear to have been warmest between ~9 and 8 cal. ka BP in many areas, including the Hinlopen Trough and Isfjorden, as well as to the southwest of Svalbard (Rasmussen et al., 2013, 2007), and on the northern coast of Spitsbergen near Wijdefjorden (Salvigsen, 2002). However, the increased AW advection did not result in strong warming along the northern Spitsbergen margin (Ślubowska et al., 2005).

In Wijdefjorden, extrapolated dates show that the transition from L2 to L3 in core 1100 occurs just after the start of the Holocene (~11.5 cal. ka BP) (Figure 5-16). This is about 700 years after the L2 to L3 transition in core 1085 (~12.2 cal. ka BP) on the shelf, suggesting a retreat of most glaciers in Wijdefjorden by this time, despite the Younger Dryas cooling. Note that cores 1091 and 1095 do not have dates from this time, so it is possible glaciers were more active locally and that glacier-proximal conditions near those cores remained later into the Holocene. The date from core 1100, in the central fjord, is similar to that of a period with high IRD and an influx of warm AW in Hinlopen (Ślubowska-Woldengen et al., 2007). It is slightly earlier but similar to dates for the deglaciation of other Svalbard fjords, which are often around 11.3-10 cal. ka BP (e.g., Baeten et al., 2010; Bartels et al., 2017; Forwick and Vorren, 2009; Fransner et al., 2017; Hald et al., 2004; Hansen, 2014; Salvigsen and Høgvard, 2005; Svendsen et al., 1996). This suggests the timing of the complete deglaciation in Wijdefjorden was likely quite similar. However, this date does not come from the head of the fjord, as the others do. It is likely the inner fjord was deglaciated shortly thereafter. However, the estimated date of the transition between L2 to L3 in the innermost core (1103) shows conditions in the inner fjord have been consistently glacier-distal since ~7.2 cal. ka BP. It is important to note that core 1103 contains less than 10 cm of L2, so it is possible glacier-distal conditions existed prior to that date as well, and that this may not represent the initial deglaciation of the inner fjord. This will be discussed further at the end of this section.

The primary difference at the transition from L2 to L3 sediments is that any oscillations of the conditions at the glacier fronts were not felt at the core locations, and/or that the meltwater production steadied. After the transition from glacier-proximal to glacier-distal conditions in cores with sediments of this age (i.e., all but 1103, which will be discussed separately), conditions appear to have been similar until the top of the core, as the sediments lack obvious changes in physical properties and geochemistry. However, slightly after the unit change, the dates in core 1100 show that the sedimentation rate is much lower above ~10.9 cal. ka BP, similarly to that of a core (HH12-969, Figure 5-15) from central Woodfjorden (Hansen, 2014). There is an apparent increase in IRD in the core just above this point, however the low sedimentation rates suggest this is instead a decrease in the deposition of sediments from suspension, with some ice rafting still occurring until the late Holocene. The other cores in the north of the fjord (1091 and 1095) are not as well dated near this change but may have experienced low sedimentation rates in the L2, or a rapid retreat of the ice front with only a short window of glacier-proximal sedimentation, as they are very thin. They are relatively

coarse, likely due to some degree of ice rafting occurring at the same time as limited suspension settling. However, the thinness of the units could also be due to winnowing of the fine sediments, a process that could have been enhanced by the rapid isostatic uplift in the early Holocene (Forman et al., 2004; Syvitski et al., 1989; Vorren et al., 1984). On the shelf, there is no IRD in the core from ~9.3 cal. ka BP until the late Holocene, indicating an extended period of limited ice rafting. Records from the western shelf also show very limited IRD during that time (Andersen et al., 1996), which is the inverse of what occurred in many western fjords, where increased IRD are reported between ~9 and 4 cal. ka BP (e.g., Forwick and Vorren, 2009; Hald et al., 2004). This trend of ongoing IRD deposition in the fjords but not on the shelf is present in Wijdefjorden.

Glaciers in Bockfjorden were less extensive than they are today for much of the Holocene (Salvigsen and Høgvard, 2005), and glaciers in Woodfjorden also retreated (Bartels et al., 2017). Similarly smaller glaciers in Wijdefjorden could be the cause of the low sedimentation rates, while the ongoing presence of IRD in the fjord likely indicates that some tidewater glaciers were still present, as in Woodfjorden (Bartels et al., 2017). It is possible the glaciers to the south and perhaps also in Vestfjorden were still relatively active for some amount of time prior to ~7.2 cal. ka BP, the transition from L2 to L3 in the inner fjord (core 1103), and contributed to the IRD found in the more northern cores. However, the sedimentation rate is similarly low at this age in the core, despite the more glacier-proximal sedimentation, so the glaciers were likely not highly active.

The late transition from L2 to L3 in core 1103 at the end of this interval (~7.2 cal. ka BP) possibly represents the deglaciation of the inner fjord. However, the glacier-proximal sediments it contains may instead represent a period of renewed glacier growth after the deglaciation. The dates from the central fjord (core 1100) clearly show that the outer sill was deglaciated by ~11 cal. ka BP. Between there and the location of core 1103, there is a small basin, as core 1103 is on the south side of a small rise (Figure 2-6). It is likely that the ice receded across this deeper area relatively quickly. It is possible the small rise acted as a pinning point. However, it is unlikely that the ice remained here for the entire time as the early Holocene was very warm until ~8 cal. ka BP (Forwick and Vorren, 2009; Hald et al., 2004; Rasmussen et al., 2013, 2007). Additionally, the change to L3 sediments occurred at the same time as the relatively warm conditions in the Hinlopen Strait came to an end also around 7.2 cal. ka BP (Ślubowska-Woldengen et al., 2007; Ślubowska et al., 2005). The glaciomarine sediment

thickness is greater in this basin than at any point north of this (Figure 5-1), which could support that the glacier front was there for some amount of time. However, this greater sediment thickness is likely in part due to the basin's location just north of Vestfjorden and the generally greater sedimentation associated with its proximity to that and the head of Wijdefjorden (Figure 2-6). The inner sill to the south, however, is only 18 m b.s.l. at present, and could have been a stronger pinning point. Again, it is unlikely it was pinned there for ~3 cal. ka throughout the warm early Holocene and it is probable that the ice front retreated from that position prior to this. Additionally, there is no obvious reason for a retreat at that time, as it was during a period of general advance on Svalbard (Baeten et al., 2010; Forwick and Vorren, 2009, 2007; Hald et al., 2004; Plassen et al., 2004; Svendsen and Mangerud, 1997). It is also ~35 km south of the core location, so glacier-proximal sedimentation would be less likely at that distance (Elverhøi et al., 1983). It is possible that this simply represents greater glacier-proximal sedimentation from the nearby valley glaciers, including those in Vestfjorden, and possibly rivers as well, since both contribute suspended sediments to the fjord. This could have occurred as a surge, as it is out of phase with the general warming and cooling trend, and surges are very common on Svalbard (Farnsworth et al., 2016). The high Ca-content suggests greater input from the southwest and Vestfjorden, while the grey colour of the laminations means periodic inputs from the east were also important.

5.5.3 Mid to late Holocene (7.0 cal. ka BP - present)

The transition to the mid-Holocene occurs within the L3 at about 128.5 cm in core 1085, 139 cm in core 1100, and 206 cm in core 1103 (Figure 5-16). The mid-Holocene was likely a time of decreased summer insolation and regional cooling, with reduced AW, lower SST and increased sea ice, and IRD fluxes in Svalbard fjords (Baeten et al., 2010; Forwick et al., 2010; Forwick and Vorren, 2009; Hald et al., 2004; Koç et al., 2002; Rasmussen et al., 2013; Ślubowska et al., 2005). The dates from the two innermost cores show that this was a period with low sedimentation rates and some IRD; however, there are no IRD from this time interval in core 1085 from the shelf. There was a transition to more ice-proximal conditions in the Hinlopen Trough over the course of the mid-Holocene (Ślubowska et al., 2005), however, this is not evident in the cores from Wijdefjorden, where IRD deposition and sedimentation rates appear to remain stable and low during this time.

In Svalbard, the last 4 cal. ka BP have been relatively cool and stable (Bauch et al., 2001; Butschek et al., 2018; Forwick and Vorren, 2009; Hald et al., 2004; Rasmussen et al., 2014,

2013; Svendsen and Mangerud, 1997), with fluctuating but generally greater sea ice and less AW (Chauhan et al., 2016a, 2016b; Jernas et al., 2013). There is an apparent increase in IRD in most cores. Extrapolating the ~12 cal. ka BP date from the shelf (1085) gives the reappearance of IRD in that core a very rough age of ~3.2 cal. ka BP. In the outer fjord (1095), there is a gradual increase in IRD from ~2.9 cal. ka BP to 1.4, after which they are more abundant. In the mid-fjord (core 1100), there are a few IRD around the dated interval of 2.6 cal. ka BP, and a few between ~1.6 and ~1.0 cal. ka BP, however the rest is devoid of clasts. In the inner fjord, core 1103 has a gradual increase in IRD from ~3.5 to 1.6 cal. ka BP, while in the last ~1.0 ka there are again very few IRD. This suggests that ice rafting began to increase from around ~3.5 cal. ka BP, similar to an increase in ice rafting in western Svalbard at ~2.9 cal. ka BP (Kempf et al., 2013). This also corresponds to the general cooling, which allowed renewed glacier growth (e.g., Bartels et al., 2017; Forwick and Vorren, 2009; Nielsen and Rasmussen, 2018; Ślubowska et al., 2005). The IRD deposition in and north of Wijdefjorden reached a maximum from ~1.5 to 1.0 cal. ka BP, but became more limited in the last thousand years. At 1.5 cal. ka BP, a short period of increased AW advection led to reduced sea ice cover, possibly allowing the deposition of more IRD at that time (Chauhan et al., 2016b). However, in other Svalbard fjords, decreased IRD flux is observed after ~4 cal. ka BP (e.g., Forwick and Vorren, 2009; Hald et al., 2004). A period of harsher condition reported from 450 to 50 BP, with nearly perennial sea ice (Chauhan et al., 2016b; Jernas et al., 2013) is not as clear in the inner and mid-fjord, though the cores from the shelf and outer fjord do have more IRD in the uppermost ~10 cm, roughly corresponding to that time period. It appears as though the IRD deposition in Wijdefjorden is opposite to that in other areas; however, this could simply be due to poor age controls on the most recent sediments. The sedimentation rates in cores 1100 and 1103 increase after ~2.6 cal. ka BP, likely the result of increased meltwater production and suspension settling. This is similar to some other Svalbard fjords (Forwick and Vorren, 2009; Hansen, 2014; Plassen et al., 2004).

6 Summary and Conclusions

Chirp data and five sediment cores from the continental shelf north of Wijdefjorden to inner Wijdefjorden were analysed and correlated with each other in order to reconstruct the deglaciation dynamics and sedimentary environments of the fjord and shelf during the Late Weichselian and the Holocene.

- The chirp data show two regional reflections: the lower reflection represents the top of the bedrock or a glacial till (U1) throughout most of the profile, and the upper represents the present seafloor.
- Two additional units occur with varying thicknesses between the regional reflectors: U2, interpreted as glacier-proximal sediments, and U3, interpreted as glacier-distal sediments. Both units tend to appear as a drape over the underlying units and are thicker in the basins, particularly in the inner fjord, than over bathymetric highs where they sometimes disappear completely. The glacier-proximal deposits (U2) frequently fill in depressions in U1.
- Internal reflections and less transparent or more chaotic areas within these units are interpreted as having more clasts, with the former often correlating with IRD-rich intervals. These reflect periods of enhanced ice rafting from icebergs and/or sea ice
- Three lithostratigraphic units are defined: L1 is glacial till, L2 is glacier-proximal sediments, and L3 is glacier-distal sediments.
- The cores reveal that suspension settling of fine-grained sediments from turbid meltwater plumes, from both tidewater glaciers and rivers, is the primary sedimentary process in the fjord, along with ice rafting of debris by icebergs and sea ice. Ice rafting is relatively more important in the outer fjord and at the fjord mouth than in the central to inner fjord or on the shelf.
- Sedimentation rates are generally higher (54.1-86 cm/ka) in the glacier-proximal deposits (L2) and the older glacier-distal sediments (L3). Sedimentation rates are low (~4-20 cm/ka) from ~10 to 2.5 cal. ka BP, and increase (44-67 cm/ka) in the most recent sediments. Rates generally decrease with distance from the head of the fjord, where the greatest sediment sources are.
- Sediment provenance, based on a combination of magnetic susceptibility and XRF core-scanning data (Ca/Sum, Ti/Zr, and Fe/Zr) show that the influence of Ca-rich sediments from south of Wijdefjorden are limited in the till in the outer fjord, and that the Ca-rich

red sediments from the southwest are most present in the mid-fjord till, but still present in the till in the outer fjord.

- In glacier-proximal sediments, laminations of different colours, densities, and element ratios reflect the differing relative input of sediments from several areas. Red sediments derive from the southwest of Wijdefjorden or from Woodfjorden depending on the core location, while grey sediments come from the east and/or the northwest.
- The glacier-distal sediments are massive, indicating a greater distance from fluctuating sources and generally more stable conditions.
- In the glacier-distal sediments, sediment in the inner fjord is dominated by input from the south and southwest. The Ca-rich sediments from the southwest have a greater influence in the inner fjord, whereas sediments from the east are more important in the outer fjord. In the central fjord, however, it appears that sediments derived from both sides are important. Beyond the mouth of the fjord, sediments from Woodfjorden are also present.
- The deglaciation of the shelf likely occurred before ~16 cal. ka BP, and the presence of IRD after ~14.8 cal. ka BP on the shelf most probably indicates a destabilisation of the glaciers in the fjord and the beginning of their retreat.
- The transition from glacier-proximal to glacier-distal sedimentation on the shelf occurs around 12.2 cal. ka BP, in the middle of the Younger Dryas, signalling a weakening glacial influence beyond the fjord, despite the general cooling that occurred at this time.
- About 700 cal. years later, glacier-distal sediments were deposited in the central fjord, indicating that glaciers had receded to within the outer sill before 11.5 cal. ka BP.
- There is little IRD in cores between ~9.3 and 3.5 cal. ka BP. This may indicate that glaciers in northern Spitsbergen were small or absent at this time.
- In the inner fjord, a transition from glacier-proximal to glacier-distal sediments occurs around 7.2 cal. ka BP. This is late compared to other fjords on Svalbard, where the transition from glacier-proximal to -distal sedimentation occurred prior to ~11 cal. ka BP, due perhaps to locally more active glaciers or rivers near the core site immediately prior to that time.
- Beginning around ~3.5 cal. ka BP, there is more IRD in the cores, with a maximum from ~1.5 to 1.0 cal. ka BP. This is likely due to the generally cool conditions that have encouraged glacial advance since ~4 cal. ka BP.

7 References

- Aagaarda, K., Foldvik, A., Hillman, S.R., 1987. The West Spitsbergen Current: Disposition and water mass transformation. *J. Geophys. Res. Ocean.* 92, 3778–3784. <https://doi.org/10.1029/JC092iC04p03778>
- Alexanderson, H., Landvik, J.Y., Ryen, H.T., 2011. Chronology and styles of glaciation in an inter-fjord setting, northwestern Svalbard. *Boreas*. <https://doi.org/10.1111/j.1502-3885.2010.00175.x>
- Andersen, E.S., Dokken, T.M., Elverhøi, A., Solheim, A., Fossen, I., 1996. Late quaternary sedimentation and glacial history of the western Svalbard continental margin. *Mar. Geol.* 133, 123–156. [https://doi.org/10.1016/0025-3227\(96\)00022-9](https://doi.org/10.1016/0025-3227(96)00022-9)
- Andrews, J.T., Jennings, A.E., 1986. Influence of sediment source and type on the magnetic susceptibility of fiord and shelf deposits, Baffin Island and Baffin Bay, N.W.T. *Can. J. Earth Sci.* 24, 1386–1401. <https://doi.org/10.1139/e87-131>
- Austin, W.E.N., Telford, R.J., Ninnemann, U.S., Brown, L., Wilson, L.J., Small, D.P., Bryant, C.L., 2011. North Atlantic reservoir ages linked to high Younger Dryas atmospheric radiocarbon concentrations. *Glob. Planet. Change* 79, 226–233. <https://doi.org/10.1016/j.gloplacha.2011.06.011>
- Avaatech, 2016. TECHNICAL SPECIFICATIONS [WWW Document]. URL <http://www.avaatech.com/> (accessed 2.22.19).
- Baeten, N.J., Forwick, M., Vogt, C., Vorren, T.O., 2010. Late Weichselian and Holocene sedimentary environments and glacial activity in Billefjorden, Svalbard. *Geol. Soc. London, Spec. Publ.* 344, 207–223. <https://doi.org/10.1144/SP344.15>
- Bartels, M., Titschack, J., Fahl, K., Stein, R., Seidenkrantz, M.S., Hillaire-Marcel, C., Hebbeln, D., 2017. Atlantic Water advection vs. glacier dynamics in northern Spitsbergen since early deglaciation. *Clim. Past* 13, 1717–1749. <https://doi.org/10.5194/cp-13-1717-2017>
- Batchelor, C.L., Dowdeswell, J.A., Hogan, K.A., 2011. Late Quaternary ice flow and sediment delivery through Hinlopen Trough, Northern Svalbard margin: Submarine landforms and depositional fan. *Mar. Geol.* 284, 13–27. <https://doi.org/10.1016/j.margeo.2011.03.005>
- Bauch, H.A., Erlenkeuser, H., Spielhagen, R.F., Struck, U., Matthiessen, J., Thiede, J., Heinemeier, J., 2001. A multiproxy reconstruction of the evolution of deep and surface waters in the subarctic Nordic seas over the last 30,000 yr. *Quat. Sci. Rev.* 20, 659–678. [https://doi.org/10.1016/S0277-3791\(00\)00098-6](https://doi.org/10.1016/S0277-3791(00)00098-6)
- Beck, J.W., Richards, D.A., Edwards, R.L., Silverman, B.W., Smart, P.L., Donahue, D.J., Hererra-osterheld, S., Burr, G.S., Calsoyas, L., Jull, A.J.T., Biddulph, D., 2001. Extremely Large Variations of Atmospheric ¹⁴C Concentration During the Last Glacial Period 292, 2453–2458. <https://doi.org/10.1126/science.1056649>
- Benn, D.I., Evans, D.J.A., 2010. *Glaciers and Glaciations*, 2nd ed. Hodder Education, London. <https://doi.org/10.2307/1790982>
- Beszczynska-Möller, A., R.A. Woodgate, C., Lee, H.M., Karcher, M., 2011. A synthesis of exchanges through the main oceanic gateways to the Arctic Ocean. *Oceanography* 24, 82–99. <https://doi.org/10.5670/oceanog.2011.53>
- Bjarnadóttir, L.R., Rüther, D.C., Winsborrow, M.C.M., Andreassen, K., 2013. Grounding-line dynamics during the last deglaciation of Kveithola, W Barents Sea, as revealed by seabed geomorphology and shallow seismic stratigraphy. *Boreas* 42, 84–107. <https://doi.org/10.1111/j.1502-3885.2012.00273.x>
- Blott, S.J., 2010. GRADISTAT version 8.0: A Grain Size Distribution and Statistics Package

for the Analysis of Unconsolidated Sediments by Sieving or Laser Granulometer.

- Blum, P., 1997. P-Wave Velocity, in: *Physical Properties Handbook: A Guide to the Shipboard Measurement of Physical Properties of Deep-Sea Cores*. College Station, Texas, p. 17.
- Bondevik, S., Mangerud, J., Birks, H.H., Gulliksen, S., Reimer, P., 2006a. Changes in North Atlantic radiocarbon reservoir ages during the allerød and younger dryas. *Science* (80-.). 312, 1514–1517. <https://doi.org/10.1126/science.1123300>
- Bondevik, S., Mangerud, J., Birks, H.H., Gulliksen, S., Reimer, P., 2006b. Changes in North Atlantic radiocarbon reservoir ages during the Allerød and Younger Dryas: Supporting Material. *Science* (80-.). 312, 1514–1517. <https://doi.org/10.1126/science.1123300>
- Bowman, S., 1990. *Radiocarbon Dating*. University of California Press/London Museum, London.
- Brouwer, P., 2010. *Theory of XRF, Theory of XRF*.
- Brückner, H., Schellmann, G., 2003. Late Pleistocene and Holocene Shorelines of Andréeland, Spitsbergen (Svalbard) - Geomorphological Evidence and Palaeo-Oceanographic Significance. *J. Coast. Res.* 19, 971–982. <https://doi.org/10.2307/4299241>
- Butschek, F., Arosio, R., Austin, W.E.N., Noormets, R., Howe, J.A., 2018. Late Weichselian glacial history of Forlandsundet, western Svalbard: an inter-ice-stream setting. *Arktos* 0, 1–14. <https://doi.org/10.1007/s41063-018-0063-x>
- Chauhan, T., Noormets, R., Rasmussen, T.L., 2016a. Glaciomarine sedimentation and bottom current activity on the north-western and northern continental margins of Svalbard during the late Quaternary. *Geo-Marine Lett.* 36, 81–99. <https://doi.org/10.1007/s00367-015-0430-6>
- Chauhan, T., Rasmussen, T.L., Noormets, R., 2016b. Palaeoceanography of the Barents Sea continental margin, north of Nordaustlandet, Svalbard, during the last 74 ka. *Boreas* 45, 76–99. <https://doi.org/10.1111/bor.12135>
- Clark, P.U., 1987. Subglacial Sediment Dispersal and till Composition. *J. Geol.* 95, 527–541.
- Cokelet, E.D., Tervalon, N., Bellingham, J.G., 2008. Hydrography of the West Spitsbergen Current, Svalbard Branch: Autumn 2001. *J. Geophys. Res. Ocean.* 113, 1–16. <https://doi.org/10.1029/2007JC004150>
- Corfu, F., Gasser, D., Chew, D.M. (Eds.), 2014. *New Perspectives on the Caledonides of Scandinavia and Related Areas*. The Geological Society, London.
- Cottier, F.R., Nilsen, F., Enall, M.E., Gerland, S., Tverberg, V., Svendsen, H., 2007. Wintertime warming of an Arctic shelf in response to large-scale atmospheric circulation. *Geophys. Res. Lett.* 34, 1–5. <https://doi.org/10.1029/2007GL029948>
- Cottier, F.R., Nilsen, F., Skogseth, R., Tverberg, V., Skarðhamar, J., Svendsen, H., 2010. Arctic fjords: a review of the oceanographic environment and dominant physical processes. *Geol. Soc. London, Spec. Publ.* 344, 35–50. <https://doi.org/10.1144/SP344.4>
- Cottier, F.R., Tverberg, V., Inall, M., Svendsen, H., Nilsen, F., Griffiths, C., 2005. Water mass modification in an Arctic fjord through cross-shelf exchange: The seasonal hydrography of Kongsfjorden, Svalbard. *J. Geophys. Res. Ocean.* 110, 1–18. <https://doi.org/10.1029/2004JC002757>
- Crews, L., Sundfjord, A., Albretsen, J., Hattermann, T., 2017. Mesoscale Eddy Activity and Transport in the Atlantic Water Inflow Region North of Svalbard. *J. Geophys. Res. Ocean.* 201–215. <https://doi.org/10.1002/2017JC013198>
- Croudace, I.W., Rothwell, R.G., 2015. *Micro-XRF Studies of Sediment Cores: Applications of a non-destructive tool for the environmental sciences (Developments in*

- Paleoenvironmental Research), Tracking Environmental Change Using Lake Sediments. Volume 2: Physical and Geochemical Methods. <https://doi.org/10.1007/978-94-017-9849-5>
- Dallmann, W.K. (Ed.), 2015. Geoscience Atlas of Svalbard.
- Domack, E.W., McClemen, C.E., 1996. Foundations for Ecological Research West of the Antarctic Peninsula Accumulation of Glacial Marine Sediments in Fjords of the Antarctic Peninsula and Their Use As Late Holocene Paleoenvironmental Indicators 70, 135–154.
- Dowdeswell, J.A., Elverhøi, A., 2002. The timing of initiation of fast-flowing ice streams during a glacial cycle inferred from glacial marine sedimentation. *Mar. Geol.* 188, 3–14. [https://doi.org/10.1016/S0025-3227\(02\)00272-4](https://doi.org/10.1016/S0025-3227(02)00272-4)
- Dowdeswell, J.A., Hogan, K.A., Evans, J., Noormets, R., Cofaigh, C.O., Ottesen, D., 2010. Past ice-sheet flow east of Svalbard inferred from streamlined subglacial landforms. *Geology* 38, 163–166. <https://doi.org/10.1130/G30621.1>
- Dowdeswell, J.A., Ottesen, D., Forwick, M., 2016. Grounding-zone wedges on the western Svalbard shelf. *Geol. Soc. London, Mem.* 46, 233–234. <https://doi.org/10.1144/m46.128>
- Elvebakk, A., Bjerke, J.W., Nilsen, L., 2018. The lichen *Allocetraria madreporiformis* in high-arctic steppes on Svalbard : a result of out-of-Tibet migration ? 30, 1–11.
- Elverhøi, A., Andersen, E.S., Dokken, T., Hebbeln, D., Spielhagen, R.F., Svendsen, J.I., Sorflaten, M., Rornes, A., Hald, M., Forsberg, C.F., 1995. The Growth and Decay of the Late Weichselian Ice Sheet in Western Svalbard and Adjacent Areas Based on Provenance Studies of Marine Sediments. *Quat. Res.*
- Elverhøi, A., Lønne, Ø., Seland, R., 1983. Glaciomarine sedimentation in a modern fjord environment, Spitsbergen. *Polar Res.* 1, 127–150. <https://doi.org/10.1111/j.1751-8369.1983.tb00697.x>
- Falk-Petersen, S., Pavlov, V., Berge, J., Cottier, F., Kovacs, K.M., Lydersen, C., 2014. At the rainbow's end: high productivity fueled by winter upwelling along an Arctic shelf. *Polar Biol.* 38, 5–11. <https://doi.org/10.1007/s00300-014-1482-1>
- Farnsworth, W.R., Ingólfsson, Ó., Retelle, M., Allaart, L., Håkansson, L.M., Schomacker, A., 2018. Svalbard glaciers re-advanced during the Pleistocene–Holocene transition. *Boreas* 47, 1022–1032. <https://doi.org/10.1111/bor.12326>
- Farnsworth, W.R., Ingólfsson, Ó., Retelle, M., Schomacker, A., 2016. Over 400 previously undocumented Svalbard surge-type glaciers identified. *Geomorphology* 264, 52–60. <https://doi.org/10.1016/j.geomorph.2016.03.025>
- Flink, A.E., Noormets, R., 2018. Submarine glacial landforms and sedimentary environments in Vaigattbogen, northeastern Spitsbergen. *Mar. Geol.* 402, 244–263. <https://doi.org/10.1016/J.MARGEO.2017.07.019>
- Førland, E.J., Benestad, R., Hanssen-Bauer, I., Haugen, J.E., Skaugen, T.E., 2011. Temperature and Precipitation Development at Svalbard 1900–2100. *Adv. Meteorol.* 2011, 1–14. <https://doi.org/10.1155/2011/893790>
- Førland, E.J., Benestad, R., Hanssen-Bauer, I., Haugen, J.E., Skaugen, T.E., 2009. Climate development in North Norway and the Svalbard region during 1900 – 2100, *Advances in Meteorology*.
- Forman, S.L., Ingólfsson, Ó., 2000. Late Weichselian glacial history and postglacial emergence of Phippsøya, Sjuoyane, northern Svalbard: A comparison of modelled and empirical estimates of a glacial-rebound hinge line. *Boreas* 29, 16–25. <https://doi.org/10.1080/030094800424286>
- Forman, S.L., Lubinski, D.J., Ingólfsson, Ó., Zeeberg, J.J., Snyder, J.A., Siegert, M.J.,

- Matishov, G.G., 2004. A review of postglacial emergence on Svalbard, Franz Josef Land and Novaya Zemlya, northern Eurasia. *Quat. Sci. Rev.* 23, 1391–1434. <https://doi.org/10.1016/J.QUASCIREV.2003.12.007>
- Forman, S.L., Mann, D.H., Miller, G.H., 1987. Late Weichselian and Holocene relative sea-level history of Bröggerhalvöya, Spitsbergen. *Quat. Res.* 27, 41–50. [https://doi.org/10.1016/0033-5894\(87\)90048-2](https://doi.org/10.1016/0033-5894(87)90048-2)
- Forwick, M., 2013. How to use XRF core scanner data acquired with the Avaatech XRF core scanner at the Department of Geology, University of Tromsø.
- Forwick, M., Nam, S.-I., Kang, M.-H., Iversen, S., Holm, T., 2017. Cruise Report: Marine-Geoscientific Cruise to North Spitsbergen 1–23.
- Forwick, M., Vorren, T.O., 2011. Stratigraphy and deglaciation of the Isfjorden area, Spitsbergen. *Nor. Geol. Tidsskr.* 90, 163–179.
- Forwick, M., Vorren, T.O., 2009. Late Weichselian and Holocene sedimentary environments and ice rafting in Isfjorden, Spitsbergen. *Palaeogeogr. Palaeoclimatol. Palaeoecol.* 280, 258–274. <https://doi.org/10.1016/j.palaeo.2009.06.026>
- Forwick, M., Vorren, T.O., 2007. Holocene mass-transport activity and climate in outer Isfjorden, Spitsbergen: Marine and subsurface evidence. *Holocene* 17, 707–716. <https://doi.org/10.1177/0959683607080510>
- Forwick, M., Vorren, T.O., Hald, M., Korsun, S., Roh, Y., Vogt, C., Yoo, K.-C.K.-C., 2010. Spatial and temporal influence of glaciers and rivers on the sedimentary environment in Sassenfjorden and Tempelfjorden, Spitsbergen. *Geol. Soc. London, Spec. Publ.* 344, 163–193. <https://doi.org/10.1144/SP344.13>
- Forwick, M., Vorren, T.O., Hass, C., Vogt, C., 2011. Retarded deglaciation of north-Spitsbergen fjords during the last glacial – an example of bathymetric controls on the dynamics of retreating glaciers.
- Fransner, O., Noormets, R., Chauhan, T., O’Regan, M., Jakobsson, M., 2018. Late Weichselian ice stream configuration and dynamics in Albertini Trough, northern Svalbard margin. *Arktos* 4, 1. <https://doi.org/10.1007/s41063-017-0035-6>
- Fransner, O., Noormets, R., Flink, A.E., Hogan, K.A., O’Regan, M., Jakobsson, M., 2017. Glacial landforms and their implications for glacier dynamics in Rijpfjorden and Duvefjorden, northern Nordaustlandet, Svalbard. *J. Quat. Sci.* 32, 437–455. <https://doi.org/10.1002/jqs.2938>
- Gentz, T., Bonk, E., Hefter, J., Grotheer, H., Mollenhauer, G., 2018. First year of routine measurements at the AWI MICADAS 14C dating facility, in: 23rd International Radiocarbon Conference, NTNU, 17 June 2018 - 22 June 2018.
- Geotek, 2000. Multi-Sensor Core Logger Manual. United Kingdom.
- Gilbert, R., 1990. Rafting in glacial marine environments, in: Dowdeswell, J.A., Scourse, J.D. (Eds.), *Glacial Marine Environments: Processes and Sediments*. Geological Society Special Publication, London, pp. 105–120. <https://doi.org/10.1144/gsl.sp.1990.053.01.06>
- Gjelten, H.M., Nordli, Ø., Isaksen, K., Førland, E.J., Sviashchennikov, P.N., Wyszynski, P., Prokhorova, U. V., Przybylak, R., Ivanov, B. V., Urazgildeeva, A. V., 2016. Air temperature variations and gradients along the coast and fjords of western Spitsbergen. *Polar Res.* 35. <https://doi.org/10.3402/polar.v35.29878>
- Gjermundsen, E.F., Briner, J.P., Akçar, N., Foros, J., Kubik, P.W., Salvigsen, O., Hormes, A., 2015. Minimal erosion of Arctic alpine topography during late Quaternary glaciation. *Nat. Geosci.* 8, 789–792. <https://doi.org/10.1038/ngeo2524>
- Gjermundsen, E.F., Briner, J.P., Akçar, N., Salvigsen, O., Kubik, P., Gantert, N., Hormes, A.,

2013. Late Weichselian local ice dome configuration and chronology in Northwestern Svalbard: early thinning, late retreat. *Quat. Sci. Rev.* 72, 112–127. <https://doi.org/10.1016/J.QUASCIREV.2013.04.006>
- GLIMS, NSIDC, 2005. Global Land Ice Measurements from Space glacier database. <https://doi.org/10.7265/N5V98602>
- Görlich, K., 1988. Micas and texture of the Recent muds in Spitsbergen fjords: Study of suspension settling. *Ann. Soc. Geol. Pol.* 58, 21–52.
- Hagen, J.O., Liestøl, O., Roland, E., Jørgensen, T., 1993. *Glacier atlas of Svalbard and Jan Mayen*. Oslo.
- Hald, M., Ebbesen, H., Forwick, M., Godtliebsen, F., Khomenko, L., Korsun, S., Ringstad Olsen, L., Vorren, T.O., 2004. Holocene paleoceanography and glacial history of the West Spitsbergen area, Euro-Arctic margin. *Quat. Sci. Rev.* 23, 2075–2088. <https://doi.org/10.1016/J.QUASCIREV.2004.08.006>
- Hambrey, M.J., 1994. *Glacial Environments*. UCL Press Limited.
- Hansen, T., 2014. Late Weichselian and Holocene sedimentary processes and glacier dynamics in Woodfjorden, Bockfjorden and Liefdefjorden, North Spitsbergen.
- Hanssen-Bauer, I., 2002. Temperature and precipitation in Svalbard 1912-2050: Measurements and scenarios. *Polar Rec. (Gr. Brit.)* 38, 225–232. <https://doi.org/10.1017/S0032247400017757>
- Hanssen-Bauer, I., Førland, E., Hisdal, H., Mayer, S., Sandø, A., Sorteberg, A., Adakudlu, M., Andresen, J., Bakke, J., Beldring, S., Benestad, R., van der Bilt, W., Bogen, J., Borstad, C., Breili, K., Breivik, O., Y Børsheim, K., Christiansen, H., Dobler, A., K Wong, W., 2019. Climate in Svalbard 2100—a knowledge base for climate adaptation, Svalbardposten. <https://doi.org/10.13140/RG.2.2.10183.75687>
- Henriksen, M., Alexanderson, H., Landvik, J.Y., Linge, H., Peterson, G., 2014. Dynamics and retreat of the Late Weichselian Kongsfjorden ice stream, NW Svalbard. *Quat. Sci. Rev.* 92, 235–245. <https://doi.org/10.1016/j.quascirev.2013.10.035>
- Hjelle, A., 1993. *Geology of Svalbard*. Norsk Polarinstitutt, Oslo.
- Hogan, K.A., Dowdeswell, J.A., Noormets, R., Evans, J., Ó Cofaigh, C., Jakobsson, M., 2010. Submarine landforms and ice-sheet flow in the Kvitøya Trough, northwestern Barents Sea. *Quat. Sci. Rev.* 29, 3545–3562. <https://doi.org/10.1016/j.quascirev.2010.08.015>
- Hormes, A., Gjermundsen, E.F., Rasmussen, T.L., 2013. From mountain top to the deep sea – Deglaciation in 4D of the northwestern Barents Sea ice sheet. *Quat. Sci. Rev.* 75, 78–99. <https://doi.org/10.1016/J.QUASCIREV.2013.04.009>
- Howe, J.A., Austin, W.E.N., Forwick, M., Paetzal, M. (Eds.), 2010a. *Fjord Systems and Archives*.
- Howe, J.A., Austin, W.E.N., Forwick, M., Paetzal, M., Harland, R.E.X., Cage, A.G., 2010b. Fjord systems and archives: A review 5–15.
- Ingólfsson, Ó., Landvik, J.Y., 2013. The Svalbard-Barents Sea ice-sheet—Historical, current and future perspectives. *Quat. Sci. Rev.* <https://doi.org/10.1016/j.quascirev.2012.11.034>
- Isaksen, K.Ø., Nordli, E., Førland, J., Łupikasza, E., Eastwood, S., Niedźwiedź, T., 2016. Recent warming on Spitsbergen—Influence of atmospheric circulation and sea ice cover. *J. Geophys. Res. Atmos.* 121, 11913–11931. <https://doi.org/10.1002/2016JD025606>
- Jernas, P., Klitgaard Kristensen, D., Husum, K., Wilson, L., Koç, N., 2013. Palaeoenvironmental changes of the last two millennia on the western and northern Svalbard shelf. *Boreas* 42, 236–255. <https://doi.org/10.1111/j.1502-3885.2012.00293.x>

- Jessen, S.P., Rasmussen, T.L., Nielsen, T., Solheim, A., 2010. A new Late Weichselian and Holocene marine chronology for the western Svalbard slope 30,000-0 cal years BP. *Quat. Sci. Rev.* 29, 1301–1312. <https://doi.org/10.1016/j.quascirev.2010.02.020>
- Kempf, P., Forwick, M., Laberg, J.S., Vorren, T.O., 2013. Late Weichselian and Holocene sedimentary palaeoenvironment and glacial activity in the high-arctic van Keulenfjorden, Spitsbergen. *Holocene* 23, 1607–1618. <https://doi.org/10.1177/0959683613499055>
- Kleiber, H.P., Knies, J., Niessen, F., 2000. The Late Weichselian glaciation of the Franz Victoria Trough, northern Barents Sea: Ice sheet extent and timing. *Mar. Geol.* 168, 25–44. [https://doi.org/10.1016/S0025-3227\(00\)00047-5](https://doi.org/10.1016/S0025-3227(00)00047-5)
- Knies, J., Nowaczyk, N., Müller, C., Vogt, C., Stein, R., Vogt, C., Nowaczyk, N., Müller, C., Knies, J., 2000. A multiproxy approach to reconstruct the environmental changes along the Eurasian continental margin over the last 150 000 years. *Mar. Geol.* 163, 317–344. [https://doi.org/10.1016/S0025-3227\(99\)00106-1](https://doi.org/10.1016/S0025-3227(99)00106-1)
- Knies, J., Vogt, C., Stein, R., 1999. Late Quaternary growth and decay of the Svalbard/Barents Sea ice sheet and paleoceanographic evolution in the adjacent Arctic Ocean. *Geo-Marine Lett.* 18, 195–202. <https://doi.org/10.1007/s003670050068>
- Koenig, Z., Provost, C., Villacieros-Robineau, N., Sennéchaël, N., Meyer, A., Lellouche, J.-M., Garric, G., 2017. Atlantic waters inflow north of Svalbard: Insights from IAOOS observations and Mercator Ocean global operational system during N-ICE2015. *J. Geophys. Res. Ocean.* 122, 1254–1273. <https://doi.org/10.1002/2013JC009262>. Received
- Kowalewski, W., Rudowski, S., Zalewski, S.M., 1990. Seismoacoustic studies within Wijdefjorden, Spitsbergen. *Polish Polar Res.* 11, 287–300.
- Kreienisiek, H., 2018. AWI C-14 LAB [WWW Document]. Alfred Wegener Inst. URL <https://www.awi.de/en/expedition/laboratories/c-14-lab.html>
- Kristensen, D.K., Rasmussen, T.L., Koç, N., 2013. Palaeoceanographic changes in the northern Barents Sea during the last 16000 years - new constraints on the last deglaciation of the Svalbard-Barents Sea Ice Sheet. *Boreas* 42, 798–813. <https://doi.org/10.1111/j.1502-3885.2012.00307.x>
- Lambeck, K., 1995. Constraints on the Late Weichselian ice sheet over the Barents Sea from observations of raised shorelines. *Quat. Sci. Rev.* 14, 1–16. [https://doi.org/10.1016/0277-3791\(94\)00107-M](https://doi.org/10.1016/0277-3791(94)00107-M)
- Landvik, J.Y., Alexanderson, H., Henriksen, M., Ingólfsson, Ó., 2014. Landscape imprints of changing glacial regimes during ice-sheet build-up and decay: a conceptual model from Svalbard. *Quat. Sci. Rev.* 92, 258–268. <https://doi.org/10.1016/J.QUASCIREV.2013.11.023>
- Landvik, J.Y., Bondevik, S., Elverhøi, A., Fjeldskaar, W., Mangerud, J., Salvigsen, O., Siegert, M.J., Svendsen, J.I., Vorren, T.O., 1998. The last glacial maximum of Svalbard and the Barents sea area: Ice sheet extent and configuration. *Quat. Sci. Rev.* 17, 43–75. [https://doi.org/10.1016/S0277-3791\(97\)00066-8](https://doi.org/10.1016/S0277-3791(97)00066-8)
- Landvik, J.Y., Brook, E.J., Gualtieri, L., Raisbeck, G., Salvigsen, O., Yiou, F., 2003. Northwest Svalbard during the last glaciation: Ice-free areas existed. *Geology* 31, 905–908. <https://doi.org/10.1130/G19703.1>
- Landvik, J.Y., Ingólfsson, Ó., Mienert, J., Lehman, S.J., Solheim, A., Elverhøi, A., Ottesen, D., 2005. Rethinking Late Weichselian ice-sheet dynamics in coastal NW Svalbard. *Boreas* 34, 7–24. <https://doi.org/10.1080/03009480510012809>
- Lloyd, J., Kroon, D., Laban, C., Boulton, G., 1996. Deglaciation history and palaeoceanography of the western Spitsbergen margin since the last glacial maximum.

- Geol. Soc. Spec. Publ. 111, 289–301. <https://doi.org/10.1144/GSL.SP.1996.111.01.19>
- Löwemark, L., Schönfeld, J., Schäfer, P., 2006. Deformation of pyritized burrows: A novel technique for the detection and estimation of core shortening in gravity cores. *Mar. Geol.* 233, 37–48. <https://doi.org/10.1016/j.margeo.2006.08.004>
- Mangerud, J., 1972. Radiocarbon dating of marine shells, including a discussion of apparent age of Recent shells from Norway. *Boreas* 1, 143–172. <https://doi.org/10.1111/j.1502-3885.1972.tb00147.x>
- Mangerud, J., Bolstad, M., Elgersma, A., Helliksen, D., Landvik, J.Y., Lønne, I., Lycke, A.K., Salvigsen, O., Sandahl, T., Svendsen, J.I., 1992. The last glacial maximum on Spitsbergen, Svalbard. *Quat. Res.* 38, 1–31. [https://doi.org/10.1016/0033-5894\(92\)90027-G](https://doi.org/10.1016/0033-5894(92)90027-G)
- Mangerud, J., Bondevik, S., Gulliksen, S., Karin Hufthammer, A., Høisæter, T., 2006. Marine ¹⁴C reservoir ages for 19th century whales and molluscs from the North Atlantic. *Quat. Sci. Rev.* 25, 3228–3245. <https://doi.org/10.1016/j.quascirev.2006.03.010>
- Mangerud, J., Dokken, T., Hebbeln, D., Heggen, B., Ingólfsson, Ó., Landvik, J.Y., Mejdahl, V., Svendsen, J.I., Vorren, T.O., 1998. Fluctuations of the Svalbard-Barents Sea Ice Shelf during the last 150 000 years. *Quat. Sci. Rev.* 17, 11–42. [https://doi.org/10.1016/S0277-3791\(97\)00069-3](https://doi.org/10.1016/S0277-3791(97)00069-3)
- Mangerud, J., Landvik, J.Y., 2007. Younger Dryas cirque glaciers in western Spitsbergen: Smaller than during the Little Ice Age. *Boreas* 36, 278–285. <https://doi.org/10.1111/j.1502-3885.2007.tb01250.x>
- Mangerud, J., Svendsen, J.I., 2018. The Holocene Thermal Maximum around Svalbard, Arctic North Atlantic; molluscs show early and exceptional warmth. *Holocene* 28, 65–83. <https://doi.org/10.1177/0959683617715701>
- Mangerud, J., Bolstad, M., Elgersma, A., Helliksen, D., Landvik, J.Y., Lycke, A.K., Lønne, I., Salvigsen, O., Sandahl, T., Sejrup, H.P., 1987. The Late Weichselian glacial maximum in western Svalbard. *Polar Res.* 5, 275–278. <https://doi.org/10.1111/j.1751-8369.1987.tb00548.x>
- Meija, J., Coplen, T.B., Berglund, M., Brand, W.A., De Bièvre, P., Gröning, M., Holden, N.E., Irrgeher, J., Loss, R.D., Walczyk, T., Prohaska, T., 2016. Isotopic compositions of the elements 2013 (IUPAC Technical Report). *Pure Appl. Chem.* 88, 293–306. <https://doi.org/10.1515/pac-2015-0503>
- Menze, S., Ingvaldsen, R.B., Haugan, P., Fer, I., Sundfjord, A., Beszczynska-Moeller, A., Falk-Petersen, S., 2019. Atlantic Water Pathways Along the North-Western Svalbard Shelf Mapped Using Vessel-Mounted Current Profilers. *J. Geophys. Res. Ocean.* 124, 1699–1716. <https://doi.org/10.1029/2018JC014299>
- Nielsen, T., Rasmussen, T.L., 2018. Reconstruction of ice sheet retreat after the Last Glacial maximum in Storfjorden, southern Svalbard. *Mar. Geol.* 402, 228–243. <https://doi.org/10.1016/j.margeo.2017.12.003>
- Nilsen, F., Cottier, F., Skogseth, R., Mattsson, S., 2008. Fjord-shelf exchanges controlled by ice and brine production: The interannual variation of Atlantic Water in Isfjorden, Svalbard. *Cont. Shelf Res.* 28, 1838–1853. <https://doi.org/10.1016/j.csr.2008.04.015>
- Norwegian Polar Institute, 2018. TopoSvalbard [WWW Document]. URL toposvalbard.npolar.no/
- Norwegian Polar Institute, 2016. GeoSvalbard SG250 Raster: Offline geological map of Svalbard [Data set]. <https://doi.org/10.21334/npolar.2016.eafafbb7>
- Nuth, C., Kohler, J., König, M., Von Deschwanden, A., Hagen, J.O., Kääh, A., Moholdt, G.,

- Pettersson, R., 2013. Decadal changes from a multi-temporal glacier inventory of Svalbard. *Cryosphere* 7, 1603–1621. <https://doi.org/10.5194/tc-7-1603-2013>
- Ó Cofaigh, C., Dowdeswell, J.A., 2002. Laminated sediments in glacial marine environments: diagnostic criteria for their interpretation. *Quat. Sci. Rev.* 20, 1411–1436. [https://doi.org/10.1016/s0277-3791\(00\)00177-3](https://doi.org/10.1016/s0277-3791(00)00177-3)
- Ottesen, D., Dowdeswell, J.A., 2009. An inter-ice-stream glaciated margin: Submarine landforms and a geomorphic model based on marine-geophysical data from Svalbard. *Bull. Geol. Soc. Am.* 121, 1647–1665. <https://doi.org/10.1130/B26467.1>
- Ottesen, D., Dowdeswell, J.A., 2006. Assemblages of submarine landforms produced by tidewater glaciers in Svalbard. *J. Geophys. Res. Earth Surf.* 111, 1–16. <https://doi.org/10.1029/2005JF000330>
- Ottesen, D., Dowdeswell, J.A., Landvik, J.Y., Mienert, J., 2007. Dynamics of the Late Weichselian ice sheet on Svalbard inferred from high-resolution sea-floor morphology. *Boreas* 36, 286–306. <https://doi.org/10.1111/j.1502-3885.2007.tb01251.x>
- Ottesen, D., Dowdeswell, J.A., Rise, L., 2005. Submarine landforms and the reconstruction of fast-flowing ice streams within a large Quaternary ice sheet: The 2500-km-long Norwegian-Svalbard margin (57°–80°N). *Bull. Geol. Soc. Am.* 117, 1033–1050. <https://doi.org/10.1130/B25577.1>
- Ottesen, R.T., Bogen, J., Finne, T.E., Anderssen, M., Dallman, W., Eggen, O.A., Jartun, M., Lundkvist, Q., Pedersen, H.R., Volden, T., 2010. *Geochemical Atlas of Norway. Part 2: Geochemical atlas of Spitsbergen.* NGU, Trondheim.
- Pernègre, V.N., Blicek, A., 2016. A revised heterostracan-based ichthyostratigraphy of the wood bay formation (Lower Devonian, Spitsbergen), and correlation with Russian Arctic archipelagos. *Geodiversitas* 38, 5–20. <https://doi.org/10.5252/g2016n1a1>
- Plassen, L., Vorren, T.O., Forwick, M., 2004. Integrated acoustic and coring investigation of glacial deposits in Spitsbergen fjords. *Polar Res.* 23, 89–110. <https://doi.org/10.3402/polar.v23i1.6269>
- Quinn, R., Bull, J.M., Dix, J.K., 1998. Optimal Processing of Marine High-Resolution Seismic Reflection (Chirp) Data. *Mar. Geophys. Res.* 20, 13–20. <https://doi.org/10.1023/A>
- Rachlewicz, G., 2009. River floods in glacier-covered catchments of the High Arctic: Billefjorden, Wijdefjorden, Svalbard. *Nor. Geogr. Tidsskr.* 63, 115–122. <https://doi.org/10.1080/00291950902907835>
- Ramberg, I.B., Bryhni, I., Nøttvedt, A., Rangnes, K. (Eds.), 2013. *Landet Blir Til.* Norsk Geologisk Forening, Trondheim.
- Rasmussen, T.L., Forwick, M., Mackensen, A., 2013. Reconstruction of inflow of Atlantic Water to Isfjorden, Svalbard during the Holocene: Correlation to climate and seasonality. *Mar. Micropaleontol.* 99, 18–28. <https://doi.org/10.1016/j.marmicro.2013.03.011>
- Rasmussen, T.L., Thomsen, E., Skirbekk, K., Ślubowska-Woldengen, M., Klitgaard Kristensen, D., Koç, N., 2014. Spatial and temporal distribution of Holocene temperature maxima in the northern Nordic seas: Interplay of Atlantic-, Arctic- and polar water masses. *Quat. Sci. Rev.* 92, 280–291. <https://doi.org/10.1016/j.quascirev.2013.10.034>
- Rasmussen, T.L., Thomsen, E., Ślubowska, M.A., Jessen, S., Solheim, A., Koç, N., 2007. Paleooceanographic evolution of the SW Svalbard margin (76°N) since 20,000 14C yr BP. *Quat. Res.* 67, 100–114. <https://doi.org/10.1016/j.yqres.2006.07.002>
- Reimer, P.J., Bard, E., Bayliss, A., Beck, J.W., Blackwell, P.G., Ramsey, C.B., Buck, C.E., Cheng, H., Edwards, R.L., Friedrich, M., Grootes, P.M., Guilderson, T.P., Hafflidason, H., Hajdas, I., Hatté, C., Heaton, T.J., Hoffmann, D.L., Hogg, A.G., Hughen, K.A., Kaiser,

- K.F., Kromer, B., Manning, S.W., Niu, M., Reimer, R.W., Richards, D.A., Scott, E.M., Southon, J.R., Staff, R.A., Turney, C.S.M., van der Plicht, J., 2013. IntCal13 and Marine13 Radiocarbon Age Calibration Curves 0–50,000 Years cal BP. *Radiocarbon* 55, 1869–1887. https://doi.org/10.2458/azu_js_rc.55.16947
- Reimer, P.J., Reimer, R.W., 2016. A Marine Reservoir Correction Database and On-Line Interface. *Radiocarbon* 43, 461–463. <https://doi.org/10.1017/s0033822200038339>
- Richter, T.O., Gaast, S. van der, Koster, B., Vaars, A., Gieles, R., Stigter, H.C. de, Haas, H. De, Weering, T.C.E. van, 2006. The Avaatech XRF Core Scanner: technical description and applications to NE Atlantic sediments. *Geol. Soc. London, Spec. Publ.* 267, 39–50. <https://doi.org/10.1144/GSL.SP.2006.267.01.03>
- Salvigsen, O., 2002. Radiocarbon-dated *Mytilus edulis* and *Modiolus modiolus* from northern Svalbard: Climatic implications. *Nor. Geogr. Tidsskr.* 56, 56–61. <https://doi.org/10.1080/002919502760056350>
- Salvigsen, O., 1979. The last deglaciation of Svalbard. *Boreas* 8, 229–231. <https://doi.org/10.1111/j.1502-3885.1979.tb00804.x>
- Salvigsen, O., Høgvard, K., 2005. Glacial history , Holocene shoreline displacement and palaeoclimate based on radiocarbon ages in the area of. *Polar Res.* 25, 15–24.
- Salvigsen, O., Österholm, H., 1982. Radiocarbon dated raised beaches and glacial history of the northern coast of Spitsbergen, Svalbard. *Polar Res.* 1982, 97–115. <https://doi.org/10.1111/j.1751-8369.1982.tb00473.x>
- Schock, S.G., LeBlanc, L.R., Mayer, L.A., 1989. Chirp subbottom profiler for quantitative sediment analysis. *Geophysics* 54, 445–450. <https://doi.org/10.1190/1.1442670>
- Ślubowska, M.A., Koç, N., Rasmussen, T.L., Klitgaard-Kristensen, D., 2005. Changes in the flow of Atlantic water into the Arctic Ocean since the last deglaciation: Evidence from the northern Svalbard continental margin, 80°N. *Paleoceanography* 20, 1–16. <https://doi.org/10.1029/2005PA001141>
- Statistisk Sentralbyrå, 2005. Svalbardstatistikk.
- Stein, R., 2008. Proxies Used for Palaeoenvironmental Reconstructions in the Arctic Ocean. *Dev. Mar. Geol.* 2, 133–243. [https://doi.org/10.1016/S1572-5480\(08\)00004-3](https://doi.org/10.1016/S1572-5480(08)00004-3)
- Streuff, K., Ó Cofaigh, C., Noormets, R., Lloyd, J., 2018. Submarine landform assemblages and sedimentary processes in front of Spitsbergen tidewater glaciers. *Mar. Geol.* 402, 209–227. <https://doi.org/10.1016/j.margeo.2017.09.006>
- Streuff, K., Ó Cofaigh, C., Noormets, R., Lloyd, J.M., 2017. Submarine landforms and glacimarine sedimentary processes in Lomfjorden, East Spitsbergen. *Mar. Geol.* 390, 51–71. <https://doi.org/10.1016/J.MARGE0.2017.04.014>
- Stuiver, M., Braziunas, T., 1989. Atmospheric ¹⁴C and century-scale solar oscillations. *Nature* 338, 405–408. <https://doi.org/10.1038/340301a0>
- Stuiver, M., Reimer, P.J., Bard, E., Beck, J.W., Burr, G.S., Hughen, K.A., Kromer, B., McCormac, G., Van Der Plicht, J., Spurk, M., 1998. INTCAL98 radiocarbon age calibration, 24,000-0 cal BP. *Radiocarbon* 40, 1041–1083. <https://doi.org/10.1017/S0033822200019123>
- Stuiver, M., Reimer, P.J., Reimer, R.W., 2019. CALIB 7.1 [WWW program] [WWW Document]. URL <http://calib.org> (accessed 3.10.19).
- Stuiver, M., Suess, H.E., 1966. On the relationship between radiocarbon dates and true sample ages. *Radiocarbon* 8, 534–540. https://doi.org/10.2458/azu_js_rc.8.3343
- Sund, M., 2008. Polar hydrology, Norwegian Water Resources and Energy Directorate.

- Svendsen, J.I., Alexanderson, H., Astakhov, V.I., Demidov, I., Dowdeswell, J.A., Funder, S., Gataullin, V., Henriksen, M., Hjort, C., Houmark-Nielsen, M., Hubberten, H.W., Ingólfsson, Ó., Jakobsson, M., Kjær, K.H., Larsen, E., Lokrantz, H., Lunkka, J.P., Lyså, A., Mangerud, J., Matiouchkov, A., Murray, A., Möller, P., Niessen, F., Nikolskaya, O., Polyak, L., Saarnisto, M., Siegert, C., Siegert, M.J., Spielhagen, R.F., Stein, R., 2004. Late Quaternary ice sheet history of northern Eurasia. *Quat. Sci. Rev.* 23, 1229–1271. <https://doi.org/10.1016/J.QUASCIREV.2003.12.008>
- Svendsen, J.I., Elverhøi, A., Mangerud, J., 1996. The retreat of the Barents Sea Ice Sheet on the western Svalbard margin. *Boreas* 25, 244–256. <https://doi.org/10.1111/j.1502-3885.1996.tb00640.x>
- Svendsen, J.I., Mangerud, J., 1997. Holocene glacial and climatic variations on Spitsbergen, Svalbard. *Holocene* 7, 45–57. <https://doi.org/10.1177/095968369700700105>
- Svendsen, J.I., Mangerud, J., 1992. Paleoclimatic inferences from glacial fluctuations on Svalbard during the last 20 000 years. *Clim. Dyn.* 6, 213–220.
- Svendsen, J.I., Mangerud, J., Elverhøi, A., Solheim, A., Schüttenhelm, R.T.E., 1992. The Late Weichselian glacial maximum on western Spitsbergen inferred from offshore sediment cores. *Mar. Geol.* 104, 1–17. [https://doi.org/10.1016/0025-3227\(92\)90081-R](https://doi.org/10.1016/0025-3227(92)90081-R)
- Synal, H.A., Stocker, M., Suter, M., 2007. MICADAS: A new compact radiocarbon AMS system. *Nucl. Instruments Methods Phys. Res. Sect. B Beam Interact. with Mater. Atoms* 259, 7–13. <https://doi.org/10.1016/j.nimb.2007.01.138>
- Syvitski, J.P.M., Burrell, D.C., Skei, J.M., 1987. *Fjords: Processes and Products*. Springer-Verlag, New York.
- Syvitski, J.P.M., Syvitski, J.P.M., Praeg, D.B., Survey, G., 1989. Quaternary Sedimentation in the St. Lawrence Estuary and Adjoining Areas, Eastern Canada: An Overview Based on High-Resolution Seismo-Stratigraphy. *Géographie Phys. Quat.* 43, 291–310. <https://doi.org/10.7202/032784ar>
- Telesiński, M.M., Przytarska, J.E., Sternal, B., Forwick, M., Szczuciński, W., Łacka, M., Zajączkowski, M., 2018. Palaeoceanographic evolution of the SW Svalbard shelf over the last 14 000 years. *Boreas* 47, 410–422. <https://doi.org/10.1111/bor.12282>
- Thomas, G.S.P., Connell, R.J., 1985. Iceberg drop, dump, and grounding structures from Pleistocene glacio-lacustrine sediments, Scotland. *J. Sediment. Petrol.* 55, 243–249.
- Tjallingii, R., Röhl, U., Kölling, M., Bickert, T., 2007. Influence of the water content on X-ray fluorescence corescanning measurements in soft marine sediments. *Geochemistry, Geophys. Geosystems* 8, 1–12. <https://doi.org/10.1029/2006GC001393>
- Vihtakari, M., 2019. PlotSvalbard: PlotSvalbard - Plot research data from Svalbard on maps. R package version 0.8.5. [WWW Document]. URL <https://github.com/MikkoVihtakari/PlotSvalbard>
- Vorren, T.O., Hald, M., Thomsen, E., 1984. Quaternary sediments and environments on the continental shelf off northern Norway. *Mar. Geol.* 57, 229–257. [https://doi.org/10.1016/0025-3227\(84\)90201-9](https://doi.org/10.1016/0025-3227(84)90201-9)
- Vorren, T.O., Plassen, L., 2002. Deglaciation and palaeoclimate of the Andfjord-Vågsfjord area, North Norway. *Boreas* 31, 97–125. <https://doi.org/10.1111/j.1502-3885.2002.tb01060.x>
- Walczowski, W., 2010. Warming of the West Spitsbergen Current and sea ice conditions north of Svalbard 51.
- Wiedenbeck, M., 2015. MICADAS: New instrumentation for carbon-14 dating 11, 75–76.
- Wollenburg, J. E. & Mackensen, A., 1998. On the vertical distribution of living (Rose bengal

stained) benthic foraminifers in the Arctic Ocean. *J. Foraminifer. Res.* 28, 268–285.

Zwarts, L., Wanink, J., 1989. Siphon size and burying depth in deposit- and suspension-feeding benthic bivalves. *Mar. Biol.* 100, 227–240.